SCUOLA DI DOTTORATO
UNIVERSITÀ DEGLI STUDI DI MILANO-BICOCCA

Departments of Earth and Environmental Sciences (DISAT)

PhD program Chemical, Geological and Environmental Sciences

Cycle XXXI

Curriculum in Environmental Sciences

Processing and analysis of latest generation satellite data for monitoring optically complex waters

Surname: Cazzaniga Name: Ilaria

Registration number: 809088

Tutor: Prof. Colombo Roberto

Co-tutor: Ing. Giardino Claudia

Coordinator: Prof. Padoa Schioppa Emilio

ACADEMIC YEAR 2017/2018

A nonno Osvaldo,

dai cui balli, successi e sacrifici, piccoli e grandi,

potrò sempre imparare…

Summary

List of Figures

List of Tables

Abstract

Inland waters are a fundamental resource, not only as drinking water reservoir, but also for agricultural and productive activities, energy, tourism; they are also essential for ecological preservation and hydrologic regulation. In addition, they are extremely sensitive to a range of stressors operating at global, regional, and local scales and thus to environmental changes, and for this reason, they have been included in Essential Climate Variables (ECVs) list.

In the latest decade, the need for a continuous monitoring of waters quality state was stressed by several projects outcome as well as requested all over the world by directives such as the European Water Frame directive (2010).

Earth Observation (EO) techniques for water quality monitoring, have been spreading in the latest decades as a supporting tool to traditional measurements, providing, at relative low cost, information on surface water status at a synoptic scale and at higher frequency, in the form of maps of water quality. The physical quantity mainly used for the retrieval of water quality parameters (WQPs), such as chlorophyll-a concentration (chl-a), proxy of phytoplankton abundance, and key variable used for trophic status classification by the European WFD, is the water reflectance. It cannot be directly measured by remote sensors but should be retrieved instead from their imagery through a processing chain, which includes the removal of useless signal components, including the contribution due to the atmosphere (gases and aerosol), and other contributions and disturbances.

Accurate atmospheric correction is a key step to obtain accurate water reflectance signature, and thus accurate WQPs maps. For inland and coastal waters, in addition, this step is made more challenging by:

- the presence of optically complex waters, which hinder the use of traditional atmospheric correction methods
- the strong impact over the signal of adjacency effect, due to the small size of the lakes or their narrow shape or the proximity to the coast (brighter than water surfaces)
- the variability of aerosol composition, which strongly affects atmospheric and electromagnetic signal interactions.

The first objective of this PhD thesis is the evaluation of suitable processing chains for Remote Sensing optical data, provided by the latest generation satellite sensors (Nasa Landsat-8-OLI, L8, and ESA Sentinel-2A/B-MSI, S2A/B, and Sentinel-3A-OLCI, S3A) for water quality monitoring over optically complex waters, focusing on inland waters. In particular three case study area were selected, characterised by different trophic conditions: oligo-mesotrophic subalpine lakes and eutrophic Mantua lakes in North Italy; meso-eutrophic Lake Trasimeno in central Italy; hypereutrophic Curonian Lagoon, between Lithuanian and Russian territories, on the Baltic Sea. Several atmospheric correction techniques were applied to be compared and validated through *in situ* radiometric measurements. Best performing water reflectance products were thus used to retrieve chl-a concentration maps through bio-optical model, which products were again validated against *in situ* measurements.

As a second objective, in fact, phytoplankton trend analysis over selected study area were performed: eutrophication time trend, phytoplankton phenology, intensive algal bloom detection, and potential contribution of EO data to WFD monitoring activities were evaluated, exploiting validated, best performing EO products time series.

Good performances were obtained from several algorithms especially for more turbid, with higher water leaving signal, waters, but satisfying performances were obtained also in more oligotrophic lakes, in particular for final chl-a maps products.

Sensors products inter-comparison produced very good results encouraging merging their data series for both short and long term trend analysis. Merged time series allowed, together with previously validated ENVISAT-MERIS derived maps, to assess seasonal patterns in lakes but also a slight trend towards eutrophication in subalpine lakes, as well as for pelagic area of Lake Trasimeno.

For intensive algal bloom detection, latest sensors products showed to be very efficient and useful, in particular being able to catch rapid and spatially delimited phenomena.

Finally, in WFD monitoring applications, it was clear that higher frequency monitoring provided by EO techniques allows to have a more complete characterization of waters state, both in term of space and time, respect to punctual and less frequent *in situ* measurements, still fundamental for validation and vertical variability characterization.

1. Main objective and thesis overview

Earth Observation (EO) **techniques for water quality monitoring**, are now spreading as a supporting tool to traditional measurements since about four decades (e.g. Tyler et al., 2016). They provide, at relative low cost and for some bio-geophysical parameters, information on surface water status. In the context of the operational exploitation of multisource remotely sensed data for water quality applications, the main objective of this thesis is the evaluation of the application for complex waters quality monitoring, focusing on inland waters, of the latest generation sensor imagery (OLI, on board of Landsat-8 satellite; MSI, on board Sentinel-2A/B; OLCI on board Sentinel-3A/B). Three specific objectives can be outlined.

The **first objective** is the evaluation of the most suitable processing chain for water quality parameters retrieval from the latest generation sensors imagery over inland waters. In the first part of this PhD thesis, several algorithms have been applied to be compared, looking for suitable processing chain for selected study areas. Several comparative studies already exist, about different atmospheric correction algorithms for inland waters (e.g., Guanter et al., 2010; Jaelani et al., 2013; Dörnhöfer et al., 2016; Bernardo et al., 2017; Martins et al., 2017) as described in next sections. On the other hand, the aim of this thesis is not the definition of the optimal choice to approach any inland water body in the world, using any EO sensor, but rather a validation of some of the most common approaches already used over other case studies area, to be adapted to the specific couple sensor - target for different case studies. As observed, in fact, by the previous stated studies, no single algorithm performs consistently better than others, in all inland waters globally, using any kind of sensor. In this work, validation activities were in any case extended to different European environments (Sec. 3), with different levels of eutrophication, in order to test the approach for robustness. The validation and the definition of the best choices is an on-going activity, since algorithms are continuously updated and new tools become available, and on the other hand, imagery, mainly for newest sensors, are reprocessed following the calibration activity.

The **second objective** is the application of the validated products for monitoring activities such as the support for the WFD activities and for ecological studies, as algal bloom detection, the

assessment of long-time and seasonal trends in phytoplankton phenology and trophic status of selected study areas (the subalpine lakes and Lake Trasimeno). This second objective has been carried out in the second part of this thesis, in which the best performing techniques over selected areas have been applied to retrieve chlorophyll-a (chl-a) concentration maps, for water eutrophication status assessment, and to perform trend analysis, exploiting latest and older generations satellite sensors imagery.

As a **third objective**, the feasibility of a synergic use of different latest generation sensors for chl-a products has been assessed, with the aim of enlarging time series, together with exploiting capability of each sensor to capture phenomena at different space or temporal scales: sensors characterized by higher temporal resolution allow, for example, to detect very quick phenomena, while sensors with higher spatial resolution allow to assess smaller spatial variations.

In this thesis, after the introduction and an overview on atmospheric correction and water quality parameters retrieval techniques, study areas are described. In materials and methods section, the sensors, which imagery was exploited here, and the validation activity are presented. Ancillary data, field campaigns and statistical methods used for the validation are also described. All atmospheric correction processors compared and validated are described instead in ANNEX I.

In results section, both comparison results for atmospheric correction products and results from validation of chl-a concentration maps are shown for each study area and sensor.

Finally, three different applications are presented, with the methods used and the results obtained: phytoplankton seasonal and long-time trend and phenology analysis, EO products application for WFD classification of lakes, algal bloom detection in subalpine lakes.

All the activities of this thesis were carried out in the framework of the following projects: GLaSS (7^{th} Framework Programme, project number313256); EOMORES (grant agreement No. 730066) funded under the European Union's Horizon 2020 research and innovation program; BLASCO (CARIPLO Rif. 2014-1249); ISEO (CARIPLO Rif. 2015-0241); INFORM (grant agreement No. 606865, FP7/2007-2013).

2. Introduction

Water is the most important resource on Earth. It is also the most abundant but, absurdly, of the world's total water resources, only 2.5% is represented by freshwater, and about 1.2% of that is surface water, being the rest locked up in ice-caps or groundwater. A large percentage of people in the world is experiencing water stress and, even worse, greenhouse warming will not have an ignorable role in redefining the state of global water systems (Vörösmarty et al., 2000). Already now, human health and development are threatened by not only insufficient but also poor quality water. The increase in intensive water use, the untreated (both domestic and industrial) discharges, fertilisers and pesticides used in agriculture, accidental and intentional spills of harmful substances, in last centuries, since industrialization, have led to the degradation of inland and coastal waters (EEA, 1995). In the latest decades, in some cases, water collecting and treatment systems, in addition to reduction in fertilizer, brought some improvements in water quality (e.g. Sec. 3.1.1).

Inland waters are usually a source, not only as drinking water reservoir, but also for its use in agricultural and productive activities, energy, tourism, etc. and they are essential for ecological preservation and hydrologic regulation.

The Millennium Ecosystem Assessment (MEA, 2005), a taskforce initiated by United Nations Secretary-General in 2001, generated a list of the so called 'ecological services' which inland waters provide. They can be divided into four categories:

- provisioning (i.e., food supply, water supply, and biodiversity);
- regulating (i.e., climate regulation, hydrological flows, and pollution control);
- cultural (i.e., recreational, aesthetic, and educational);
- supporting and regulating (i.e., soil formation, nutrient cycling, and pollination) (World Resources Institute 2005).

Even if inland waters are only a small part of total land surface, (approximately 53106 km^2 considering all water bodies larger than 0.002 km^2 (Verpoorter et al., 2014)), globally the value the ecosystem services they provide is impressive: in De Groot et al. (2012) monetary value of these

fresh water ecosystem services was evaluated, on the basis of available studies and databases, to be about 4267 Int.$/ha/year (2007 price levels).

In addition, lakes are extremely sensitive to a range of stressors operating at global, regional and local scales and are thus 'sentinels' of environmental change: the impact of rapid and uncontrolled environmental changes, is clearly visible in eutrophication, proliferation of toxic algae, increase in turbidity, loss of aquatic benthos, and harmful effects on health for both animals and men (Mishra et al., 2017).

In 2011, inland water bodies have been included among Essential Climate Variables (ECVs), which "*provide the empirical evidence needed to understand and predict the evolution of climate, to guide mitigation and adaptation measures, to assess risks and enable attribution of climate events to underlying causes, and to underpin climate services. They are required to support the work of the UNFCCC and the IPCC*" (WMO). In this context, according to CCI (Climate Change Initiative) project, lakes can be important as:

- indicators for hydrological and climate conditions at regional scale (monitoring changes in lakes volume);
- proxy of climate variations (through lakes water temperature monitoring and ice formation and break-up, and fast ice duration).

They are also a meaningful indicator of the development pressure, and land use and land cover change.

The Spanish National Ecosystem Assessment in 2013, within the framework of the Millennium Ecosystem Assessment study concluded "*that 45% of the ecosystem services assessed at the national level have been degraded or are being used unsustainably, with regulating services being the most negatively affected*"[1]. In particular, for inland and coastal waters a *"considerable degradation of most of their services, with the only exception being cultural services*" was observed. The assessment concluded that actions were required reverse the degradation and the loss of ecosystem services (Gardner et al., 2015). Several other national and international directives focused on these problems, aiming to improve water bodies ecological state: US Clean Water Act (U.S. Senate, 2002), South African National Water Act (Government of South Africa,

[1] Gardner et al., 2015.

1998), National Water Management Strategy of Australia and New Zealand (Australian Government, 2000), the Canada Water Act (Government of Canada, 1985).

In the European Union, the need for having "*[…] a coherent and comprehensive overview of water status within each river basin district*[2]" was defined by Water Framework Directive (WFD), setting out the requirements for the monitoring of, among the others, surface water status. WFD has the main objective of maintaining 'good' and non-deteriorating status for all waters.

In particular, WFD obliges member states to monitor systematically all natural and artificial lakes with a surface larger than 0.5 km^2 (Premazzi et al., 2003), implying measuring in field some indicators of lake water quality to be carried out indicatively every three months. Later, some works (e.g. Skeffington et al., 2015) discussed the need of reducing time interval, in particular trying to catch periods when phytoplankton is rapidly changing. One of the most important indicators is in fact chlorophyll-a concentration (chl-a), measured as a proxy of phytoplankton abundance, which is, in turn, one of the groups suggested for ecological status assessment by the WFD. In Italy, adopting the WFD, the minimum frequency was raised up to six samples/year.

On the other hand, traditional field limnologic measurements, even if essential and able to provide information at species level from the surface to the deepest layers, are punctual measurements, both in terms of time and space. For these reasons, they sometimes are not able, even with the Italian higher frequency, to catch quick temporal and spatial variability, within the same basin, lacking of representativeness. More in general, the approach can rarely sustain the frequency and spatial coverage required to support effective management practices in vulnerable areas (IOCCG 2008), with the risk of resulting in erroneous water quality classifications (Bresciani et al., 2011; van Puijenbroek et al., 2015).

Earth Observation (EO) techniques for water quality monitoring, are now spreading as a supporting tool to traditional measurements, providing, at relative low cost and for some bio-geophysical parameters, information on surface water status at a synoptic scale and at higher frequency, since about four decades (e.g. Tyler et al., 2016). Regular observations of physical and biogeochemical components in inland and coastal waters provides essential information in the form of maps of water quality, bottom properties and bathymetry as needed for science and

[2] Article 8 of the Water Framework Directive (WFD, WFD 00/60/EC; EC Parliament and Council, 2000)

resource management (e.g. Palmer et al. 2015a; Olmanson et al., 2008; Dekker and Hestir, 2012; Mouw et al. 2015).

In the last ten years, the number of publications related to the use of remote sensing techniques for inland waters quality monitoring has increased: the publications including the terms *Remote Sensing* and *Inland waters*, listed in Web of Knowledge are more than 270[3]. In 2016, the article review by Dörnhöfer and Oppelt, provided a comprehensive overview of how remote sensing can support lakes research and monitoring, listing all the available validated methods, to retrieve, among others, information on lakes biota and water transparency. Although the promising results, the same review stresses how these techniques still need to be integrated in monitoring frameworks activities, such as the European WFD and or the US Clean Water Act.

2.1 Remote Sensing techniques for inland waters quality monitoring: opportunities and challenges

Indicators observable from EO for inland/coastal waters, through passive sensors only, are mainly:

- pigments concentration, in particular chl-a, which is a proxy of phytoplankton abundance and key variable used for trophic status classification by the European WFD
- Total Suspended Matter (TSM) concentration (some time split in inorganic and organic fraction)
- Colored Dissolved Organic Matter (CDOM) absorption, proxy of its abundance
- Transparency/turbidity of water column
- diffuse attenuation coefficient K_d
- presence of cyanobacteria
- submerged and emerged aquatic vegetation
- floating materials
- bathymetry (in shallow waters)
- substrates types such as corals, macroalgae, sand, rocks
- oil spill
- ice cover
- Surface Water Temperature (SWT)

[3] Last queried on 24/3/2018

Providing maps of the above indicators, at high frequency, could thus be a useful tool to be integrated to classical measurements for:

- seasonal and long-term trends analysis of water quality and surface temperature
- algal blooming identification and monitoring
- early warning systems input for algal blooms
- generating indicators according to users' needs
- phenology trends analysis
- change detection over emerged aquatic vegetation and over submerged habitats such as those colonised by aquatic vegetation and by corals, including their bleaching
- quantification and morphology of the areas of plumes.

The physical quantity mainly used for water quality parameters (WQP) retrieval, such as chl-a concentration, TSM, CDOM, transparency and others, is the **water reflectance**, in particular, **Remote Sensing Reflectance** (Rrs). Rrs is an Apparent Optical Property (AOP), a spectral quantity, which for water surfaces depends on the content and concentration of optically reactive substances dissolved or suspended in the euphotic layer of water column, as well as on illumination conditions. Rrs spectrum is the result of the interaction of the electromagnetic signal with, in addition to the water itself, phytoplankton, detrital and organic matter substances, dissolved or suspended in the water column, which absorb and scatter light in a different way along the electromagnetic spectrum. It cannot be directly measured by remote sensors but can be retrieved from their products through a processing chain, which includes the removal of useless signal components. Total signal includes, in fact, sky and solar radiance scattered by atmospheric molecules and aerosols, Sun and sky radiance reflected directly by the water surface and whitecaps, radiance scattered by surrounding area, scattered into the field of view of the sensor by the atmosphere, and finally radiance scattered by water column. On the total amount of the signal recorded by remote sensing optical sensors, water and water components contribution is very small, while most of the signal is due to the interactions with the atmosphere (up to 90%). For this reason, accurate atmospheric correction is a key step to obtain accurate Rrs and thus accurate WQPs maps.

2.1.1 Atmospheric correction over inland waters

Atmospheric correction is the process of removing the contributions to the signal due to different sources than the water column and its constituents. The signal measured by the sensors out of

Earth atmosphere (Top-Of-Atmosphere radiance, L_{TOA}) is the sum of different components as listed in Equation 1 (Moses et al., 2017):

$$L_{TOA} = L_a + L_r t_r + L_w t_w \ [Eq. 1]$$

where L_a is the atmospheric path radiance, i.e. the contribution due to gases and aerosol in atmosphere, L_r is the specular radiance from the water surface, t_r is the transmittance for the specular radiance through the atmosphere, L_w is the water-leaving radiance, and t_w is the transmittance of the radiance from water to sensor (Figure 1). L_a and L_r are the non-water components that atmospheric correction aims at removing.

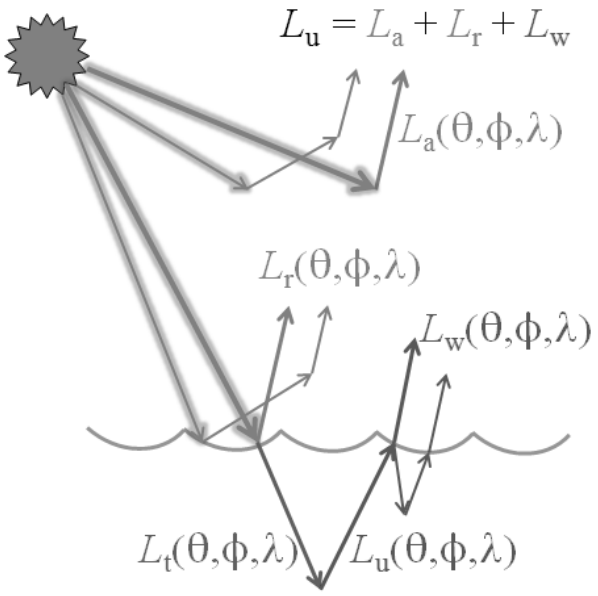

Figure 1 Interaction between solar radiation, atmosphere, water surface and water components.

Water reflectance ρ_w is obtained from L_w as in Equation 2 (Moses et al., 2017):

$$\rho_w = \frac{\pi L_w}{\cos(\vartheta_s)\, E_0 t_s} \ [Eq. 2]$$

where E_0 is the scalar solar irradiance, ϑ_s the solar zenith angle, and t_s is the transmittance of the solar radiation on its way from the sun to the water surface. Finally, Rrs used for WQPs retrieval, is obtained dividing ρ_w by π, thus treating the water surface as a Lambertian surface.

Accurate aerosol contribution estimate (both composition and quantity) are required, since as Keller (2001) observed, incorrect values may produce large errors in obtaining Rrs and consequently in retrieving concentrations of water quality parameters. In particular, the effect of inaccurate visibilities (or AOT concentration) on Rrs, and thus finally on chl-a concentration and

back-scattering of particles retrieval, is larger for visibility lower than 15 km (i.e. larger values of AOT).

Remote sensing of ocean colour from space began in 1978, with the successful launch of NASA's Coastal Zone Color Scanner (CZCS), while, at the beginning on the Nineties, airborne imaging spectrometry and Thematic Mapper on-board of Landsat provided relevant data for studying inland waters. Since that, numerous algorithms have been developed to correct the signal for atmospheric effects over waters. Several atmospheric correction algorithms have been developed for open ocean waters (e.g., Gordon and Wang, 1994; Fukushima et al., 1998, 2007; Bailey et al., 2010 and references herein; Antoine and Morel, 2011), used for imagery correction of several sensors such as CZCS, the MODerate resolution Imaging Spectroradiometer (MODIS), the Sea-viewing Wide Field-of-view Sensor (SeaWiFS), Medium Resolution Imaging Spectrometer (MERIS), the Visible Infrared Imaging Radiometer Suite (VIIRS).

At the basis of these algorithms, there is the assumption that the water-leaving radiance is negligible in the near-infrared (NIR) region (black-pixel assumption), which holds true for waters with very low pigments and particulate matter concentrations. In more turbid waters (e.g., Doerffer and Fischer, 1994; Ruddick et al., 2000; Siegel et al., 2000; Hu et al., 2000; Ali et al., 2013; Al Shehhi et al., 2017 and references herein), the signal, also in the NIR region, is not negligible, due to scattering by particles in water, preventing the use of these black-pixel assumption based algorithms. In addition, for inland and coastal waters, the problem of atmospheric correction is trickier to be solved due to the following factors:

- the presence of optically **complex waters**: these waters are characterised by high phytoplankton biomass concentration, mineral particles, detritus and CDOM, that typically do not co-vary over space and time, as they do in open ocean waters. They hinder the use of traditional atmospheric correction methods (Moore et al., 1999; Ruddick et al., 2000; Wang and Shi, 2005; Palmer et al., 2015a; Vanhellemont and Ruddick, 2015). Sediment concentrations in inland waters, typically due to the proximity to the coast and thus to human discharges from terrestrial sources, surface and sub-surface runoff, cause in fact non-negligible reflectance of water in the near-infrared region, typically used to estimate and remove the effect of atmospheric aerosol contribution (Mishra et al., 2017).
- the strong impact over the signal of **adjacency** effect, due to the small size of the lakes or their narrow shape or the proximity to the land (usually brighter than water surfaces and often

showing a complex orography), which signal is scattered with multiple and complicated patterns into sensor field-of-view by the atmosphere (Van Mol and Ruddick, 2005; Kiselev et al., 2015; Sterckx et al., 2015; Bulgarelli et al., 2017);

- the **variability of aerosol composition**, which strongly affects atmospheric and electromagnetic signal interactions (Moses et al., 2017). In addition, on land, aerosol composition is strongly impacted by human activities;
- the variability in the **altitude** of the water bodies, which introduces further uncertainties estimating aerosol contribution (Moses et al., 2017).

Aside the application of Radiative Transfer Model (e.g. 6SV, Second Simulation of the Satellite Signal in the Solar Spectrum – Vectorial, Vermote et al., 2006; MODTRAN, MODerate resolution atmospheric TRANsmission, Berk et al., 2008, 2014), parametrised through ancillary measurements of visibility or aerosol load and microphysical properties (see Sec. 4.3), several approaches have been developed to deal with non-negligible reflectance in the NIR region and they were recently reviewed by Moses et al. (2017). For example, Vanhellemont and Ruddick (2015) proposed an approach very similar to Gordon and Wang (1994), but retrieving the aerosol contribution using, instead of NIR bands, SWIR (short-wave infrared) bands. Many sensors lack SWIR bands, and the black-pixel assumption may not be valid in extremely turbid waters at the shorter end of the SWIR region. Finally, these bands are often affected by high sensor noise. The Management Unit of the North Sea Mathematical Models algorithm (MUMM), originally developed for SeaWiFS imagery only, was dedicated to atmospheric correction over inland and turbid waters, retrieving the aerosol reflectance ratio extracted from clear water pixels in the image, where the water reflectance is assumed to be zero (Ruddick et al., 2000). This approach could result not applicable in all inland waters, due to the fact that an entire inland water body might be turbid, with no clear water pixels (Vidot and Santer, 2005), and also to the fact that adjacency effects might contaminate the observed radiance, especially in the NIR region (Moses et al., 2017). Other algorithms exploit aerosol information retrieved from land, based often on Dense Dark Vegetation (DDV) method (Kaufman and Sendra, 1988), as implemented in ATCOR (Richter and Schläpfer, 2014). Also, the sensor-independent atmospheric correction scheme OPERA (OPERational Atmospheric correction algorithm, Sterckx et al., 2015, now iCOR (Image correction for atmospheric effects, De Keukelaere et al., 2018), and SelfContained Atmospheric Parameters Estimation for MERIS data (SCAPE-M) automatic atmospheric correction processor (Guanter et al., 2007, 2008), belong to this category. This approach resulted to be applicable to waters with

various complexities, also where most of the water-based aerosol retrievals fail. On the other hand, the major issue with this method is the lack of pixels satisfying the criteria for DDV, often hindering the aerosol type being derived from the image itself (Moses et al., 2017).

Other methods use the simultaneous retrieval of aerosol and gases contribution, water reflectance and WQPs. Usually, this approach is implemented through non-linear optimization (Kuchinke et al., 2009) or Neural Networks (NN) as in Case-2 Regional (C2R) processor (Doerffer and Schiller, 2007, now C2RCC, Brockmann et al., 2016, see Sec. 0 in ANNEX I), the Free University Berlin (FUB) processor (Schroeder et al., 2007), the Eutrophic Lakes processor and the Boreal Lakes processor (Doerffer and Schiller, 2008a), which were dedicated to ENVISAT-MERIS and have been now developed for other sensors (S2-MSI, L8-OLI, S3-OLCI). Of course, these NNs are trained according to a specific dataset of simulations (*Hydrolight* (Mobley and Sundman, 2013, a commercial software product of Numerical Optics, Ltd) for *C2R*, RT codes (Fischer and Grassl, 1984; Fell and Fischer, 2001) for *FUB*) or *in situ* measurements: data from lakes of Finland for the Boreal Lakes Processor and from Spanish lakes and water reservoirs for the Eutrophic Lakes processor. Even though these training sets try to cover a broad range of concentrations, not always these processors are well performing over any kind of environment. Based on the same approach (with the simultaneous retrieval), but not on NN techniques, is the *POLYMER* (POLYnomial based algorithm applied to MERIS, Steinmetz et al., 2011) algorithm, which is described later (Sec. b in ANNEX I).

Finally, other approaches based on the retrieval of aerosol characteristics only based on images (the so-called image-based algorithms) perform atmospheric correction without using any external ancillary information. This group includes approaches like the Dark Object Subtraction (DOS), scanning for and subtracting the lowest radiance in the image, taken as 'the dark pixel' radiance; *COST* COsine of the Solar zeniTh angle (Chavez, 1996), extending the DOS method approximating the downward atmospheric transmittance with the cosine of the solar zenith angle; the QUick Atmospheric Correction (*QUAC*) algorithm (Bernstein et al., 2005a, 2005b), depending again on dark pixels availability.

In the latest years, several works compared different approaches and algorithms for the latest generation sensors, over several case study areas, with different characteristics, in terms of water types, atmospheric and surrounding environmental conditions.

Among all the available algorithms, some of them have been validated in this thesis activities, over different study areas (Sec. 3). The choice was driven, sensor by sensor, and target by target, by:

- good performances of the algorithms over inland waters for the same sensors;
- good performances of the algorithm over similar or the same environment with other sensors in the past;
- availability of the algorithm (since are not always publicly available) for each specific sensor;
- availability of ancillary information (e.g. aerosol microphysical properties).

Looking among previous comparative work on atmospheric correction for the latest generation sensors, for Sentinel-2A-MultiSpectral Imager (S2A-MSI) sensor, Dörnhöfer et al. (2016) compared results over the oligotrophic Lake Starnberg in Germany, obtained through Sen2Cor (Müller-Wilm, 2013, Sec. e), MIP (Modular Inversion Processor, an EOMAP property physics-based method, https://www.eomap.com) and ACOLITE (Atmospheric Correction for OLI 'lite', an atmospheric correction and processor for the Landsat-8-Operational Land Imager (L8-OLI) and S2A-MSI developed at RBINS, Sec. d in ANNEX I): MIP outperformed Sen2Cor and ACOLITE at most measurement sites, mainly in terms of spectrum shape as showed by χ^2 (defined in validation section) values obtained. Martins et al. (2017), compared results from 6SV, ACOLITE and Sen2cor, over Amazon Floodplain Lakes, obtaining different results over the different lakes: better performances through Sen2Cor and ACOLITE over dark lakes, and better performance through 6SV over brighter lakes. Even in this study, it is clear how the selection of the proper "*atmospheric correction method needs to be aligned with the study purposes and user expertise to apply these tools*"[4] since their results showed advantages and disadvantages of different methods for the reflectance shape and magnitude accuracy. Finally, in this floodplains case study the limitation in retrieving accurate spectra in the NIR region was shown, due to the strong adjacency effect caused by the presence of the forest. DOS, QUAC, the Fast Line-of-sight Atmospheric Analysis of Hypercubes (FLAASH, an interface for MODTRAN, Adler-Golden et al., 1999), ACOLITE, and Provisional Landsat-8 Surface Reflectance Algorithm – L8SR were compared for L8-OLI over the Barra Bonita eutrophic hydroelectric reservoir (Bernardo et al., 2017). Performances were evaluated in terms of magnitude, providing the best results for L8SR.

[4] Martins et al. (2017)

In the previous decade, over the principal study areas of this thesis (Sec. 3), some algorithms were validated for different applications obtaining good results. In particular, C2R was exploited for MERIS imagery processing over large Italian lakes (Giardino et al., 2008), and for the implementation of the Water Framework Directive in European peri-alpine lakes (Bresciani et al., 2011); MODTRAN-based c-WOMBAT-c procedure (Brando and Dekker, 2003) was used over Lake Garda for an Hyperion image (Giardino et al., 2007) and 6SV was applied over Lake Garda to MIVIS (Multispectral Infrared and Visible Imaging Spectrometer) data (Bresciani et al., 2012a), a L8-OLI, a MODIS-Aqua, and a RapidEye-3 images (Giardino et al., 2014a). SCAPE-M for MERIS imagery was validated and compared to C2R results, over different European lakes, included Italian subalpine lakes and Lake Trasimeno: SCAPE-M performed well over more turbid waters (i.e. Trasimeno) but problems were underlined for clear waters, where C2R performed better. ATCOR-4 (Sec. c in ANNEX I) and 6SV were exploited, using the continental and rural predefined aerosol models respectively, to atmospherically correct MIVIS imagery over lakes Trasimeno, Garda, Mantua, and Idro (a smaller Lake included in phytoplankton bloom analysis in Sec. 6.3) (Giardino et al., 2015a). Over the oligotrophic Lake Geneva, very similar to Lake Garda, a comparative validation was made through ACOLITE, OPERA, and C2RCC atmospheric corrected products for L8-OLI and S2-MSI imagery: C2RCC performed better by non-ideal atmospheric conditions, while ACOLITE produced good results by perfect weather conditions (Depuis, 2017).

Processors used for image processing in this thesis are fully described in ANNEX I.

2.1.2 Water quality parameters retrieval over inland waters

The most important parameter used to retrieve trophic level is chl-a concentration, and several algorithms have been developed and validated in the last decades, to derive chl-a maps from Rrs.

In particular, for chl-a concentration these approaches can be divided into three main categories:

- approaches based on empirical/semi-empirical algorithms (e.g. Matthews et al., 2012; Medina-Cobo, 2014; Kudela et al., 2015)
- physically based approaches, based on spectral inversion of analytical/semi-analytical models, or neural networks (e.g. Doerffer and Schiller, 2008a, 2008b; Riha and Krawczyk, 2011; Wynne et al., 2010; Li et al., 2013, 2015; Mishra et al., 2013)
- hybrid solutions (Carvalho et al., 2010; Matsushita et al., 2015).

Empirical algorithms apply simple or multiple regressions between chl-a concentration and the ratios or the values of irradiance reflectance or Rrs, while **semi-empirical models** exploit specific spectral features of absorption and scattering of the constituents governing reflectance. Empirical algorithms can be divided into other three categories: green/blue ratios algorithms, red-NIR band ratios algorithms and further empirical algorithms. The first category includes many operational algorithms and exploits the fact that the absorption of blue light is increasing with phytoplankton concentration, as observed in waters degrading from blue to green in Morel and Prieur, 1977. Thus, these algorithms usually relate chl-a concentration to the ratios among a blue band and a green band, both in clear oceans and lakes waters (e.g. Chavula et al., 2009). The blue band is selected in the range 442-490 and the green band in the range 488-555, respectively, according to bands availability for different sensors and configurations used in imagery processing. The benchmark for ocean colour is the *O'Reilly* chlorophyll algorithm (known as *OCx*, where x is the number of bands involved), a modified cubic polynomial (MCP) function which has been chosen as the at-launch SeaWiFS operational chl-a algorithm, and then adapted and improved in several configurations. Nowadays, it is used for chl-a retrieval from MODIS, VIIRS, MERIS, OCTS imagery, and even for S3-OLCI Ocean Colour Products in Case 1 waters in the configuration:

$$log10[chl] = \sum_{x=0}^{4} \left(A_x (log_{10}\left(R_j^i\right)^x\right) \; [Eq.3]$$

where R_j^i is the maximum ratio of irradiance reflectance at band i, among 443, 490 and 510 nm, over irradiance reflectance at band j at 560 nm. Despite their good performance in open ocean waters, they are less accurate in more productive waters (Odermatt et al., 2012), in particular, due to the presence of CDOM (with high absorption in shorter wavelengths) and the primary chl-a absorption feature. On the other hand, better results have been retrieved using the red-NIR ratios algorithms, which are based on the combination of 2 or 3 bands, exploiting the secondary absorption maximum at 665 nm, the reflectance peak around 700 nm (minimum absorption of phytoplankton, TSM, CDOM, and water) and its fluorescence emission band at 681 nm (Mittenzwey et al., 1992; Gons et al., 2002; Gower, et al., 2005; Moses et al., 2009a, 2009b; Mishra and Mishra, 2012; Matthews et al., 2012; Odermatt et al., 2012). While their strength are their simplicity and rapidity in data processing, empirical algorithms are yet generally only appropriate to waters with characteristics similar to those used in the algorithm development (Lee et al., 2002). Similar to this approach, are also most of the methods used to detect cyanobacteria, based

on the spectral characteristics of their accessory pigments (e.g., phycocyanin, phycoerythrin) associated with different algal species (e.g., *Microcystis* spp., *Planktothrix* spp.). For example, Bresciani et al. (2009) used a three-band algorithm (677, 747, and 710 nm) to detect chl-a concentration associated with chlorophyte and cyanobacterial bloom in a productive lake; Kutser (2009) used a band ratio of two MERIS channels (620 and 665 nm) to map cyanobacterial blooms in the Baltic Sea.

The **analytical**, **semi-analytical**, and **quasi-analytical algorithms** (e.g. Arst and Kutser, 1994; Kutser et al., 2001; Dekker et al., 2011; Carder et al., 2004; Gitelson et al., 2008; Lee et al., 2009) are based on solutions to the radiative transfer equation. They are based on the inversion of the radiative transfer equations establishing relationships among AOPs (i.e. Rrs or rrs, Remote Sensing Reflectance below water surface) and IOPs (Inherent Optical properties, i.e. algal and non-algal particles and detrital backscattering and absorption), through several analytical and empirical steps, inverting the equation:

$$rrs(\lambda) = g_1\left(\frac{b_b(\lambda)}{a(\lambda)+b_b(\lambda)}\right) + g_2\left(\frac{b_b(\lambda)}{a(\lambda)+b_b(\lambda)}\right)^2 \quad [Eq.4]$$

where $a(\lambda)$ is the total spectral absorption coefficient, $b_b(\lambda)$ is the total spectral backscattering coefficient, g_1 and g_2 are geometrical factors (Gordon et al., 1975, 1988). They allow separating the phytoplankton absorption components in the signal from Gelbstoff and detritus contribution. In addition, they can adjust for the variation of the chlorophyll-specific phytoplankton absorption coefficient, which varies according to chl-a concentration and nutrient and light availability (Carder et al., 1999).

The main difference between semi-analytical and quasi-analytical models is the method used to estimate $b_b(\lambda)$ and $a(\lambda)$: for semi-analytical models, the knowledge of the absorption of algal particles ($a_{phy}(\lambda)$), non-algal particles ($a_{NAP}(\lambda)$) and Colored Dissolved Organic Matter ($a_{CDOM}(\lambda)$) is required, while for quasi-analytical models, the total $a(\lambda)$ is derived directly from Rrs, and the other absorptions coefficients are computed from the spectral decomposition of the estimated $a(\lambda)$ (Lee et al., 2002, 2007,2009). Semi-analytical models require thus *in situ* measurements, in order to be set with the site/seasonal specific IOPs.

In this thesis activities, for WQPs retrieval, **BOMBER** (Bio-Optical Model Based tool for Estimating water quality and bottom properties from Remote Sensing images, Giardino et al., 2012), was used as a tool for the spectral inversion exploiting a semi-analytical models technique (Sec. 4.4.1)

and, alternatively over extreme eutrophic waters, a semi-empirical algorithm was used (Sec. 4.4.2).

3. Study areas

In this thesis, some first applications were presented (analysis of the phytoplankton phenology, seasonal and long-time trends of trophic status evolution and algal blooms detection), mostly focused in Italy over Lake Garda, one of the Italian, subalpine lakes, and Lake Trasimeno, as study cases. In order to show the approach robustness, comparison and validation of different processing methods were extended to other Italian subalpine lakes, with both similar and different eutrophic and boundary conditions and where *in situ* measurements useful for validation were available. The Italian lakes investigated in this study are shown in Figure 2, while Table 1 indicates their principal morphological feature. Here, a description follows of all the study areas over which several approaches have been tested: the description is more detailed for lakes Garda and Trasimeno. Finally, Sec. 3.4 describes an international site, the Curonian Lagoon, as it was providing an additional record of field data useful for the validation of the processors.

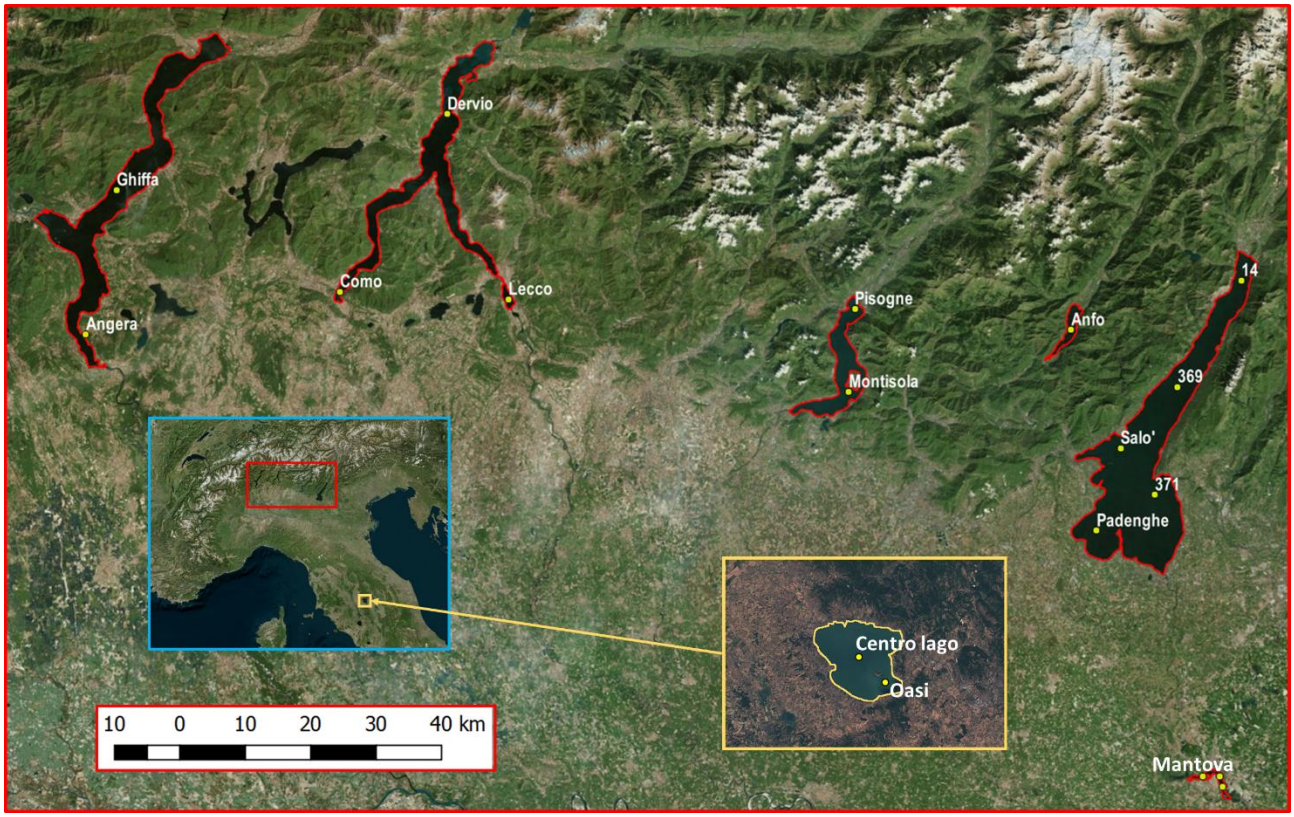

Figure 2 Italian study sites. In red, from West to East: Maggiore, Como, Iseo, Garda, Idro, Mantova. In yellow: Lake Trasimeno Yellow dots indicate the regional environmental protection agencies sampling sites for chl-a concentration monitoring.

Table 1 Principal characteristics of case study lakes.

Lake	Surface (km^2)	Volume (km^3)	Max depth (m)	Mean Depth (m)	Altitude (m a.s.l.)	Catchment area (km^3)
Como	145	22.5	410	154	198	4,508
Garda	370	50.4	346	136	65	2,290
Maggiore	212	37.1	370	177	193	6,599
Iseo	65	7.6	251	124	185	1,777
Mantova	6	0.2	15	3.5	18	855
Trasimeno	124	0.6	6	4.5	258	396
Curonia	1,584	6.2	5.8	3.7	0	

3.1 Subalpine Italian lakes

The Italian deep southern subalpine lakes, Garda, Iseo, Como, and Maggiore, represent an essential, extensively used, water resource for North Italy.

Their origin is due to glacial excavation over tectonic-fluvial valley (Carollo and Libera, 1992) and they are classified as clear oligotrophic deep lakes (Garda and Maggiore), oligo-mesotrophic (Lake Como) and meso-eutrophic (Lake Iseo, Leoni et al., 2014). They are all oligomittic lakes, meaning that complete overturn of the water column (which brings to the euphotic layer from the bottom, sediments rich in nutrients) happens once in a year, but only in those years characterized by a strongly cold and windy winter (Salmaso, 2011). In response to both the local climate and large-scale climatic variability, an increasing stability of the water column is shown by recent studies (Rogora et al., 2018).

From the climatic point of view, subalpine lakes lie between Alps, where climate is more rigid, and the Po valley, where climate is continental but mitigated by the presence of the Alps itself, which operate as a shield for northern colder winds, and, in the Eastern part, of the Adriatic Sea. Lakes themselves contribute to the mitigation of the climate of the close surrounding area.

On the other hand, climate changes are bringing changes over the hydrologic cycle itself: for example, in Lombardia region, where at least partially all the subalpine lakes, here included, lie, a clear trends in increasing temperature were recorded in the recent years: 2016 was the sixth warmest year since the last century, with an increase in temperatures of about 1.35 degrees, comparing to the 1961-1990 average (ISPRA, 2017). On the contrary, a slight decreasing trend in precipitation was recorded, in addition to a reduction in the number and an intensification of precipitation events. The decrease of snow precipitations and of the increasing temperatures are

bringing a reduction of glaciers snow cover, and both surfaces and volumes of Alps glaciers are strongly decreasing (ARPA Lombardia, 2007).

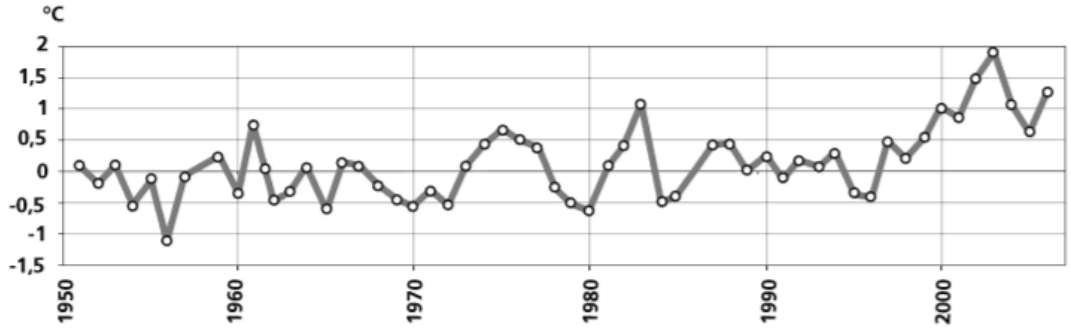

Figure 3 Anomalies in yearly mean average temperature comparing to 1961-1990 – temperature (13°) in Lombardy. A trend towards positive anomalies is clearly shown since 1996 (Source: ARPA Lombardia).

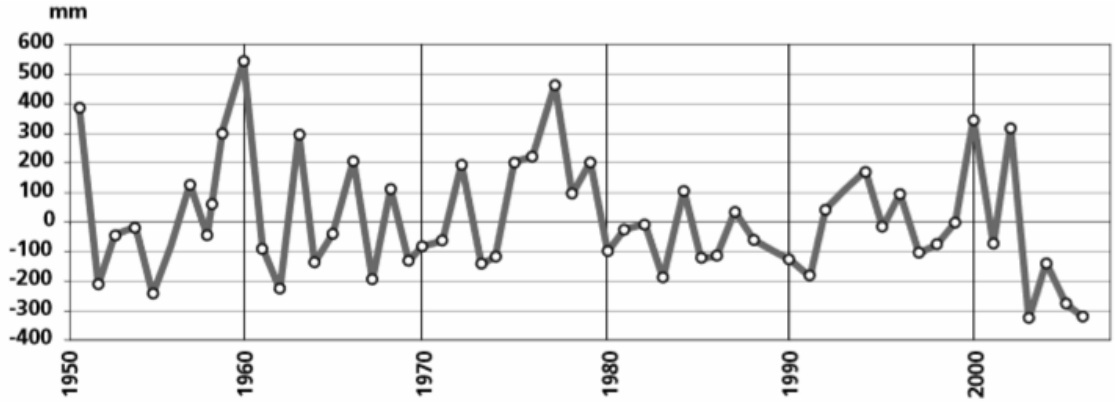

Figure 4 Anomalies in yearly total precipitation comparing to 1961-1990 mean yearly total precipitation (1008 mm) in Lombardia. No trends are clearly visible excepted for the last years (Source: ARPA Lombardia).

3.1.1 Lake Garda

Figure 5 Lake Garda. View from Punta Staffalo, Sirmione.

Lake Garda (Figure 5) is the largest Italian lakes, extending for 370 km² at 65 m a.s.l., 50.35 km^3 across Lombardia, Trentino Alto Adige, and Veneto regions. Water level is regulated by Salionze dam, located on Mincio river, its emissary, south of the lake, while the major affluent is Sarca river. It is an oligomittic lake: the latest complete overturn events occurred in 2004, 2005, and 2006 (Rogora et al., 2018), as shown in Figure 6. In addition, an extended vertical mixing (until 170 m depth, about 76% of the lake volume) occurred in 2013 (Rogora et al., 2018). Theoretical residence time is about 26.8 years. Its waters are extensively used as a source for drinking water, irrigation, productive activities, and electrical production: water is pumped upstream and stored in Lake Ledro, West-North. On the other hand, the most important uses are bathing and recreational activities linked to tourism, which brings to its coast more than 10 millions of tourists every year (Gallinaro et al., 2013). Fishing activities have been reduced, mainly due to several invasive species that appeared in the last decades affecting littoral and pelagic biota (Gallinaro et al., 2013).

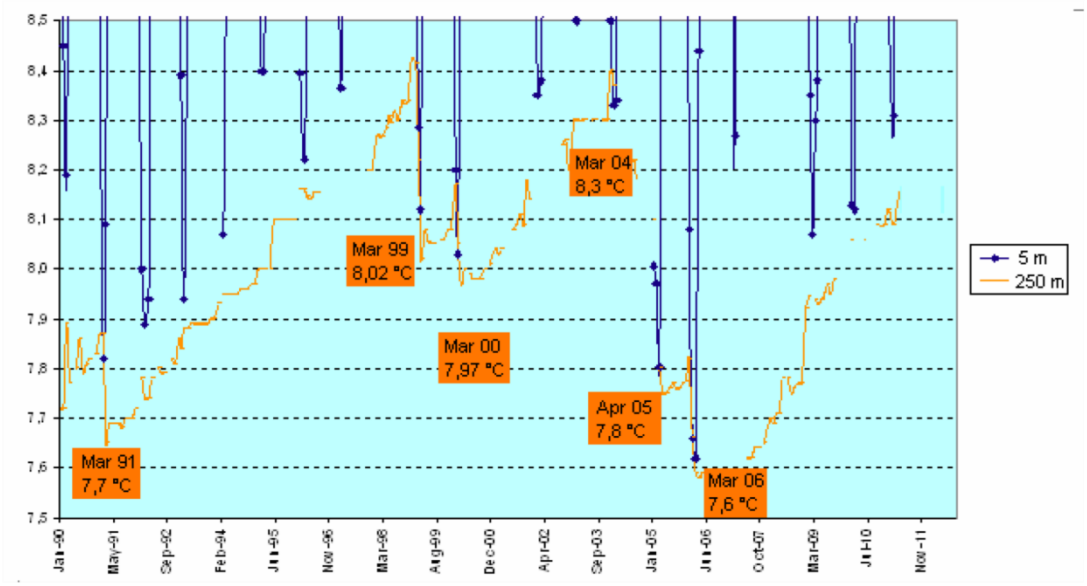

Figure 6 Water temperature at 5 and 250 m depths. In orange boxes the dates of complete overturn. (Source: APPA Trento)

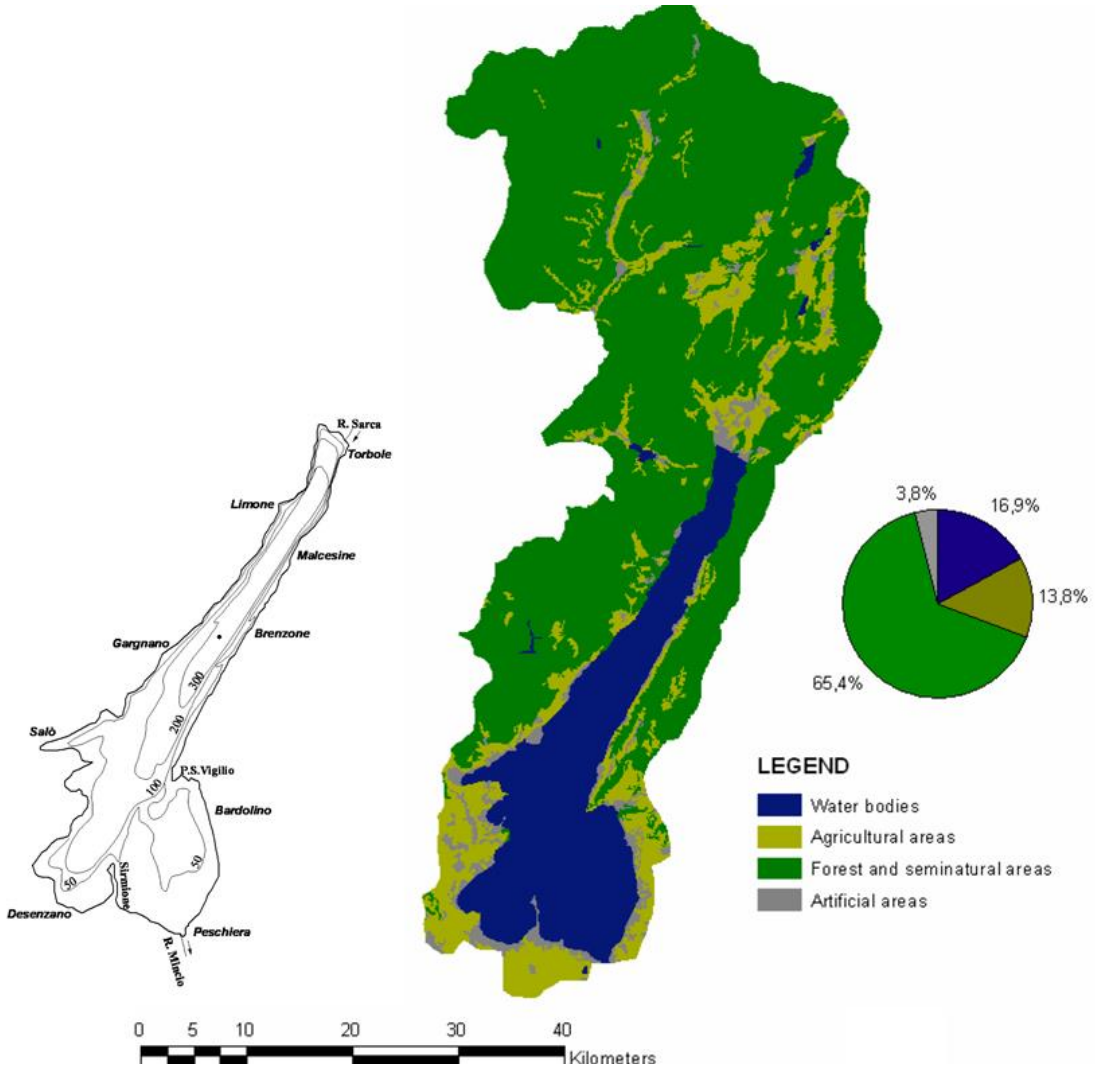

Figure 7 Lake Garda: on the left bathymetry (Source: Barbanti 1974, modified); on the right land use of the basin (Source: Corine Land Use, level 1, 2006).

The lake itself can be divided into three sub-basin, the narrowest northern one, and the two southern basins, divided by a submerged ridge, extending from Sirmione Peninsula to Punta San Virgilio promontory, which divides the lake into a deeper western basin (Figure 7) and a shallower eastern basin (Salmaso, 2010). They are characterised by different depth, different characteristics and vocation of the coasts and, mainly in the touristic period, by different level of water quality.

As the other subalpine lakes, its coast is characterized, in the northern part, by mountain slopes mainly covered by forests and rural territories (Figure 7), while the southern part is characterised by hills, sloping gently down to the coast, and mostly urban and in part agricultural. In the last century in the coastal area urbanization increased due mainly to tourism vocation of the area. Since the 1980's, a collector has been gathering all sewer discharges around the coast, bringing black waters, after pre-treating, downstream of the dam.

Since the 1970s, phosphorus concentrations increased in the whole water column (Salmaso, 2011), until 2006, when it stabilised, but, in the absence of the water column overturn (complete or at least at deep depth), large part of nutrients remains in the hypolimnetic layers through the sedimentation of organic particles.

Chl-a concentration in Lake Garda shows seasonal variation, as showed by superficial values measured *in situ* by protection agencies (ARPAV, ARPA Lombardia and APPA Trento) shown in Figure 8, with first peaks in spring, highest values recorded in summer, with some more rare peaks in autumn.

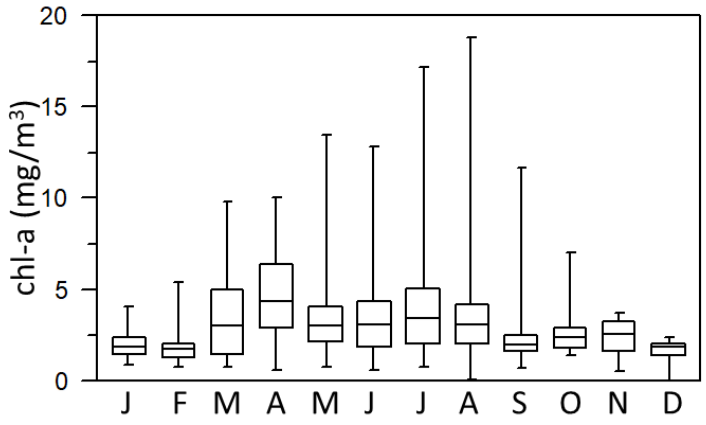

Figure 8 Monthly box-plot for all available chl-a superficial concentration in situ measurements for period 1997-2017, Lake Garda. For each month median values, 25% and 75% percentiles and min and maximum values are shown.

Regarding phytoplankton composition, in Lake Garda (Figure 9) large diatoms (dominated by *Fragilaria crotonensis*), cyanobacteria, (dominated by *Planktothrix rubescens*) and chlorophytes (dominated by *Mougeotia* sp.) prevail (Salmaso and Padisák, 2007; Gallina et al., 2013).

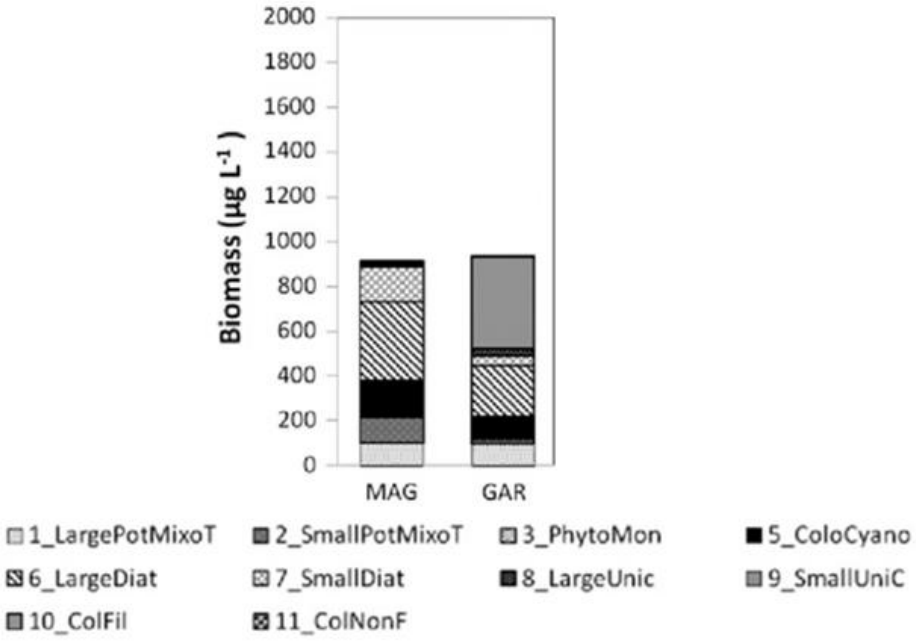

Figure 9 Diversity of phytoplankton composition upon their morpho-functional groups (MFG) for lakes Maggiore (MAG) and Garda (GAR) (Salmaso and Padisàk, 2007, modified).

The increased concentrations of total phosphorus had a positive impact on Oscillatoriales and Diatomeae, since Cyanobacteria are in general the most positively responding phylum to an increase of eutrophication. Cyanobacteria have their maximum development in summer-autumn period, while diatoms dominate the spring period. Chl-a concentration is regularly monitored by Regional and provincial environmental protection agencies in the monitoring points, listed in Table 2, and shown in Figure 2. In the shallower southern part of the lake, macrophytes are strongly developed but its typical submerged communities, are being replaced by de-structured stands, probably due to the decrease in water temperature and the increase in water level fluctuations (Bresciani et al., 2012b).

Table 2 Monitoring stations of regional and provincial protection agency in Lake Garda

Station	Agency	Latitude	Longitude
Salò	ARPA Lombardia	45.62	10.61
Sirmione/Padenghe	ARPA Lombardia	45.50	10.56
369	ARPAV	45.70	10.72
371	ARPAV	45.55	10.68
14	APPA Trento	45.84	10.85

In parallel to water quality trend analysis and algal bloom detection, some analysis have been carried out on air temperature and precipitation regimes and trends. For air temperature and precipitation monitoring, the closest monitoring stations to Lake Garda, with available data for the study period, are ARPA Lombardia stations in Ponti sul Mincio (MN), Limone sul Garda (BS), Padenghe sul Garda (BS), Puegnago sul Garda (MN), ARPAV station in Bardolino (VR). In addition, an AERONET (AErosol RObotic NETwork, Holben et al., 1998, see Sec. 4.5) installed in October 2013 in Sirmione, provides information about microphysical properties of the aerosol over the study area.

3.1.2 Lake Maggiore

Figure 10 Lake Maggiore, view from Eremo Santa Caterina del Sasso.

Lake Maggiore (Figure 10) is the second largest Italian lake by surface (212 km^2) and volume (37 km^3, mean depth 177 m) at 194 m a.s.l. The lake itself and the catchment area, which is 6599 km^2 large, the largest of the southern subalpine lakes (1.1% are glaciers), belongs to Switzerland, and Italian Lombardia and Piemonte regions. Water uses include recreational use, navigation, fishery, but Lake Maggiore is, first of all, an essential source for the agricultural consortiums South the lake and for hydroelectric power production.

Its shape is very narrow with a north-southern elongated shape. Deepest bottoms are situated in the central and northern parts, shallower bottoms are in the southern and in Switzerland, in the northern part. The most important tributaries are rivers Ticino and Maggia, Toce from Lake Orta and Tresa from Lake Lugano. The only effluent is Ticino river where Miorina dam, regulating lake waters level, is located.

Lake Maggiore underwent rapid eutrophication during the 60s and 70s, reaching mesotrophic state, with a return to oligotrophy during the 80s and the 90s (Visconti et al., 2008). In fact, after the creation of wastewater treatment plants in late 1970s, the phosphorous inputs decreased. As Lake Garda, Lake Maggiore is an oligomittic lake, with latest complete overturn occurred in 2005 and 2006 (the return period was about 7 years between 1950s and 1970s, Rogora et al., 2018). Renewal time is about 4.1 years. Phytoplankton composition is dominated by small and large diatoms, together with colonial cyanobacteria (Figure 9).

3.1.3 Lake Como

Figure 11 Lake Como, Lecco branch, viewed from Alpe del Giumello.

Lake Como (or Lario, Figure 11) is the deepest Italian lake (maximum depth: 410 m, in front of Argegno, on the western coast); its surface and water volume are 146 km^2 and 22.5 km^3, respectively. The catchment area is around 4522 km^2. It has a narrow shape as the other subalpine lakes but in the southern part it is divided into two branches, called Lake Lecco (East) and Lake Como (West), resembling an upside-down “Y”. The Como branch is separated from the rest of the

lake by an underwater ridge and has a water renewal time of 8.3 years (Buzzi, 2002), while is lower for the Lecco branch, where the main effluent (Adda river) is located. For the whole lake has been estimated in 12.8 years (Buzzi et al., 1997). Adda is also its major affluent, together with the minor tributaries Mera, Fiumelatte, Pioverna, Liro, Livo, Albano, Telo, Breggia, and Varrone. Spring vertical mixing typically involves the first 150-200 m, with the latest extended vertical mixing occurred in 2009, involving 71% of the lake volume, while the latest complete turnovers occurred in 2005 and 2006 (Rogora et al., 2018).

Its waters are exploited for drinking water, energetic, industrial, irrigation, transport, fishing, and recreational uses. Lake Como has undergone eutrophication since the 60's, culminated in the '80s when the concentration of total phosphorus in front of the coast of the city of Como (South of the western branch), was detected in 80 μg l^{-1}. Since 1980s, total phosphorus concentrations started decreasing, causing a significant decrease of some dominant species, such as *Microcystis aeruginosa* and *Melosira granulata*, linked to higher eutrophication level.

The most dominant taxa, detectable almost along the whole year, are *Fragilaria crotonensis* and *Planktothrix rubescens* (Buzzi, 2002), while minor species as *Tabellaria fenestrata* and *Mougeotia sp*. in the western basin, and *Asterionella formosa* in the eastern basin, tend to show a single, conspicuous peak during their annual development. On the other hand, however, a considerable amount of phosphorus is blocked in the deep hypolimnion, from where could be re-suspended to the upper layer in years of complete or more extended episodes of vertical mixing, creating suitable conditions for the development of cyanobacterial blooms. Some examples occurred in August 2000, when a bloom of *M. aeruginosa* developed in the entire western branch, with a maximum density of 300,000 cell ml^{-1} (Buzzi, 2002) or in August 2013, when a bloom of *Dolichospermum lemmermannii*, a cyanobacterial species that produces surface scum, made lake waters unsuitable for bathing or drinking for several days (Bresciani et al., 2016a). Again, in summer 2016 an extended cyanobacteria bloom was detected (see Sec. 6.3).

3.1.4 Lake Iseo

Figure 12 Lake Iseo: view of Monte Isola from Tavernola Bergamasca (BG).

Lake Iseo (Figure 12) is the fourth lake for dimensions among subalpine lakes, extending for 61 km^2 with an average depth of 123 m and a total volume of 7.57 km^3, at 186 m a.s.l. Its water catchment is about 1777 km^2, where the largest Italian glacier (Adamello) is located, and lake water level is regulated by the Sarnico dam. Its major inflows are Oglio river, also the main effluent, and Italsider Channel. In the lake centre it is located the largest and highest European lacustrine island, Monte Isola. East to the island the lake is shallower (<100 m), while deeper in the western part (Figure 13).

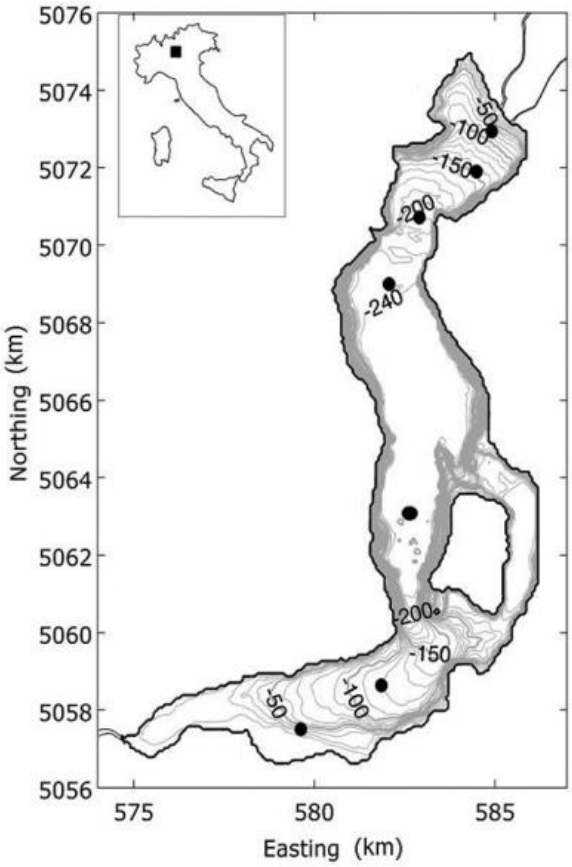

Figure 13 Lake Iseo bathymetry (source: Leoni et al., 2014)

The West coast is characterised by more rare vegetation, while the Eastern coast has gently sloping banks, more reach in vegetation. Wastewaters are collected to two treatment plants, one North and one South the lake. The lake underwent a relatively rapid eutrophication in the 1970s, mainly due to large nutrients loading from the inflows (Leoni et al., 2014).

Also Lake Iseo is oligomictic: complete overturn over the latest 20 years has happened only twice, and anoxic conditions have been established below 200 m (Valerio et al., 2014). An extended, not complete, vertical mixing occurred in 2009, up to 150 m depth (Rogora et al., 2018).

The concentration of chl-a and biomass of total phytoplankton and of different taxa in Lake Iseo varied significantly along water depth. In Leoni et al. (2014) analysis have been carried out over seven sites along the lake and four taxa, *Diatoma elongatum*, *Planktothrix rubescens*, *Mougeotia* sp., and *Sphaerocystis schroeteri* accounted for >90% of the total volume of the identified taxa, with depth of the deep chl-a peak ranging from 10 to 12 m (up to 15 mg m^{-3}). On the other hand, no significant variability in the spatial distribution among the sampling sites was found, probably due largely to horizontal water movements in the lake providing uniform conditions (Valerio et al., 2012). The area surrounding the lake is subjected to periodic winds, characterized by a daily

inversion (Valerio et al., 2014): predominant direction is the same of the north–south lake axis, with an average speed of 3.9 m/s.

3.2 Mantua lakes

Figure 14 Mantua lakes: view of Mantua city from Lake Superiore.

Mantua lakes (Figure 14) are the three lakes (Superiore, Di Mezzo, Inferiore) of the city of Mantua, created by the damming of the Mincio River in the XII century, in the Po Valley. Their total surface area is 6.21 km^2; Lake Superiore has a maximum depth of 10 m close to the city, but it is about 1.5 – 2 m deep in the major part of its extension; Lake di Mezzo has an average depth of 4 m, while Lake Inferiore depth is on average 4 – 5 m. In general, being excavated along the centuries (mainly to avoid the town flooding), the lake bathymetry is very complex and characterized by the presence of channels (ARPA Lombardia, 2005). Vasarone (since 1190) and Vasarina (hydroelectric power plant built in 2015) dams are regulating the flow between the Superior and Middle lakes. The residence time of water in the three lakes is about 8.4, 1.9 and 2.5 days, respectively (Bresciani et al., 2009). Water usage is primary industrial, hydroelectric and recreational. The

surrounding district is strongly industrialized due to the presence of the water as an easy accessible source for both goods transportation and for industrial processes. This industrialization process and the demographic growth Mantua underwent after the second World War brought increasing pressures over the ecosystem (industrial and civil waste water were discharged to lake waters without any treatment until 80s).

All the three lakes are characterised by eutrophic levels, high turbidity (Secchi disk depth < 1 m in summer, Pinardi et al., 2018), and excess growth of macrophitic vegetation. During the vegetative period (April – October), a large part of the surface of the lakes is covered by dense stands of emergent macrophytes such as *Nymphea lutea*, *Trapa natans* and *Nelumbo nucifera* (the lotus flower) (Villa et al., 2017), since 2004 cut and harvested, to reduce their accumulation on the bottom.

Phytoplankton communities in Mantua lakes are characterized by the presence of diatoms in spring, cyanophytes and chlorophytes in summer (Pinardi et al., 2011), with cyanobacteria blooms more recurrent in recent years (Pinardi et al., 2018). Finally, in the latest years, a reduction of the water flow together with nutrients loads is bringing a rapid accumulation of organic matter in the lakes (Pinardi et al., 2011).

3.3 Lake Trasimeno

Figure 15 Lake Trasimeno, view from Castiglione del Lago (PG).

Lake Trasimeno (Figure 15), a post-tectonic lake situated in central Italy, is the fourth largest Italian lake (124 km^2). The lake is almost round with a diameter of about 11 km, but very shallow, with the maximum depth around 6 m (mean depth is 4.5 m). Due to this fact, water temperature is significantly conditioned by air temperature and solar irradiation, and thus the lake is strongly subjected to evaporation (125-150 m^3/year, ARPA Umbria, 2012). The lake hosts three small islands (Polvese, Maggiore, Minore) in the south-eastern part (ARPA Umbria, 2012).

The catchment area is relative small compared to the lake (309 km^2), mainly characterized by hills and small plains, closer to the western coast. Along its coasts, the most important activities are tourism, agriculture and livestock breeding with cultivated lands covering about 70% of its catchment. In addition, the lacustrine ecosystem represents an area of exceptional value for flora and fauna richness and species diversity.

The lake shows from mesotrophic to eutrophic conditions, for which principal critical parameters are phosphorous and chl-a concentrations. The lake is not stratified and thus sediments resuspension phenomena and phytoplankton blooms (including cyanobacteria blooms) occurred very often and are characterized by the presence of *Microcystis* spp*., Snowella* spp*., Planktothrix* spp*., Oscillatoria* spp*., Aphanizomenon* spp*.* and *Cylindrospermopsis raciborskii* (Ventura, 2003). Being the lake itself one third of the total area of the entire catchment area, response to precipitation by its waters level is very fast. A negative trend in precipitation was recorded between 2009 and 2012 (Figure 16), which enhanced the effects of anthropic pressure over lake, due mainly to civil wastewaters, agricultural, livestock farming, and tourisms activities. In 2013, an increase in precipitation amount allowed to restore and exceed the hydrometric zero level.

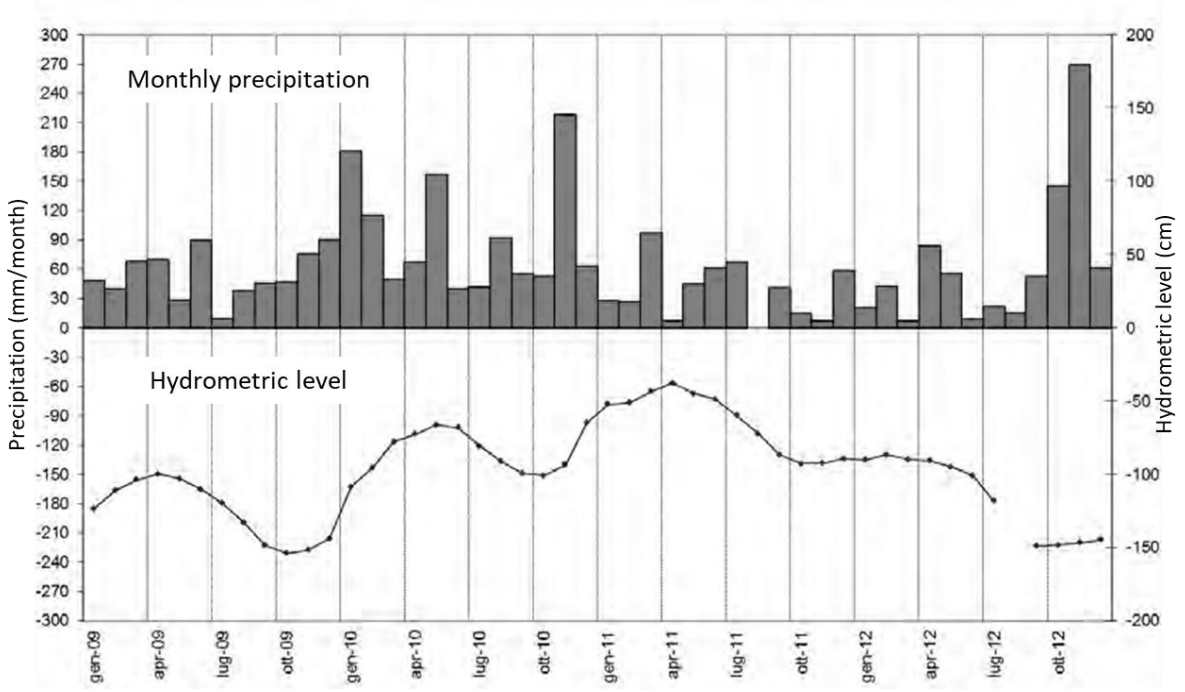

Figure 16 Monthly total precipitation and hydrometric level for 2009-2012. Source (ARPA Umbria, 2014, modified).

In Lake Trasimeno, phytoplankton monitoring is carried out every two months in one pelagic station (Centro Lago), and one station between the South-East coast and Polvese Island (Oasi, Figure 2). In the period 2009-2011, in the Pelagic station 703 species were identified (769 in the more coastal one), with Cyanobacteria prevailing, followed by, in order, Chlorophyceae, Diatoms, and Cryptophyceae (Arpa Umbria, 2014). Average measured chl-a for station Centro Lago (Oasi) was respectively, 5.19(3.91), 1.98(2.21), 3.68(2.35), ~11(~7.5), ~10(~10), ~5(~5.5) mg m^{-3} for 2009, 2010, 2011, 2013, 2014, 2015 (ARPA Umbria 2012, 2017), with highest peaks recorded in September (2009-2011).

3.4 Curonian Lagoon

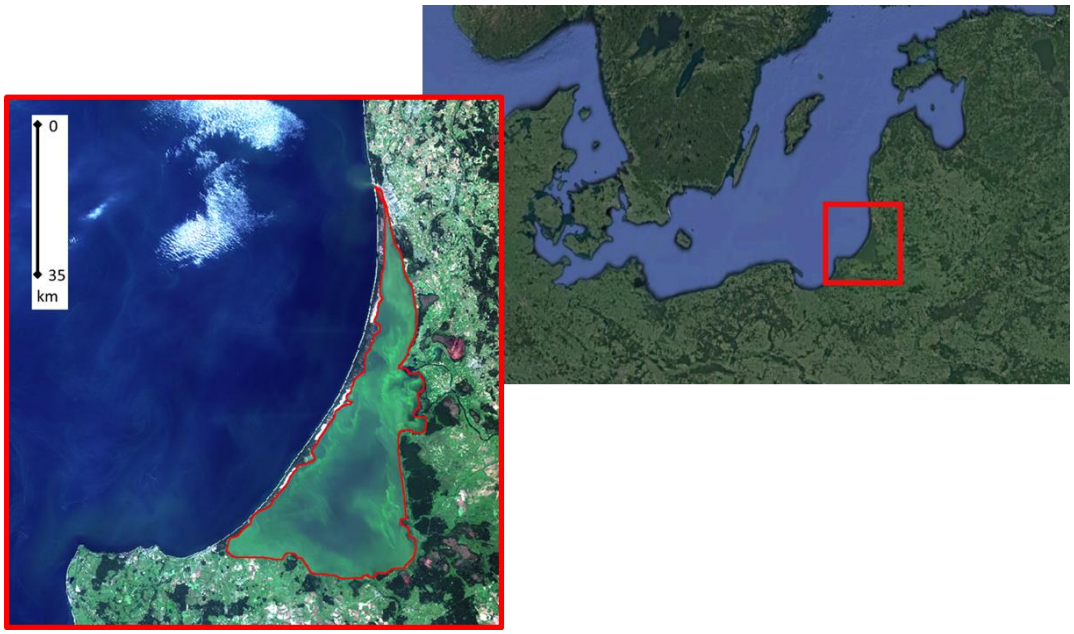

Figure 17 Curonian Lagoon (in red).

The Curonian Lagoon is a shallow coastal water body, 1584 Km^2 large (Gasiūnaitė et al., 2008), separated from the Baltic Sea by a narrow, dune-covered sand spit (the Curonian Spit), and connected only through the navigable Klaipéda Strait. It lies between Lithuanian and Russian territories. The mean depth is about 3.8 m and total volume about 6.2 km^3. The east coast of the lagoon is low, forested wetland, part of which forms the Nemunas River delta. The west coast is represented by the Curonian Spit, declared national park and included in the UNESCO World Heritage List. The residence time of lagoon water in the northern basin, close to the strait, is about 77 days, while the average for the southern basin is nearly 200 days (Jakimavičius, et al., 2018). Its salinity varies, depending on the ratio between the amount of brackish water inflow through the Klaipéda Strait and the amount of fresh water coming from the Nemunas River. In the period 1986-2005, salinity in the Curonian Lagoon from North to South was 2.5 ppt (parts per thousand) at Klaipéda, 1.2 ppt at Juodkranté, and less than 0.1 ppt at Venté and Nida (Jakimavičius, et al., 2018).

The lagoon is interested by large cyanobacterial blooms in summer-autumn seasons, producing the typical phenomenon of the scum, due to their superficial accumulation. The presence of cyanobacterial toxic metabolites in the Curonian Lagoon has been investigated and demonstrated for the first time in the work of Aisté et al. (2009) in 2006 when *Microcystis aeruginosa* was the most common species with *Nodularia spumigena* in the northern part of the Curonian Lagoon.

4. Materials and methods

4.1 Spaceborne Sensors for water quality analysis

Aiming at producing a long time series of chl-a maps for long term and phenology trend analysis, in this thesis activities, different sensors have been used, depending on their availability, selected among others, on the basis of their characteristics and performances. Several sensors imagery were in fact available for the latest decades, but not all sensors are suitable for inland water monitoring scope.

Starting with CZCS launched in 1978, whose every parameter was optimized for its usage over water, several satellite optical sensors, either dedicated or not, have been exploited for ocean colour monitoring. Among them, past and currently main sensors operating over Europe are listed in Table 3.

Table 3 Ocean Colour dedicated optical sensors main characteristics.

SENSOR	SATELLITE	Time availability	Spatial resolution (m)	N. bands	Spectral coverage (nm)	Revisiting time
MODIS-Aqua	Aqua	2002-today	250/500/1000	36	405-14385	1-2
MODIS-Terra	Terra	1999-today	250/500/1000	36	405-14385	1-2
OLCI	Sentinel 3A	2016-today	300/1200	21	400 - 1020	1-2
OLCI	Sentinel 3B	in commissioning phase	300/1200	21	400 - 1020	1-2
VIIRS	Suomi NPP	2011-today	375 / 750	22	402 - 11800	1
VIIRS	JPSS-1/NOAA-20	2017-today	370 / 740	22	402 - 11800	1
MERIS	ENVISAT	2002-2012	300	15	390-1040	1-2

Even if not specially designed for inland waters monitoring, these sensors have been fully exploited also by the inland water remote sensing communities.

Table 4 Non Ocean Colour dedicated optical sensors main characteristics.

SENSOR	SATELLITE	Time availability	Spatial Resolution (m)	n. bands	Spectral coverage (nm)	Revisiting time
MSI	Sentinel-2A	2015-today	10/60	13	443 – 2190	10
MSI	Sentinel-2B	2016-today	10/60	13	443 – 2190	10
OLI	Landsat-8	2013-today	30	7	443 – 2201	16

On the other hand, not all these sensors are suitable for any inland water basin monitoring, due primary to too low spatial resolution, which prevents their usage for basins of medium-small dimension, like some of the Italians lakes included in this study. In addition to the trade-off between spatial and temporal resolutions, also radiometric resolution and band availability along sensors need to be taken into account in the choice of the most suitable sensor, depending on lake characteristics and on the goal of the analysis itself.

In the past, a good compromise between medium spatial resolution and overpass frequency useful for rapid changes in water colours tracking, was reached with MEdium Resolution Imaging Spectrometer Instrument (**MERIS**) on board of the European ENVISAT-I, launched in 2002 (Sec. 4.1.1). MERIS provided a long time series imagery of more than 10 years, with a nominal overpass frequency of 1-2 days, allowing long term analysis. Its imagery has bene successfully used in inland waters (e.g. Gons et al., 2002, 2008; Kutser et al., 2006; Gitelson et al., 2008; Giardino et al., 2010; Guanter et al., 2010; Matthews et al., 2010; Odermatt et al., 2010; Binding et al., 2011; Bresciani et al., 2011; Matthews et al., 2012; Stumpf et al., 2012; Palmer et al., 2015b).

In Odermatt et al. (2010) and in GLaSS project (WP5, 2015) this sensor products, obtained through Case-2-Regional processor and Maximum Peak Height (MPH, Matthews et al., 2012), were fully validated also over Italian lakes and they have thus been exploited in this thesis for long term and phenology analysis over Lake Garda and Lake Trasimeno (Sec. 6.1).

After the loss of ENVISAT-I, waiting for its successor Ocean and Land Colour Instrument (**OLCI**), on board of the twin satellites Sentinel3-A and B (Sec. 4.1.3), Operational Land Imager (**OLI**) on-board NASA Landsat-8 satellite (Sec. 4.1.4) and MultiSpectral Instrument (**MSI**) on-board ESA Sentinel-2A and B twin satellites were exploited. Despite the fact that these sensors were not specifically designed for water monitoring, they are both offering advanced opportunities for synoptic, fine-scale, and high-frequency monitoring applications in lakes, for detailed water quality analysis (Kutser, 2004; Pahlevan et al., 2014) due to their radiometric sensitivity (with 12-bit quantization) (Hedley et al., 2012; Dörnhöfer and Oppelt, 2016); their high spatial resolution and overpass

frequency (up to every 2–3 days combining L8 and S2 satellites over study areas, Bresciani et al., 2018); the improved spectral band configuration in the visible–near-infrared wavelengths spectral range. Several studies showed their capability of providing robust water quality parameters products (e.g. Giardino et al., 2014a; Lim and Choi, 2015; Lobo et al., 2015; Dörnhöfer et al., 2016; Toming et al., 2016; Vanhellemont and Ruddick, 2016; Martins et al., 2017).

Finally, in 2016, Sentinel-3A was launched, carrying on board OLCI sensor, which inherited MERIS characteristics, with spatial, time and spectral characteristics suitable for this thesis scope. Its launch in fact allowed starting validate and then fully exploit its imagery, expected (with the consecutive launch of twins satellites, one of them already launched in April 2018, and in commissioning phase at the time of writing) to provide a long data series.

4.1.1 MERIS

MERIS is a programmable, medium-spectral resolution, imaging spectrometer operating in the visible and Near Infrared spectral range with 15 bands (Table 5). It was on board the ESA ENVISAT-I, launched in March 2002 and whose contacts were lost in May 2012. MERIS was dedicated to Land (Vegetation), Ocean and Coast and atmosphere (Clouds and Precipitation). The instrument was a so-called *push-broom* spectrometer, with linear CCD arrays providing spatial sampling in the across-track direction, while the satellite's motion provided scanning in the along-track direction.

Table 5 MERIS bands characteristics and application (Source: ESA, https://earth.esa.int/web/guest/missions/esa-operational-eo-missions/envisat/instruments/meris/design. Last accessed on 5/3/2018).

Band	Band centre (nm)	Bandwidth (nm)	Potential Applications
1	412.5	10	Yellow substance and detrital pigments
2	442.5	10	Chlorophyll absorption maximum
3	490	10	Chlorophyll and other pigments
4	510	10	Suspended sediment, red tides
5	560	10	Chlorophyll absorption minimum
6	620	10	Suspended sediment
7	665	10	Chlorophyll absorption and fluorescence reference
8	681.25	7.5	Chlorophyll fluorescence peak
9	708.75	10	Fluorescence reference, atmospheric corrections
10	753.75	7.5	Vegetation, cloud
11	760.625	3.75	Oxygen absorption R-branch
12	778.75	15	Atmosphere corrections
13	865	20	Vegetation, water vapour reference
14	885	10	Atmosphere corrections
15	900	10	Water vapour, land

The instrument's 68.5° field of view around nadir covered a swath width of 1150 km and it was shared between five identical optical modules. Spatial resolution was double: 300 m at nadir over land and coastal area, and 1200 m over open ocean waters. Acquisition was at around 10:00 local time and temporal resolution was 1-2 days, in cloud free conditions.

4.1.2 OLI

Landsat-8 (L8), was launched in February 2013 and carries on board the Operational Land Imager (OLI) sensor and Thermal Infrared Sensor (TIRS). It is operating with a spatial resolution of 30 m at ground, acquiring images every 16 days (Irons et al., 2012; Roy et al., 2014), that might be reduced to 8–9 days in case target areas lie in two adjacent orbits (Brando et al., 2015). L8 is part of the global NASA Landsat Earth observation program that started in the 1970s.

OLI is a *push-broom* sensor employing a focal plane with long arrays of photosensitive detectors (Irons et al., 2012), to which a four-mirror anastigmatic telescope focuses incident radiation. Its field-of-view is 15 deg., covering a 185 km across-track swath. The spectral bands of OLI sensor, while similar to Landsat 7's ETM+ sensor, provide enhancement from prior Landsat instruments, with in addition a deep blue visible channel (band 1) specifically designed for water resources and coastal zone investigation, and a new infrared channel (band 9) for the detection of cirrus clouds. Spatial resolution is 30 m for OLI bands, while 100 m for TIRS bands, but TIRS products are registered to and delivered with the 30-meter OLI data product.

4.1.3 MSI

The Sentinel-2 mission is a constellation of two satellites, designed for land monitoring, providing high resolution optical imagery, expected to be used in continuity with SPOT and Landsat missions. Sentinel-2A was launched on 23 June 2015 and Sentinel-2B on 7 March 2017. The mission main objectives are: land observation (vegetation, soil and water cover, inland waterways and coastal areas), land use and change detection maps, support in generating land cover, disaster relief support, climate change monitoring.

Sentinel-2A/B carry on board MSI (Multispectral Imager), a push-broom sensor designed and built by Airbus Defence and Space, France. It acquires in 13 spectral bands (Table 6), ranging from the visible to the shortwave infrared (SWIR) (Drusch et al., 2012), with a field of view of 20.6°, and a ground track width of 290 km, larger than previous multi-spectral optical missions such as SPOT and Landsat. It has two distinct arrays of 12 detectors mounted on each focal plane covering VNIR and SWIR channels respectively. The 12 detectors on each focal plane are in a staggered

configuration to cover the entire field of view. Bands have different spatial resolution from 10 m to 60 m (Table 6), with an overpassing frequency of 5 days, and even less (2-3) for some of the study areas included in this work, which lie in two different orbits.

Each satellite has a seven years lifetime design and are supposed to be replaced, in the framework of ESA's Copernicus Program, in 2022-2023 by new identical missions taking the data record to the 2030 timeframe.

Table 6 MSI bands central wavelength, spatial resolution and main purpose for each band.

Band	Resolution (m)	Central wavelength (nm)	Band width (nm)	Purpose
B01	60	443	20	Aerosol detection
B02	10	490	65	Blue
B03	10	560	35	Green
B04	10	665	30	Red
B05	20	705	15	Vegetation classification
B06	20	740	15	Vegetation classification
B07	20	783	20	Vegetation classification
B08	10	842	115	Near infrared
B08A	20	865	20	Vegetation classification
B09	60	945	20	Water vapour
B10	60	1375	30	Cirrus
B11	20	1610	90	Snow / ice / cloud discrimination
B12	20	2190	180	Snow / ice / cloud discrimination

Respect to Landsat-OLI, MSI offers more spectral measurements within the near-infrared (NIR) region, advantageous over optically complex coastal/inland waters, for enhanced retrievals of TSM and chl-a concentration maps in hypertrophic, CDOM-rich, and extremely turbid waters (Pahlevan et al., 2017).

Despite its mission objectives, S2-MSI imagery is now intensively used for coastal and inland water quality maps retrieval, as several studies show (e.g. Dörnhöfer et al., 2016; Toming et al., 2016; Vanhellemont and Ruddick, 2016; Martins et al., 2017) as well as several projects outcomes (e.g. BLASCO[5], INFORM[6]), but also coral bleaching detection (Sen2Coral[7]).

[5] Blending LAboratory and Satellite techniques for detecting CyanObacteria (CARIPLO, 2014-2019).
[6] Improved monitoring and forecasting of ecological status of European INland waters by combining Future earth ObseRvation data and Models (European Union, FP7 SPACE, 2014-2017)
[7] SEOM S2-4Sci Land and Water: Coral Reefs (ESA's SEOM Programme, 2016-2017))

4.1.4 OLCI

Designed as the successor of ENVISAT-MERIS, Ocean and Land Colour Instrument, OLCI, with additional channels and a different camera arrangement, has as main missions the maritime monitoring, land mapping and monitoring, atmospheric monitoring and climate change monitoring.

The OLCI is a push-broom instrument with five camera modules sharing a field of view of 68.5°, (14.2° for each camera) overlapping by 0.6°, and with the whole field of view shifted across track by 12.6° away from the nadir, minimizing sun-glint effect (ESA OLCI Instrument Technical Guide).

Spatial resolution is around 300 m, used for the product grid of Full Resolution (FR) products, while the Reduced Resolution (RR) processing mode provides Level-1B data approximately 1.2 km.

Each cameras is equipped with a CCD array (Charge-Coupled Device), with image areas of 740 x 520 detectors (3700 ground pixels in total) for a spectral range between 390 and 1040 nm. Elementary spectral bands have a spectral resolution of about ~1.7 nm and a spectral sampling interval of ~1.25 nm (ESA, 2016). Binning the signal of consecutive CCD lines into variable width spectral bands, two imaging modes are possible: a 'raw mode' with 46 micro-bands (used during instrument calibration), and a 'nominal operating mode' with 21 micro-bands (plus one smear band) listed in Table 7.

Table 7 OLCI bands, with nominal central wavelength, width and main purpose for each band.

Band	λ centre (nm)	Width (nm)	Purpose
Oa01	400	15	Aerosol correction, improved water constituent retrieval
Oa02	412.5	10	Yellow substance and detrital pigments (turbidity)
Oa03	442.5	10	Chlorophyll absorption maximum, biogeochemistry, vegetation
Oa04	490	10	High Chlorophyll,
Oa05	510	10	Chlorophyll, sediment, turbidity, red tide
Oa06	560	10	Chlorophyll reference (Chlorophyll minimum)
Oa07	620	10	Sediment loading
Oa08	665	10	Chlorophyll (2nd Chlorophyll absorption maximum), sediment, yellow substance/vegetation
Oa09	673.75	7.5	For improved fluorescence retrieval and to better account for smile together with the bands 665 and 680 nm
Oa10	681.25	7.5	Chlorophyll fluorescence peak, red edge
Oa11	708.75	10	Chlorophyll fluorescence baseline, red edge transition
Oa12	753.75	7.5	O2 absorption/clouds, vegetation
Oa13	761.25	2.5	O2 absorption band/aerosol correction.
Oa14	764.375	3.75	Atmospheric correction
Oa15	767.5	2.5	O2A used for cloud top pressure, fluorescence over land
Oa16	778.75	15	Atmos. corr./aerosol corr.
Oa17	865	20	Atmospheric correction/aerosol correction, clouds, pixel co-registration

Band	λ centre (nm)	Width (nm)	Purpose
Oa18	885	10	Water vapour absorption reference band. Common reference band with SLSTR instrument. Vegetation monitoring
Oa19	900	10	Water vapour absorption/vegetation monitoring (maximum reflectance)
Oa20	940	20	Water vapour absorption, Atmospheric correction/aerosol correction
Oa21	1 020	40	Atmospheric correction/aerosol correction

4.2 Satellite images and processing chain

In order to obtain chl-a concentration maps, imagery needs to be processed along a processing chain (Figure 18), which includes radiometric correction (to obtain from digital numbers (DNs) extra-atmospheric radiance (Top OF Atmosphere, TOA, radiance)), atmospheric correction to obtain Remote sensing reflectance (Rrs), and finally the application of bio-optical models to obtain from Rrs chl-a concentration.

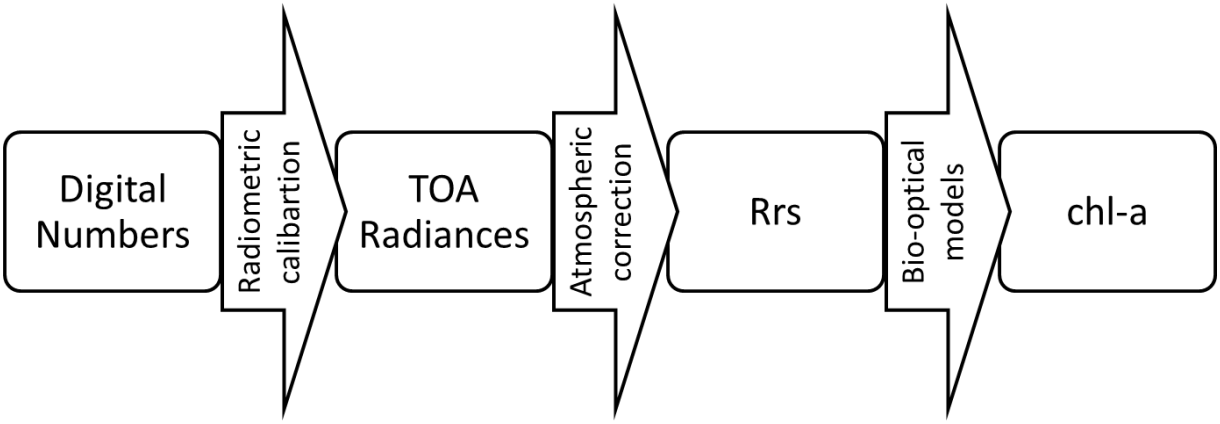

Figure 18 Processing chain for chl-a maps retrieval from satellite sensors imagery.

25 cloud-free OLI-L8 Collection 1 L1B images were downloaded from USGS *EarthExplorer* tool (https://earthexplorer.usgs.gov/), containing scaled and calibrated DNs. When needed (for ATCOR and 6SV-based processors), TOA radiances were obtained through *Radiometric calibration ENVI-IDL tool*.

45 cloud-free MSI-S2 L1C images were downloaded from Copernicus Open Access Hub, (https://scihub.copernicus.eu/dhus/), containing TOA reflectance. When required, before processing (thus for ATCOR and 6SV-based processors), all bands were resampled at 10 m through SNAP *S2-toolbox*, with nearest neighbour method, and TOA reflectance $\rho_{toa}(\lambda)$ was converted into $L_{toa}(\lambda)$ before being ingested by the interface for atmospheric correction through 6SV and by ATCOR, according the following equation:

$$L_{toa}(\lambda) = \frac{\rho_{toa}(\lambda)\, F_0(\lambda)\, U \cos(\theta)}{\pi} \; [Eq.5]$$

where $F_0(\lambda)$ is the extra-terrestrial solar irradiance for each band λ, U is the correction factor taking into account Earth-Sun distance variation, and θ is the solar zenith angle over each target pixel.

Both MSI and OLI images downloaded were already reprojected to UTM – WGS84 Zone 32 projection.

90 cloud-free OLCI-S3 L1B Full Resolution Non-Time-Critical (V2.23-2.29) images were downloaded from Copernicus Online Data Access (CODA) for the time series since October 2017 and from CODAREP (REProcessed) for the full reprocessed time series (April 2015 – September 2017). DNs images were converted into TOA radiances and reprojected to UTM – WGS84 Zone 32 through SNAP – *Sentinel-3 Toolbox.*

After atmospheric correction, Rrs obtained as described in the next sections for each algorithm/software, was then used to retrieve chl-a concentration maps through an ENVI-IDL tool BOMBER (Sec. 4.4.1) over subalpine lakes and Lake Trasimeno, and through a band-ratio based algorithm for Mantua lakes and Curonian Lagoon (Sec. 4.4.2).

4.3 Atmospheric correction algorithms

As shown is section 2.1.1, several algorithms, listed in Table 8, have been developed and validated over inland waters. A selection of algorithms and software have been tested, including those available for the current latest generation sensors, and already tested over similar water and environmental conditions for each sensor and study area. In addition, the comparison includes standard products as provided for each sensor.

For S2-MSI and L8-OLI, atmospheric correction products inter-comparison has been carried out among standard Level-2 (MSI only, through Sen2Cor), ACOLITE, ATCOR, 6SV. For S3-OLCI, the inter-comparison has been carried out among standard Level2 products, alternative NN products (through SNAP-C2RCC), 6SV and POLYMER. Each algorithm or software and actual parametrization or chosen options are described in ANNEX I.

Table 8 Summary of atmospheric correction processors compared in this study and main characteristics included.

PROCESSOR (options)	SENSOR	TARGET	Predefined aerosol	Microphysical properties	Image based	Glint correction	Adjacency correction
6SV DailyMicro	OLI, OLCI, MSI	Subalpine lakes		x			
6SV Seasonal Micro	OLI, OLCI, MSI	Subalpine lakes		x			
6SV predefined	OLI, OLCI, MSI	Trasimeno, Curonia	x				
ATCOR fixed	OLI, MSI	All	x				x
ATCOR varying	OLI, MSI	All	x		x		x
C2RCC	OLI, OLCI, MSI	All			x		
POLYMER	OLCI	All			x	x	
ACOLITE	OLI, MSI	All				x	

4.4 Water quality parameters retrieval algorithms

4.4.1 BOMBER tool

BOMBER (Bio-Optical Model Based tool for Estimating water quality and bottom properties from Remote sensing images, Giardino et al., 2012) is a tool, developed by the Institute for Electromagnetic Sensing of the Environment, National Research Council (IREA-CNR), in ENVI-IDL environment, for water quality parameters and bottom properties (bathymetry and substrate type) retrieval. It operates the inversion of spectral reflectance via a bio-optical model and uses optimization techniques, to retrieve from Rrs spectra, chl-a and TSM concentrations, $a_{CDOM}(440)$ and, in shallow waters, depth and substrate classification of the bottom. It is based on the works by Albert and Mobley (2003) and Lee et al. (1998, 1999). The above water remote sensing reflectance is expressed as a function of the subsurface radiance reflectance $r(0^-, \lambda)$, which is in turn the sum of the water column and, for shallow waters, the bottom contributions, respectively $r(0^-, \lambda)_c$, and $r(0^-, \lambda)_B$:

$$Rrs(\lambda) = \frac{\Pi(0^-, \lambda)}{1 - \gamma(0^-, \lambda)} \; [Eq. 6]$$

where Π and γ are model parameters which take into account the effects of air–water interface and $r_0^-(\lambda)$ is expressed, for optically deep waters (dp), as:

$$r(0^-, \lambda)^{dp} = (g_0 + g_1 u(\lambda)^{g_2}) u(\lambda) \; [Eq. 7]$$

For shallow waters, it is expressed as the sum of $(0^-, \lambda)$ due to the water column (c) and the bottom (b):

$$r(0^-,\lambda) = r(0^-,\lambda)_c + r(0^-,\lambda)_b = r(0^-,\lambda)^{dp}\left(1 - A_0 e^{\left(-\left(\frac{1}{\cos(\theta_w)} + D_u^B\right)\kappa(\lambda)H\right)}\right) + A_1\rho(\lambda)e^{\left(-\left(\frac{1}{\cos(\theta_w)} + D_u^B\right)\kappa(\lambda)H\right)}, \text{[Eq. 8]}$$

where the variables $\cos(\theta_w)$ and H are the cosine of the underwater sun zenith angle and the bottom depth, respectively. g_0, g_1, g_2, A_0, A_1, D_u^B, and K are model parameters defined in Lee et al. (1998, 1999). Their defaults values are based on Lee et al. (1999), estimated using radiative transfer numerical model *Hydrolight* (Mobley and Sundman, 2013) and can be changed by users, based on literature.

$u(\lambda)$ is a function of the two IOPs $a(\lambda)$ and $b_b(\lambda)$, respectively total absorption and backscattering coefficients:

$$u(\lambda) = \frac{a(\lambda)}{a(\lambda) + b(\lambda)} \; [Eq. 9]$$

which are in turn modelled as functions of concentrations of water constituents. Finally, ρ_w is the bottom albedo, sum of the three substrate albedo, as can be defined in the model.

The optimization process is performed through the minimization of a target function δ which measures the spectral distance between modelled image derived for each water pixel (Eq. 10).

$$\delta = \sqrt{\sum_{\lambda} (Rrs(\lambda) - \widehat{Rrs}(\lambda))^2} \; [Eq. 10]$$

IOPs in the model are defined by the user, using site specific measurements of the absorption coefficients of pure water, phytoplankton, non-algal particles and coloured dissolved organic matter, the backscattering coefficients of pure water, phytoplankton and non-algal particles. In this study, the model, was parametrized using site specific IOPs gathered *in situ*, as described in Giardino et al. (2014a for Subalpine lakes, 2015b for Lake Trasimeno), based on a long term database of ~150 records from 2000 to date (Manzo et al., 2015).

4.4.2 Semi-empirical models

As defined in INFORM project (Hunter et al., 2017), spectral inversion of bio-optical modelling performed better for waters without the typical spectral chl-*a* features in the red-edge wavelength region, with a low chl-*a* concentration (<10 mg m^{-3}), while adaptive semi-empirical band-ratio

algorithms were more suitable for higher chl-*a* concentrations (up to 150 mg m^{-3}). Thus, to retrieve chl-a concentration in the hypereutrophic Curonian Lagoon and in Mantua lakes, a semi-empirical approach was exploited, obtaining concentration as:

$$Chla \propto \frac{Rrs(Ref\_peak)}{Rrs(Abs\_peak)} \text{ [Eq. 11]}$$

using a 2-bands ratio, where, $Rrs(Ref\_peak)$ is the relative maximum in the range 690-715 nm, and $Rrs(Abs\_peak)$ is the relative minimum in range 668-682 nm. For S2-MSI was thus used the band ratio B5/B4 and for S3-OLCI B11/B8. In particular the equations used for S3-OLCI and S2-MSI are, respectively shown in equations 12 and 13 (Bresciani et al., 2016b; Hunter et al., 2017; Pinardi et al., 2018):

$$chl\_a = 52.19 \frac{Rrs(708.75)}{Rrs(665.0)} - 32.07 \; [Eq. 12]$$

$$chl\_a = 76.36(\pm 2.29) \frac{Rrs(705)}{Rrs(665.0)} - 51.57(\pm 0.26) \; [Eq. 13]$$

4.5 Ancillary data

4.5.1 Ground-based data

In order to parametrize 6SV interface and ATCOR in the 'fixed' mode (see Annex I), ancillary data as aerosol microphysical properties, aerosol, water vapour and ozone concentration were needed.

Aerosol Optical Depth at 550 nm (AOD550), which gives information about the aerosol load over study areas, and the other microphysical aerosol properties were extracted from AERONET (AErosol RObotic NETwork) time series, available for Lake Garda (Sirmione_Museo_GC site, 45.50N, 10.61E) and Lake Maggiore (Ispra site, 45.80N, 8.63E).

AERONET is a remote sensing aerosol monitoring network initiated by NASA and now spread globally with the aim of supporting NASA, CNES and NASDA Earth Observation satellite systems. The network is composed by CIMEL CE-318 sun-photometers (Figure 19), automatically Sun and sky scanning spectral radiometers, which provides, through direct estimation from measurements, columnar water vapour concentration and AOD at different wavelengths. This instrument has approximately a 1.28° full angle field-of-view, with two detectors to measure direct sun, aureole, and sky radiance, and a collimator of 33 cm. The sun is pointed with a precision of 1° and a four-

quadrant detector tracks the Sun precisely, before starting doing any sequence of measurements. Measurements are not contaminated by rain thanks to a sensor of humidity, preventing the instrument from leaving the 'park' position in case of rain.

Figure 19 CIMEL CE-318 instrument in AERONET Sirmione_Museo_GC site.

The instrument performs several and different sequences of Sky or radiance measurements in several wavelength between 340 and 1640 nm. The direct Sun measurements are made every about 15 minutes, to measure air mass, in eight spectral bands, in triplet (taking a total of about 30 seconds): variation in the triplets can usually be used to screen clouds. Sky measurements are performed in series: the first Sky measurement is made after the Sun triplets at 20° from the Sun. Then, aureole and sky radiances observations through a large range of scattering angles are made to retrieve size distribution, phase function, and aerosol optical thickness. Sky radiance sequence are divided into Almucantar and Principal Plane types: an almucantar is a series of measurements taken at the same elevation angle of the Sun for several azimuth angles, the number of which depends on the solar zenith angle, repeated for each channel. Almucantar sequences are made daily at an optical air mass of 4, 3, 2, and 1.7 both morning and afternoon, in addition to sequences hourly done between 9 a.m. and 3 p.m. (local solar time). A direct Sun observation completes the almucantar sequence. Principle plane sequences, on the other hand, make the sky measurement in the principal plane of the Sun, hourly with an air mass lower than 2.

In addition to the direct products, an inversion of sky radiances measurements and AOD provides size distribution, complex refractive index and partition of spherical/non-spherical particles. Estimated from these last, phase function, single scattering albedo, spectral and broad-band fluxes are provided (Dubovik and King, 2000; Dubovik et al., 2002, 2006). There are some assumptions on

the basis of this inversion: aerosol particles partitioning into spherical and non-spherical, plane-parallel atmosphere, homogeneous aerosol vertical distribution in the almucantar inversion and bi-layered for the principal plane inversion.

Direct products are publically distributed through AERONET Data Display Interface (https://aeronet.gsfc.nasa.gov/) at 1.0 (all the measurements), 1.5 (automatically screened for clouds and invalid data), and 2.0 (manually inspected) quality levels; inversion products are provided only at 1.5 and 2.0 quality levels. Since manually inspection requires some time, and level 2.0 data usually come after about one year, for the purpose of atmospheric correction in this thesis, when level 2.0 data were not yet available, level 1.5 data were used.

For Sirmione and Ispra sites, instruments perform measurements at 340, 380, 440, 500, 675, 870, 1020, 1640 nm and at 412, 443, 490, 555, 667, 870 and 1020 nm, respectively. AOD at 550 nm was thus retrieved exponentially interpolating available values along synchronous measurements (Figure 20) and through a weighted mean of the two closest measurements to satellite overpass (within 1 hour).

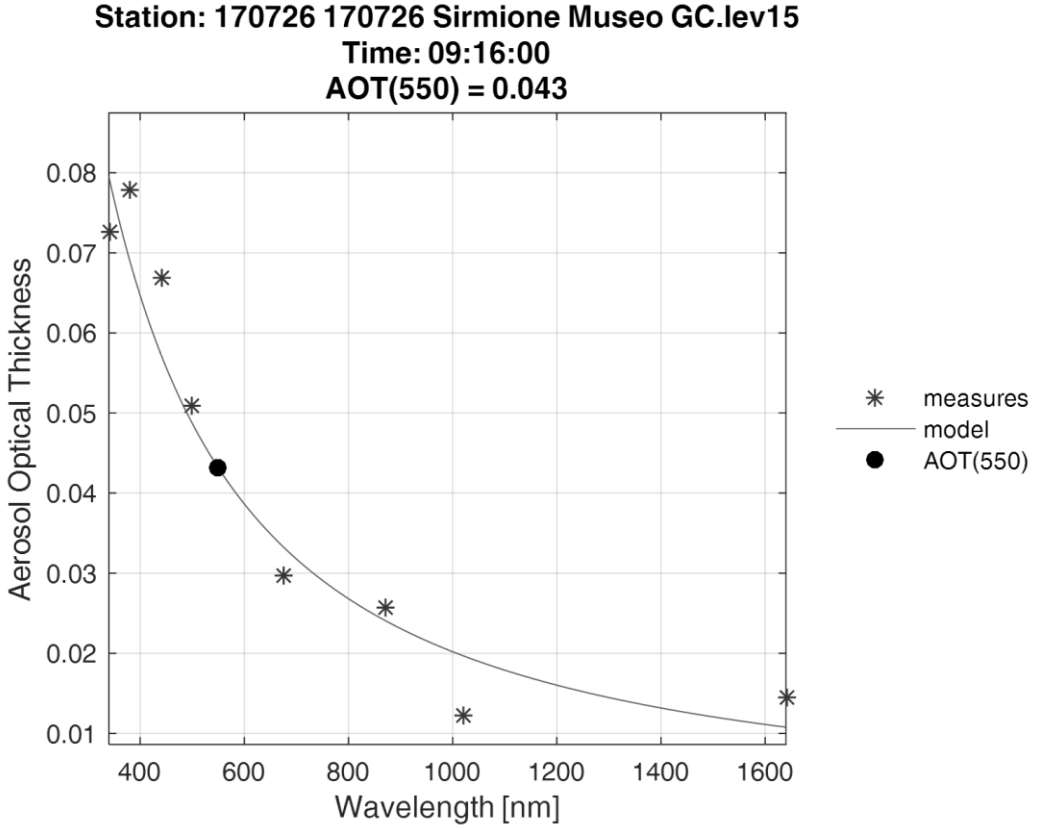

Figure 20 Example of AOD value retrieved at 550 nm from Sirmione site on 26th July 2017.

4.5.2 Satellite data

In order to parametrize 6SV, where no AERONET sites are available close to study areas, as described in Sec. 0, AOD values at 550 nm, ozone concentration and columnar water were retrieved from MODIS products through Giovanni interface. In particular, for AOD and columnar water, the Level-3 (L3) MODIS Atmosphere Daily Global Product MOD08_D3 (Platnick et al., 2015) was selected. It contains daily 1x1° grid values of atmospheric parameters related to aerosol particle properties, cloud optical and physical properties, atmospheric water vapour, atmospheric profile and stability indices. Terra was preferred to Aqua, when available, being closer in time to S3A/B and S2A/B overpass.

4.6 Field campaigns

In order to assess the accuracy of atmospheric correction algorithms/processors and compare their performances, Rrs products were compared to radiometric measurements collected *in situ*, usually within 3 hours from satellite overpass. Radiometric measurements were performed with CNR-IREA instrumentation with a WISP-3 (Hommersom et al., 2012), a spectroradiometer developed for gathering Rrs spectra of water in the range of 400–800 nm, as well as with a full range of radiometers (i.e. a FieldSpec ASD-FR and a SpectralEvolution (SE)), operating between 350 and 2500 nm, and operated according to Bresciani et al. (2013). In particular, WISP-3 simultaneously measures water and sky radiances at 40° at Nadir, and total irradiance, by three different optics and appropriate geometry.

ASD and SE can be deployed above and below water and their field of view (FOV) lenses can be changed. The measurements of water and sky radiances at 40° at Nadir, and total irradiance were sequentially acquired with the same radiometer, by mounting a remote cosine receptor and a 5° lens and keeping the angles consistent to the SeaWiFS protocol (Fargion and Mueller, 2000). Remote sensing reflectance Rrs was estimated, in accordance with Mobley (1999).

Both with WISP or ASD or SE, in each station, the sequence of measurements was repeated at least 3 times. Irradiance spectra were thus analysed to exclude any cast taken under very unstable sky conditions. Selected measurements were thus used to retrieve Rrs as in equation 14 (Mobley, 1999), where ρ_{sky} is set to 0.028, and C_a and C_b are two correction factors for wind speed, respectively 0.821 and -0.00004, with wind speed lower than 5 ms^{-1}, 1.63 and 0.002 otherwise.

$$Rrs(\lambda) = \frac{L_u(\lambda) - \rho_{sky} L_d(\lambda)\, C_a}{E_S(\lambda) + C_b} \quad [Eq.\,14]$$

In turbid eutrophic waters, spectral signature was adjusted according to Kutser et al. (2013) for glint effects removal through a power function, using reflectance values in the 350–380 nm range to determine the slope of the power function itself and values in the 890–900 nm range to determine the absolute value of glint.

In each stations, Rrs spectra obtained were thus averaged. Field campaigns over Lake Trasimeno were conducted in collaboration with ARPA Umbria.

To validate chl-a concentration maps, limnologic field campaigns were conducted: integrated water samples between the surface and the Secchi-Disk depth were collected by using a Van Dorn sampler. The water was then filtered *in situ* for subsequent laboratory analysis. Chl-a concentrations, extracted with acetone at 90%, were determined in laboratory (in the University of Parma for Italian casa studies, in Klaipeda University for Curonian lagoon samples) via spectrophotometric method (Lorenzen, 1967). In addition, chl-a concentration data, gathered from monitoring measurements by local authorities ARPA Lombardia, ARPAV, APPA Trento and Arpa Umbria, were used.

In addition to chl-a concentration, also Total Suspended Matter (TSM) concentration and Coloured Dissolved Organic Matter (CDOM), and phytoplankton absorption were measured during *in situ* campaigns, in order to characterise study site waters. In particular, this information was useful to parametrized the bio-optical model BOMBER (as described in Sec. 4.4.1). TSM was determined gravimetrically, and its organic and inorganic fractions were determined after incineration in muffle (450°C for 3 hours). *In situ* measurements of spectral absorption were obtained via filter pad technique. Values of the spectral absorption coefficients of phytoplankton and of non-algal particles (aNAP) were determined spectrophotometrically (Trüper and Yentsch, 1967). Finally, the backscattering coefficients of particles were measured in situ using a Hobi Labs Hydroscat-6.

Both radiometric and limnologic field campaigns conducted by CNR-IREA during the period of this thesis activity and data gathered from protection agencies are listed in Table 9, together with satellites simultaneously available.

Table 9 List of field campaigns by both CNR-IREA and Protection Agencies used for products validation.

Date	Area	Instrument	Rrs measurements	Water samples	Satellite overpass
10/04/2015	Garda	WISP-3	14	-	L8
15/07/2015	Garda	WISP-3	7	-	L8
22/07/2015	Maggiore	ASD	4	3	L8

Date	Area	Instrument	Rrs measurements	Water samples	Satellite overpass
30/07/2015	Maggiore	WISP-3	10	-	S2A
12/09/2015	Garda	WISP-3	20	-	S2A
15/09/2015	Garda	WISP-3	16	-	S2A
24/09/2015	Maggiore	ASD,WISP	8	3	L8
25/09/2015	Garda	WISP-3	10	-	S2A
19/10/2015	Maggiore	WISP-3	18	-	L8
22/05/2016	Garda	WISP-3	3	-	S2A,S3A
07/06/2016	Garda	-	-	2	S3A
28/06/2016	Garda	WISP-3	5	2	S2A,S3A
01/07/2016	Garda	WISP-3	5	4	L8, S2A, S3A
07/07/2016	Garda	WISP-3	7	-	S2A, S3A
28/07/2016	Mantua	SE,WISP-3	5	5	S2A
09/08/2016	Garda	-	-	2	S3A
17/08/2016	Garda	WISP-3	4	-	S2A, S3A
24/08/2016	Curonia	WISP-3	3	-	S2A, S3A
01/09/2016	Curonia	WISP-3	4	11	S3A
19/09/2016	Mantua	SE, WISP-3	5	5	S2A, L8
26/09/2016	Iseo	SE,WISP-3	5	5	S2A, L8
08/03/2017	Garda	SE, WISP-3	7	3	S2A, S3A
17/05/2017	Garda	WISP-3	4	-	S2A, L8
13/06/2017	Trasimeno	WISP-3	16	8	S2A, S3A
04/07/2017	Garda	-	-	2	L8
06/07/2017	Garda	WISP-3	6	-	S2A, S3A
07/07/2017	Garda	WISP-3	5	-	S3A
10/07/2017	Trasimeno	WISP-3	10	2	S2A, S3A
13/07/2017	Garda	WISP-3	6	-	S2B, S3A, L8
26/07/2017	Iseo	WISP-3	4	-	S3A
28/07/2017	Mantua	SE	4	4	S2B
01/08/2017	Como	WISP-3	3	2	S3A
02/08/2017	Garda	WISP-3	1	1	S2A, S3A
07/08/2017	Garda	WISP-3	3	-	S2B, S3A
05/09/2017	Trasimeno	WISP-3	8	2	S3A
18/09/2017	Trasimeno	WISP-3	8	-	S2A, S3A
21/09/2017	Garda	WISP-3	5	-	S3A
27/06/2018	Garda	WISP-3	4	-	S3A

4.7 S3-OLCI and S2-MSI derived maps inter-comparison

As already stated before, the potentiality to generate continuous water quality parameters maps from S2 images has become a topic of increased interest for inland water monitoring. On the other hand, since OLCI on S3A (and S3B in the future) has higher revisiting and multiple match-ups with S2A/B, it was examined in this thesis activities, as a surrogate for S2A/B for rapid assessment of products retrieval. The limit of OLCI to capture small scale variation of chl-a is presented as counterpart of its high revisiting time and sensor's radiometry. The analysis has been based on the use of a common image processing scheme, selected among the best performing ones, as evaluated in previous processor inter-comparison activity, for both sensors, and applied in Garda and Trasimeno lakes, having a range of water types from clear blue to turbid productive.

14 OLCI and the almost synchronous MSI L1B images were chosen, 8 for Lake Trasimeno and 6 for Lake Garda, based on their availability with clear sky conditions and low glint contamination risk. MSI-S2A/B L1C images were downloaded via Copernicus Open Access Hub, containing TOA reflectance. Images were first processed as described in Sec. 4.2.

Once obtained L_{TOA} values, images were atmospherically corrected using *6SV DailyMicro* for Lake Garda, and *6SV predefined* with continental aerosol type for Lake Trasimeno. Chl-a maps were thus derived from Rrs maps through BOMBER, as described in Sec. 4.4.1.

Synchronous chl-a maps were thus compared to assess similarities and differences in terms of concentrations and differences in capturing both chl-a concentration magnitude and spatial variability. To accomplish these goals, S3A products were co-registered with S2A/B corresponding images. Images were masked with the same mask, to avoid shallow waters and mixed pixels along coast.

For each couple of corresponding images, values were extracted from the whole map, and pixel values frequency violin plots (Hintze et al., 1998) for each date were produced. 3 by 3 OLCI pixels (and thus 90 by 90 MSI pixels) ROIs were defined over protection agencies monitoring stations and other 20 random points, distributed on the whole surface for Lake Trasimeno, and on the Southern part of the lake for Lake Garda. The narrower northern part of the lake showed in fact in validation high residual errors due to the orography of the high coasts surrounding this part of the lake. In addition, in order to assess not only potential differences in magnitude but also potentiality of MSI to catch variability at finer scale, maps were created and coefficient of variation was calculated over selected ROIs, where S2A/B-MSI seemed to catch more variability.

Finally, over regional protection agencies monitoring stations (sites: 'Sirmione/Padenghe' and 'Salò' by ARPA Lombardia and '371' by ARPAV Veneto over Lake Garda; 'Centro Lago' and 'Oasi' by ARPA Umbria over Lake Trasimeno), values obtained in each date were used to hypothetically classify waters according to Water Frame Directive classification, among different trophic levels, according to chl-a concentration limits defined in Wolfram et al. (2009).

4.8 Validation

Rrs values for each band were extracted and averaged over a 3 by 3 pixels window over measurements points, for each synchronous atmospherically corrected product. The extraction was performed though SNAP tool *Pixel Extraction*.

Validation was at first made at a band level, which stressed out a large overestimation for the first band of OLCI sensor, over Lake Garda (percentage error close to 250%). This band was thus excluded before processing images through BOMBER to retrieve chl-a maps.

In order to access accuracy not only in terms of magnitude, but considering also the shape of the spectrum, in addition to Root Mean Squared Error (RMSE, Eq. 15) for each band, χ^2 statistic was calculated for each match-up, as in equation 16:

$$RMSE = \sum_{i=0,n} \frac{\left(chla_{satellite,i} - chla_{in\ situ,i}\right)^2}{n} \quad [Eq. 15]$$

$$\chi 2 = \sum_{\lambda} \frac{(Rrs_{satellite,\lambda} - Rrs_{in\ situ,\lambda})^2}{Rrs_{in\ situ,\lambda}} \quad [Eq. 16]$$

including each λ band ingested by BOMBER and included in *in situ* instrument spectral range, i.e. those available from 412 nm to 708 nm for Garda and from 412 nm to 800 nm for Trasimeno and Curonian Lagoon.

The same method for the extraction was followed for chl-a maps validation, retrieving then accuracy in terms of Mean Absolute Error (MAE) for n samples over each lake:

$$MAE = \sum_{i=0,n} \frac{\left|chla_{satellite,i} - chla_{in\ situ,i}\right|}{n} \quad [Eq. 17]$$

For OLCI L2 Ocean Colour products, the recommended flags listed in Sentinel-3A Product Notice did not allow to retrieve any results from products, thus a less stringent set (the one in common for each type of L2 Ocean Colour products) was used: *WQSF_lsb.CLOUD,*

WQSF_lsb.CLOUD_AMBIGUOUS, WQSF_lsb.CLOUD_MARGIN, WQSF_lsb.INVALID, WQSF_lsb.COSMETIC, WQSF_lsb.SATURATED, WQSF_lsb.SUSPECT, WQSF_lsb.HISOLZEN, WQSF_lsb.HIGHGLINT, and *WQSF_lsb.SNOW_ICE.*

In order to compare results obtained by the different algorithms, only stations which were not masked for all the different atmospheric corrected products were included in the calculation, but all the valid match-ups are shown in Rrs spectra plots.

5. Results

5.1 Atmospheric correction products comparison and validation

5.1.1 Lake Trasimeno

Over Lake Trasimeno for **MSI** imagery, the best results were obtained by ACOLITE (old version), *6SV predefined and* ATCOR processors.

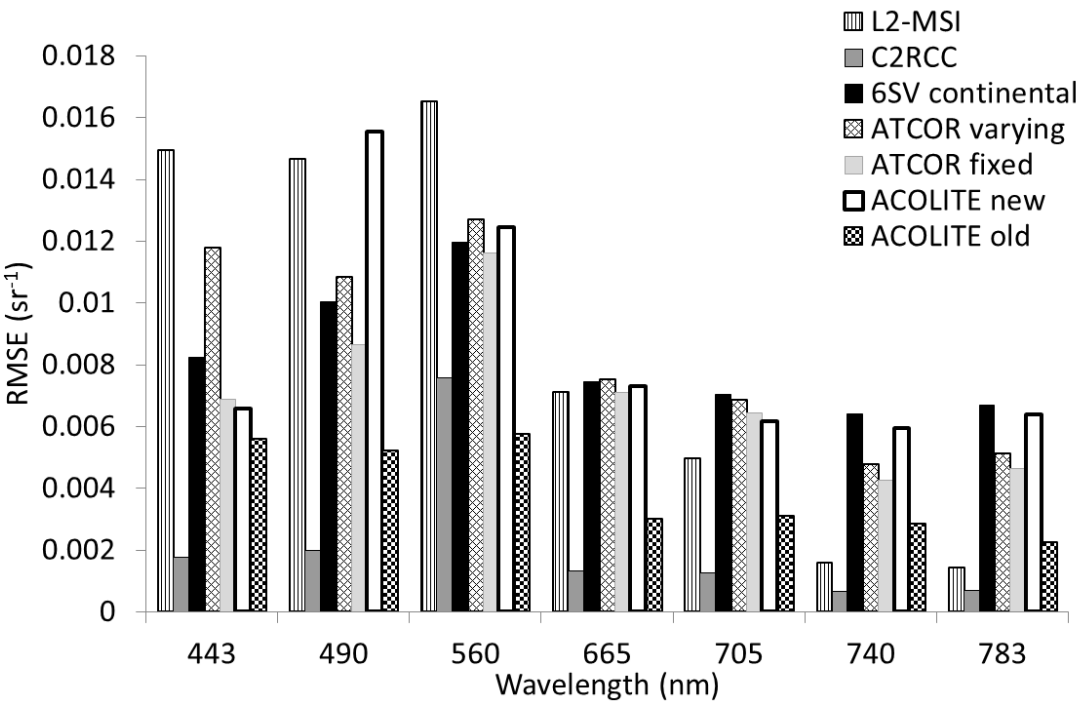

Figure 21 RMSE estimated for all the processors from S2A-MSI imagery, and in situ measured in Lake Trasimeno.

In fact, even if overestimating Rrs as measured *in situ* (as shown also by the larger error in terms of RMSE in Figure 21), 6SV, ATCOR (*varying* configuration) and ACOLITE (old version) provided the best results in terms of shape, as shown in Figure 22, in particular allowing to capture the characteristic peak at 705 nm, typical of high concentration of phytoplankton. In fact, although the lowest values of χ^2 were estimated for C2RCC (Figure 23), this processor, performed well with lower concertation conditions (as in 13th June 2017), but the peak observed *in situ*, in dates with very high concentration, was completely lost. This can be stressed comparing band ratio of band 6 (705 nm) over band 5 (665 nm) with the value observed *in situ*; MAE is reported in Table 10 for the two dates when chl-a measurements were available: it shows as, while *6SV continental*, *ATCOR*

varying, and ACOLITE (both versions) performances were stable, for C2RCC strongly worsen in presence of high values of chl-a concentration.

Table 10 MAE calculated between band ratio (B5/B6) by all the processors compared to in situ values. 'Failure' indicate that all pixels corresponding to the measurement points were masked out by the processor.

Date	6SV continental	ATCOR varying	ATCOR fixed	ACOLITE old	ACOLITE new	C2RCC	Level 2
13/6/2017 (low chl-a)	0.089	0.068	0.080	failure	0.045	0.037	0.068
18/9/2017 (high chl-a)	0.085	0.065	failure	0.058	0.049	0.408	0.090

On the other hand, *6SV continental* results, showed an overall overestimation, which could be due also to an underestimation of aerosol load, which, in case of Lake Trasimeno was derived from MODIS products.

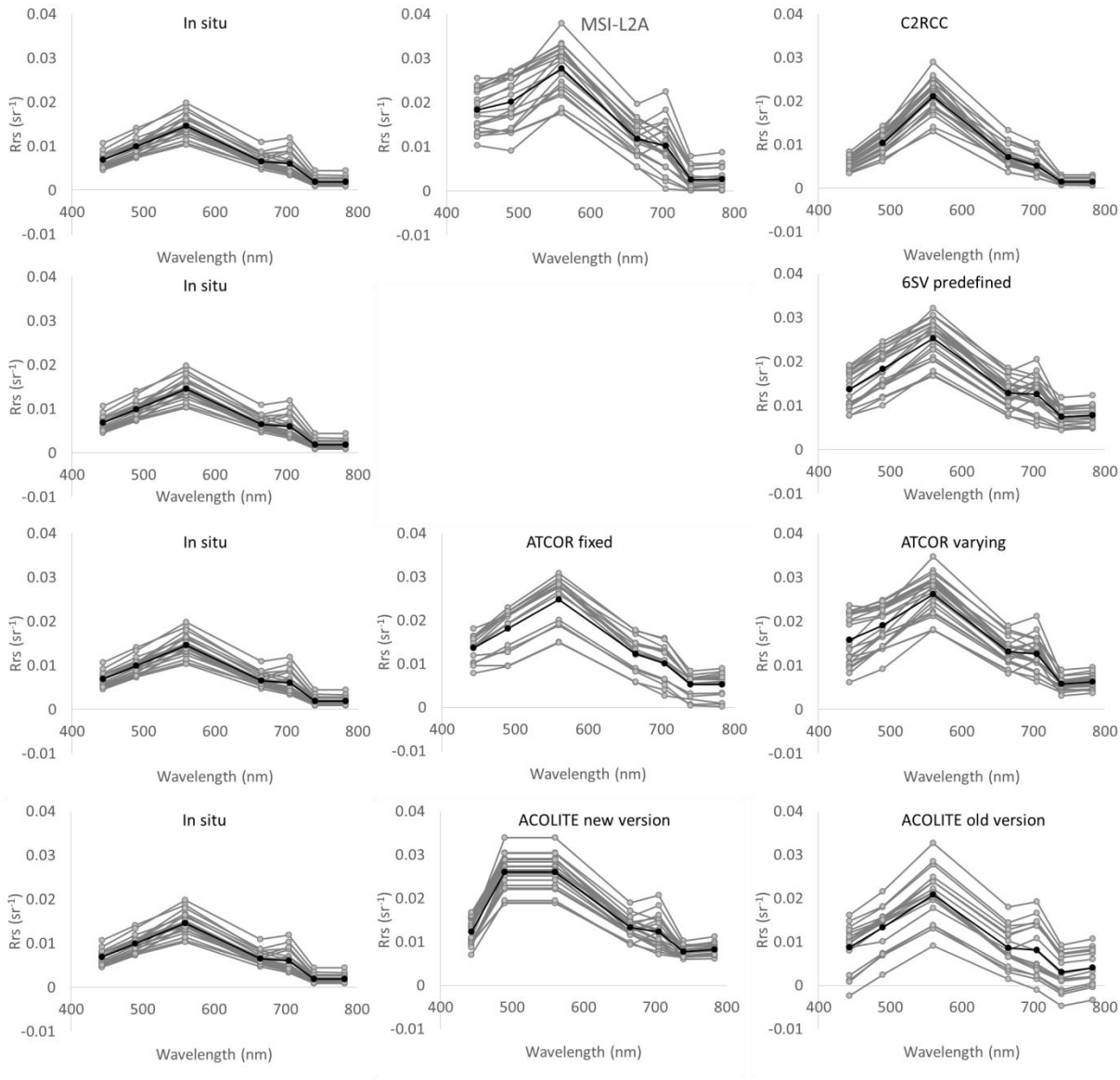

Figure 22 Rrs obtained through all atmospheric correction processors in Lake Trasimeno for all available match-ups, extracted from 3 by 3 ROIs over in situ measurements stations from S2A/B-MSI imagery and in situ measured. In situ plot is repeated to help visualization. Black line shows mean value for each processor (of in situ measurements in case of in situ plot). The empty space would have been reserved for '6SV dailyMicro' that does not exist for Trasimeno (because there is not any AERONET station nearby) but it has been generated in case of Garda (cf. Figure 28)

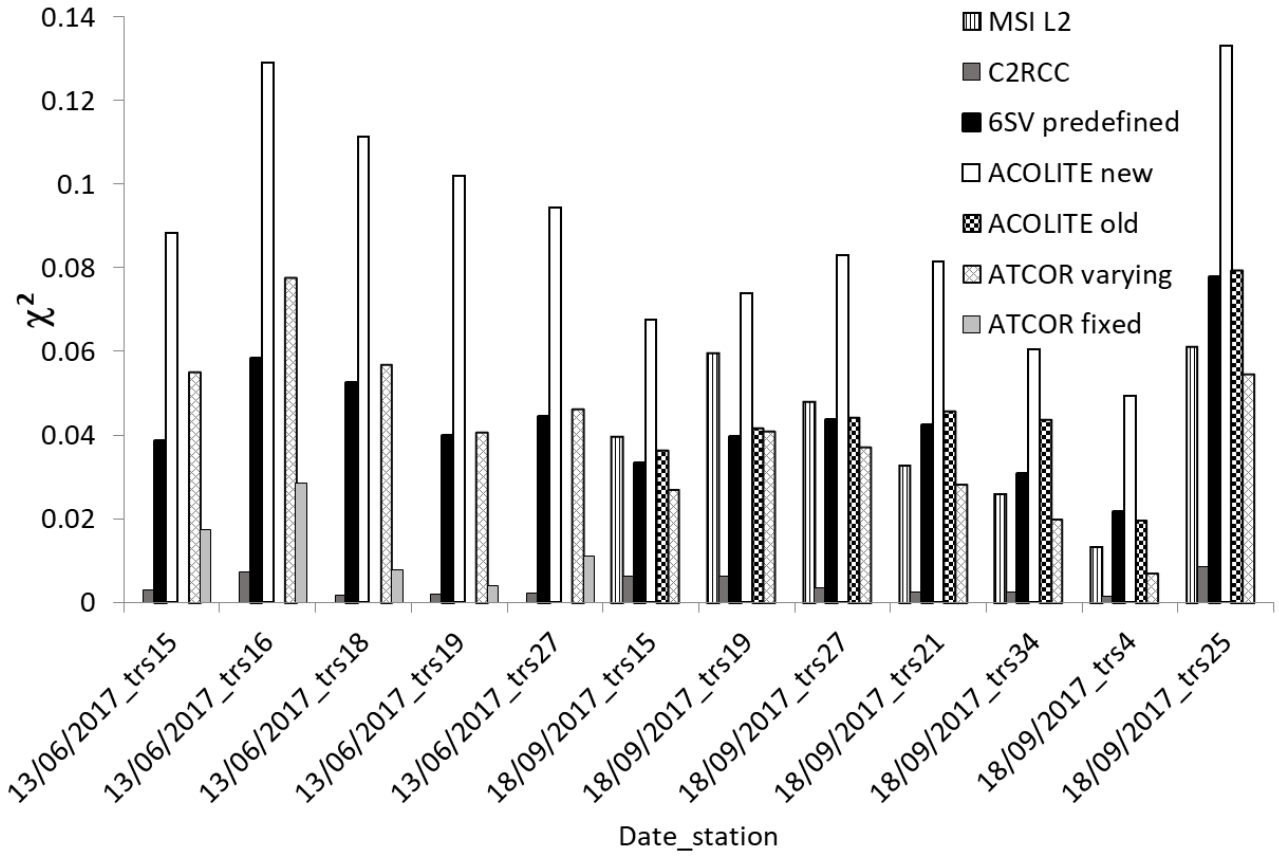

Figure 23 χ^2 estimated for all the processors from S2A-MSI imagery, and in situ measured in Lake Trasimeno.

ACOLITE new showed very bad performances in the green-blue region. Figure 22 shows although new version improved Rrs retrieval in NIR region (sometimes negative in the previous version), slope in the blue-green region were more accurate for *ACOLITE old* results. On the other hand, as shown later for chl-a validation, for the few available match-ups, chl-a algorithm embedded in *ACOLITE new* produced a very accurate estimation of chl-a concentration. More match-ups are thus needed to investigate the potentiality of this algorithm over this lake waters.

For **OLCI** products, the best results were obtained by *6SV predefined* and POLYMER (Figure 24), with POLYMER outperforming *6SV predefined* in every match-up as RMSE and χ^2 show (Figure 25, Figure 26): C2RCC processor again underestimated Rrs and missed the peak as for MSI results.

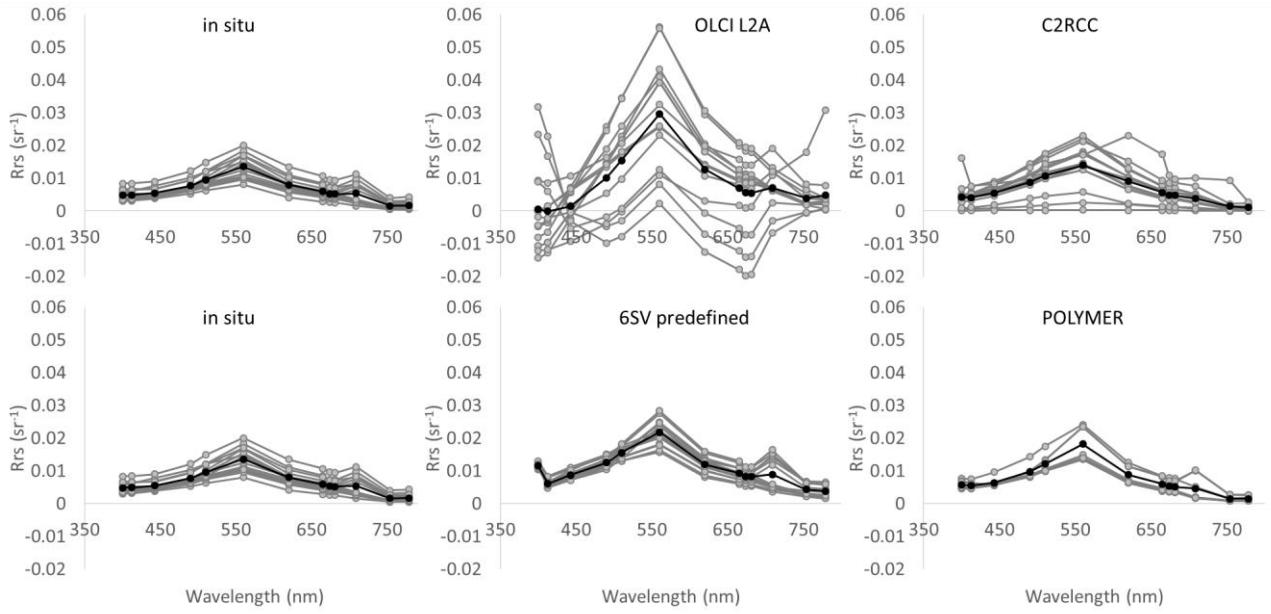

Figure 24 Rrs obtained through all atmospheric correction processors in Lake Trasimeno for all available match-ups, extracted from 3 by 3 ROIs over in situ measurements stations from S3A-OLCI imagery and in situ measured. In situ plot is repeated to help visualization. Black line shows mean value for each processor (of in situ measurements in case of in situ plot).

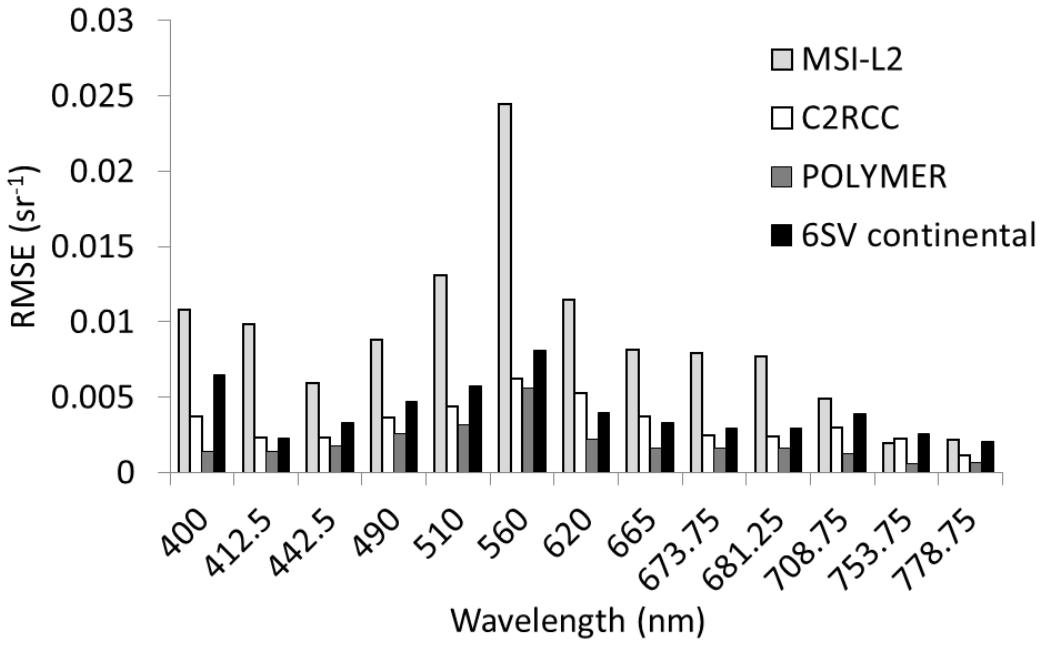

Figure 25 RMSE estimated for all the processors from S3A-OLCI imagery, and in situ measured in Lake Trasimeno.

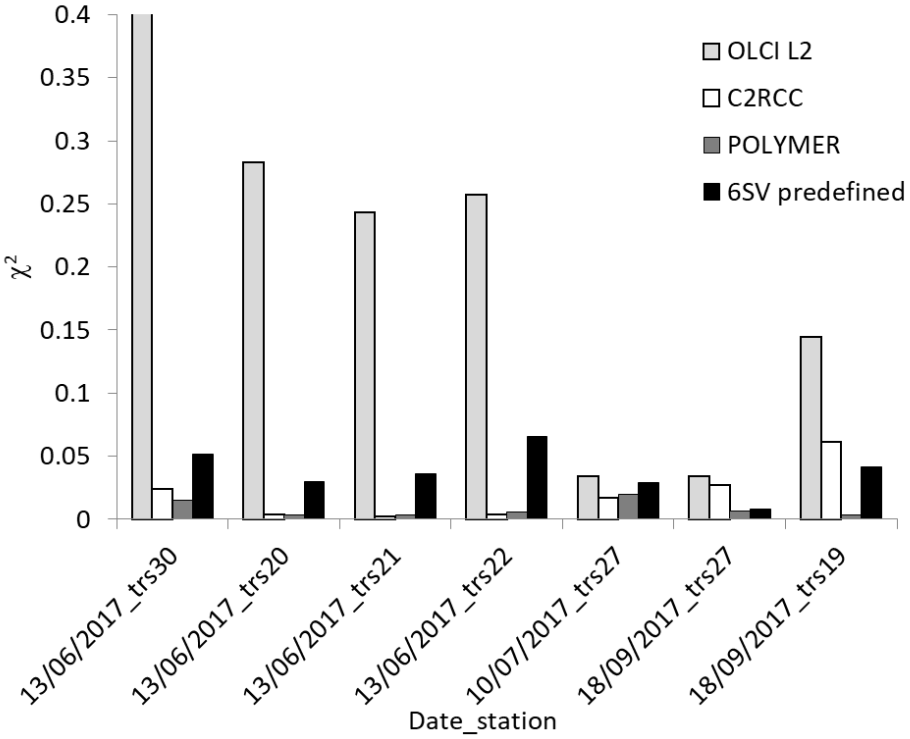

Figure 26 χ^2 estimated for all the processors from S3A-OLCI imagery, and in situ measured in Lake Trasimeno.

5.1.2 Subalpine lakes

For subalpine lakes, the best performance from **S2A/B-MSI** imagery considering band by band performances through RMSE (Figure 27) were obtained by C2RCC and ACOLITE (old version).

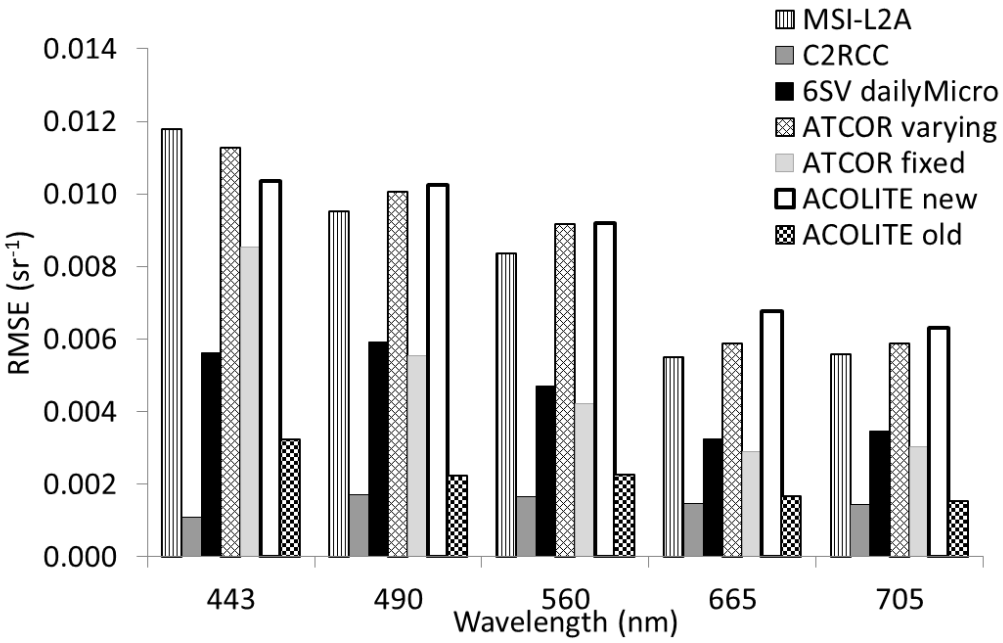

Figure 27 RMSE estimated for all algorithms from S2A/B-MSI imagery and in situ measured in subalpine lakes.

On the other hand, in terms of shape (Figure 28), the best results were obtained by the standard products MSI-L2, *ACOLITE new*, and 6SV (both *dailyMicro* and *seasonalMicro* configuration), mainly in dates when signal was stronger, as on 17th August 2016, during which a cyanobacteria bloom was observed. In fact, although the smallest values for χ^2 were retrieved from C2RCC match-ups (Figure 29), for very clear waters, as on 8th March 2017, C2RCC largely underestimated Rrs in the NIR region; in addition, it tends to anticipate the peak measured at 560 nm to 490 nm. The other processors failed in estimating the slope between the first two bands.

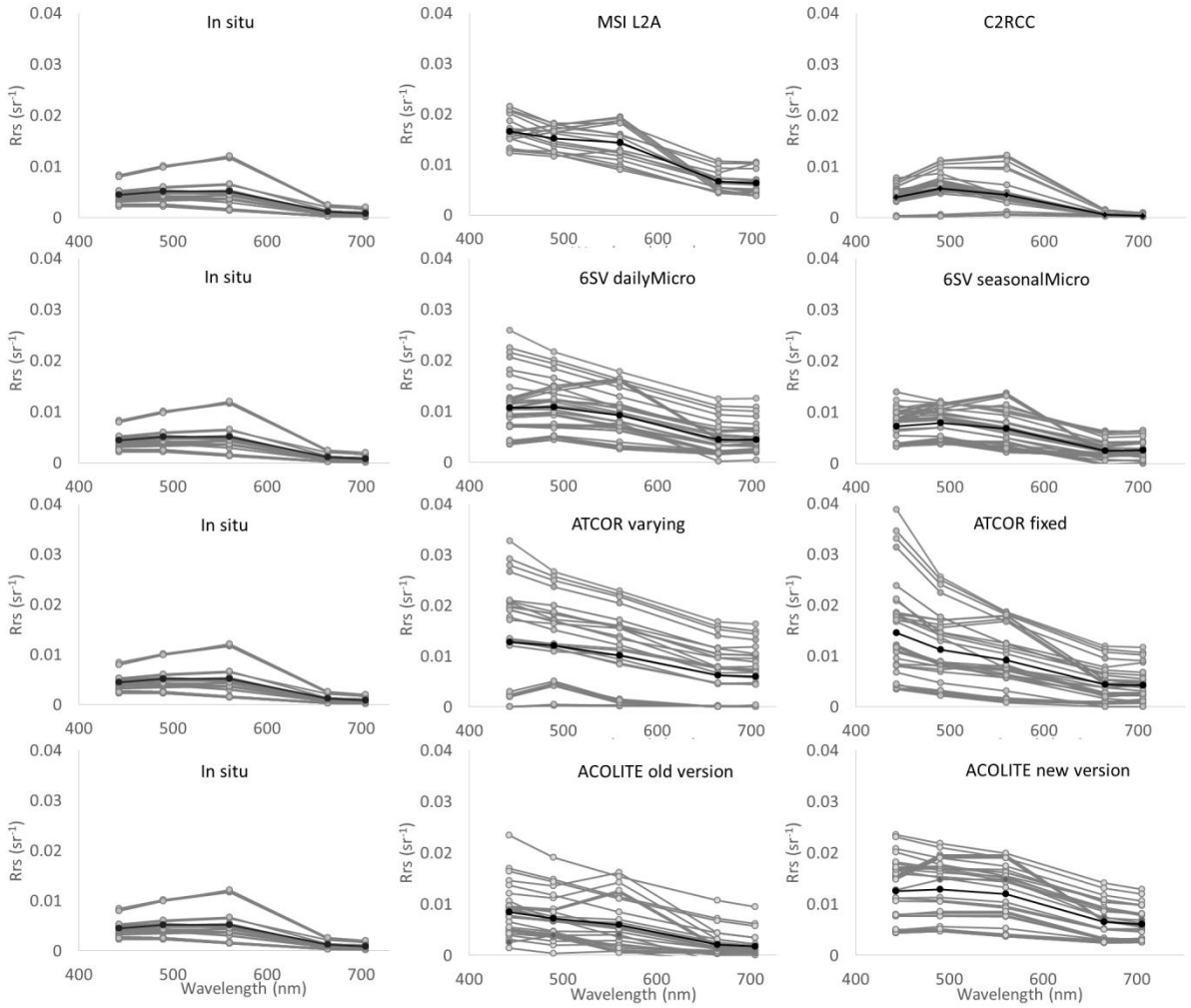

Figure 28 Rrs obtained through all atmospheric correction processors in subalpine lakes for all available match-ups, extracted from 3 by 3 ROIs over in situ measurements stations from S2A/B-MSI imagery and in situ measured. In situ plot is repeated to help visualization. Black line shows mean value for each processor (of in situ measurements in case of in situ plot).

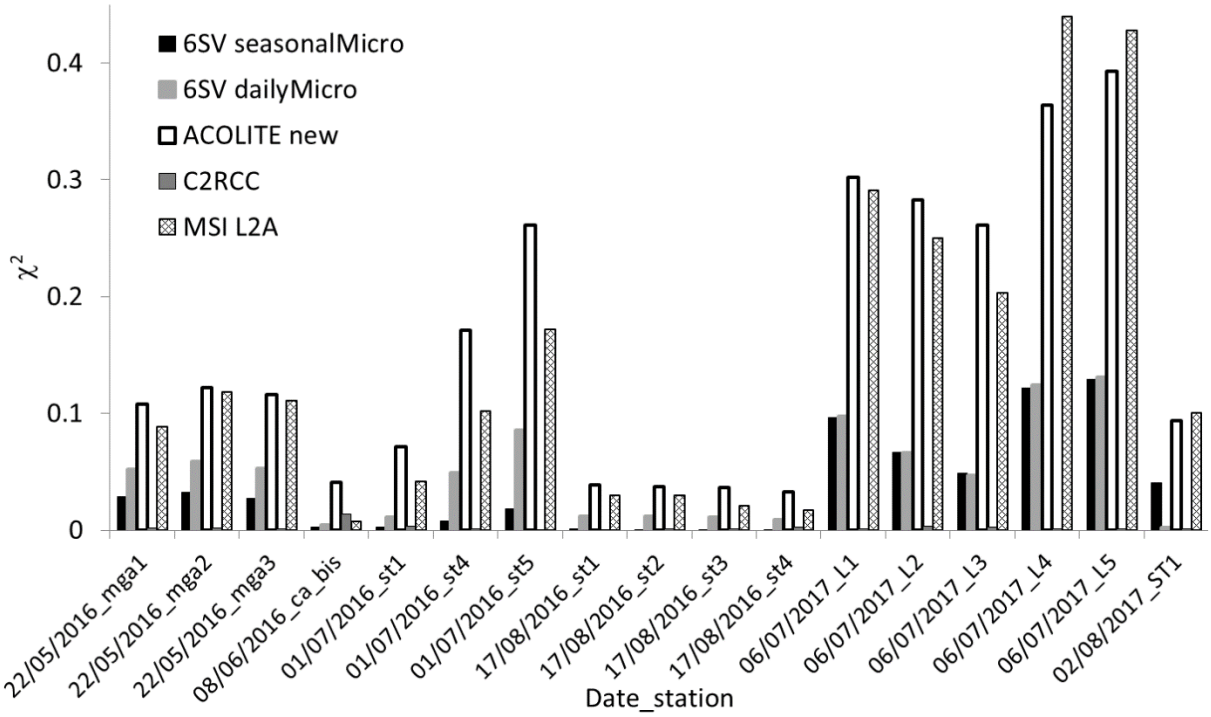

Figure 29 χ^2 calculated for the best performing algorithms (only stations with valid values for all) from S2A/B-MSI imagery, and in situ measured in subalpine lakes.

For **S3A-OLCI** imagery (Figure 30), the best results in terms of shape were obtained from POLYMER and 6SV, this last only for bands between 412.5 and 740 nm (the first band was in fact overestimated, by both 6SV and L2 standard products), despite the fact the lowest RMSE was again obtained by C2RCC by almost all bands, and by POLYMER. The lowest χ^2 values were retrieved for POLYMER, OLCI-L2, C2RCC products (Figure 32). As stated in Sec. 4.8, standard products were constantly flagged out by suggested flags; values were often negative in the blue and NIR regions of the spectrum. C2RCC tended to overestimate the green-blue slope, moving again the peak toward blue region. *6SV seasonalMicro* performed well as far as retrieved AOT from MODIS product was accurate. Negative values were produced when MODIS products error was larger, in particular with larger aerosol load conditions, as expected, as on 1st July 2016 (the lower spectra in Figure 30, *6SV seasonalMicro* plot), when AOD from AERONET was 0.39 and from MODIS derived product was 0.49.

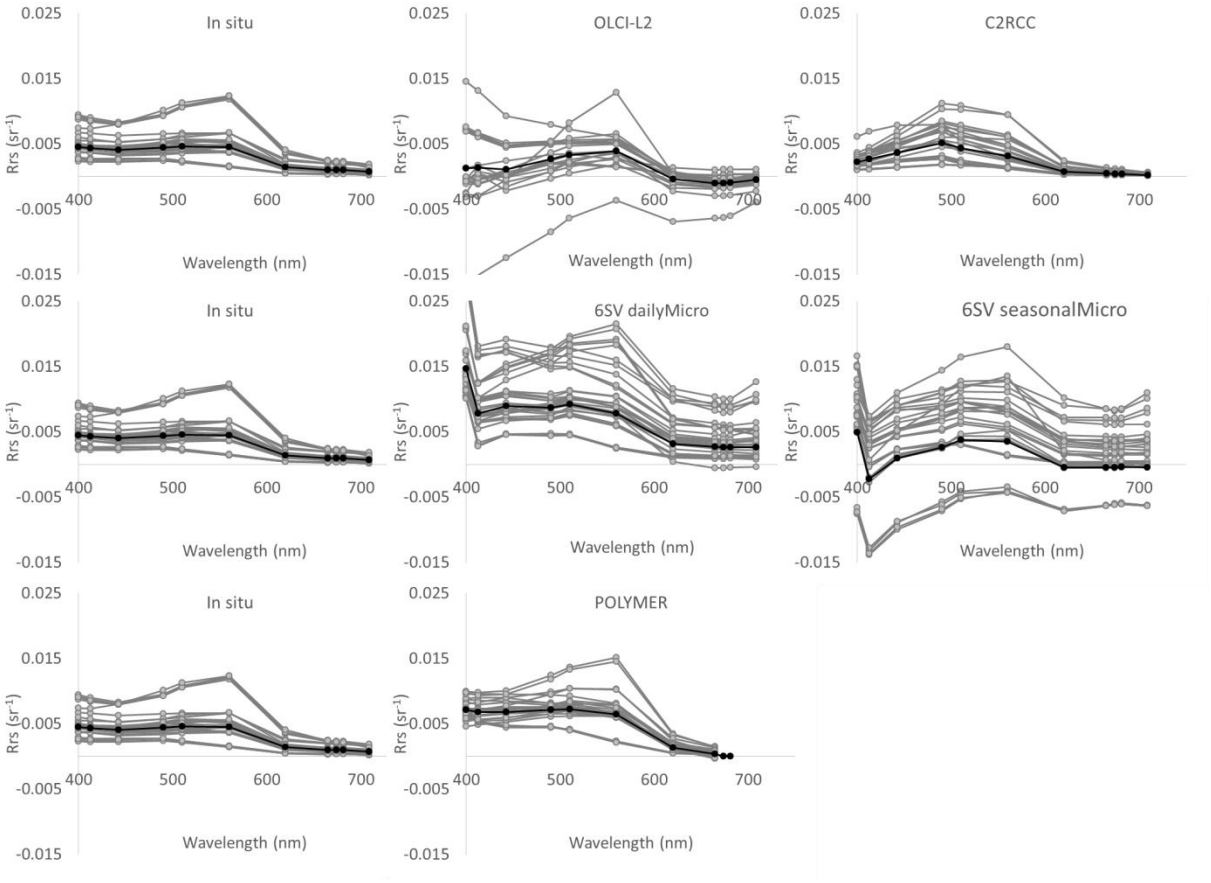

Figure 30 Rrs obtained through all atmospheric correction processors in subalpine lakes for all available match-ups, extracted from 3 by 3 ROIs over in situ measurements stations from S3A-OLCI imagery and in situ measured. In situ plot is repeated to help visualization. Black line shows mean value for each processor (of in situ measurements in case of in situ plot).

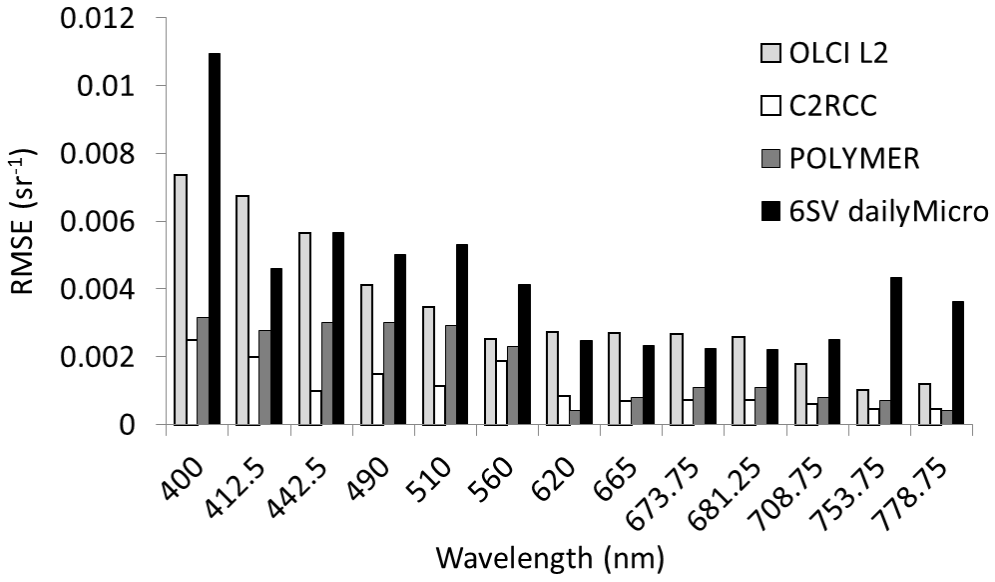

Figure 31 RMSE calculated for the best performing algorithms (only stations with valid values for all) from S3A-OLCI imagery, and in situ measured in subalpine lakes

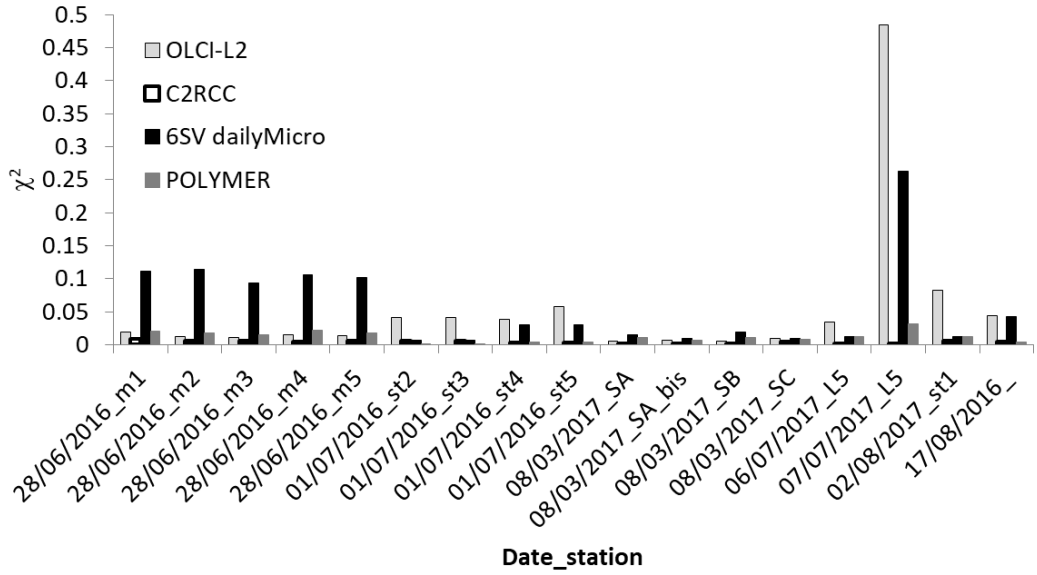

Figure 32 χ^2 calculated for the best performing algorithms (only stations with valid values for all) from S3A-OLCI imagery, and in situ measured in subalpine lakes.

For **L8-OLI** derived product, best performance in terms of χ^2 and RMSE (Figure 33 and Figure 34) were obtained through C2RCC and secondly, *6SV dailyMicro*, but C2RCC failed (masked out) retrieving Rrs on much more dates, including when *in situ* water samples for chl-a measurement were collected, thus preventing from being further analysed in terms of final product accuracy. For *ACOLITE new*, ATCOR *varying* and 6SV *seasonalMicro* χ^2 results were omitted to help visualization, since the range was respectively 0.06-0.32 sr^{-1}; 0.05-0.25 sr^{-1}; 0.004-0.1 sr^{-1}. ATCOR and ACOLITE (both versions) highly overestimated Rrs spectra, mainly in the blue region (Figure 35).

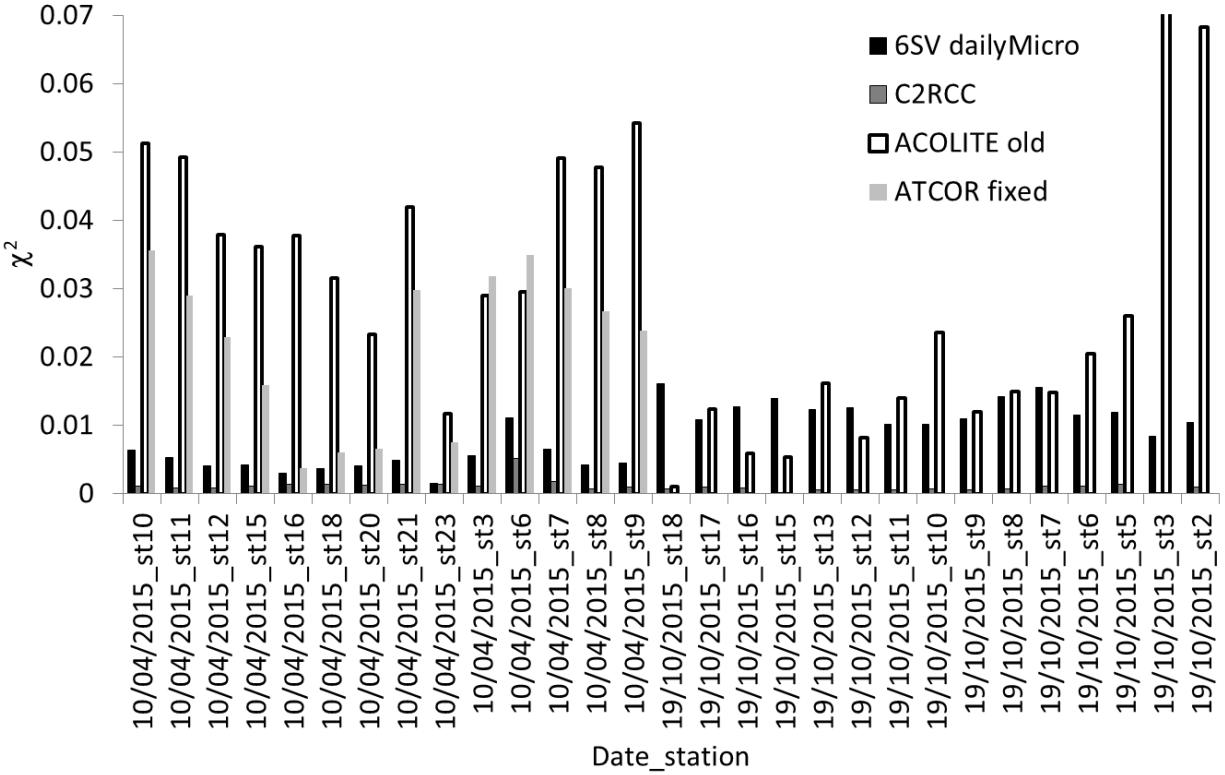

Figure 33 χ^2 calculated for the best performing algorithms from L8-OLI imagery, and in situ measured in subalpine lakes. Values for the other processors were omitted to help visualization. ATCOR fixed masked out all pixels on 19/10/2015 over all stations.

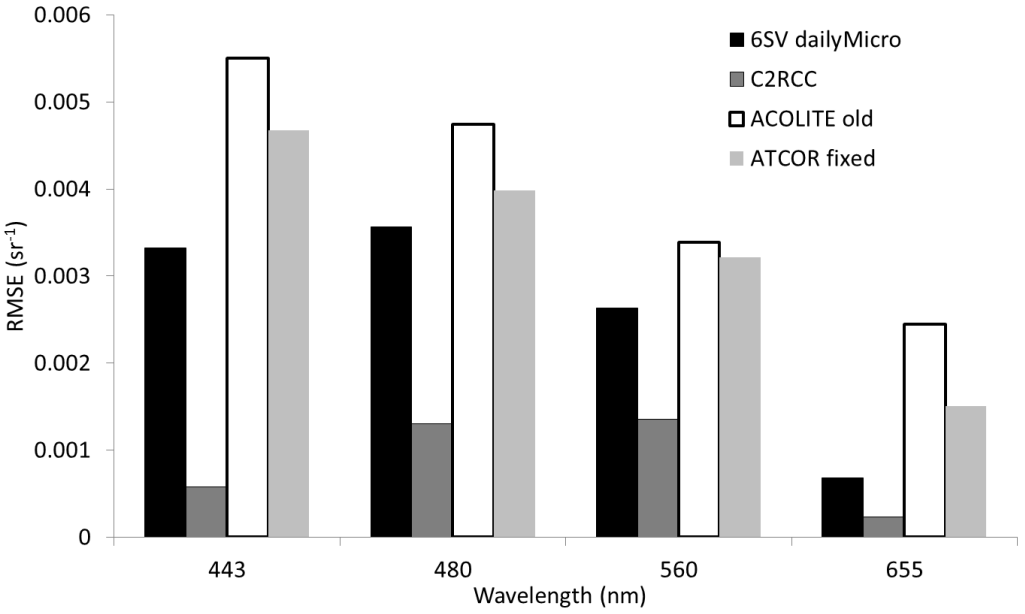

Figure 34 RMSE estimated for the best performing algorithms from L8-OLI imagery, and in situ measured in subalpine lakes.

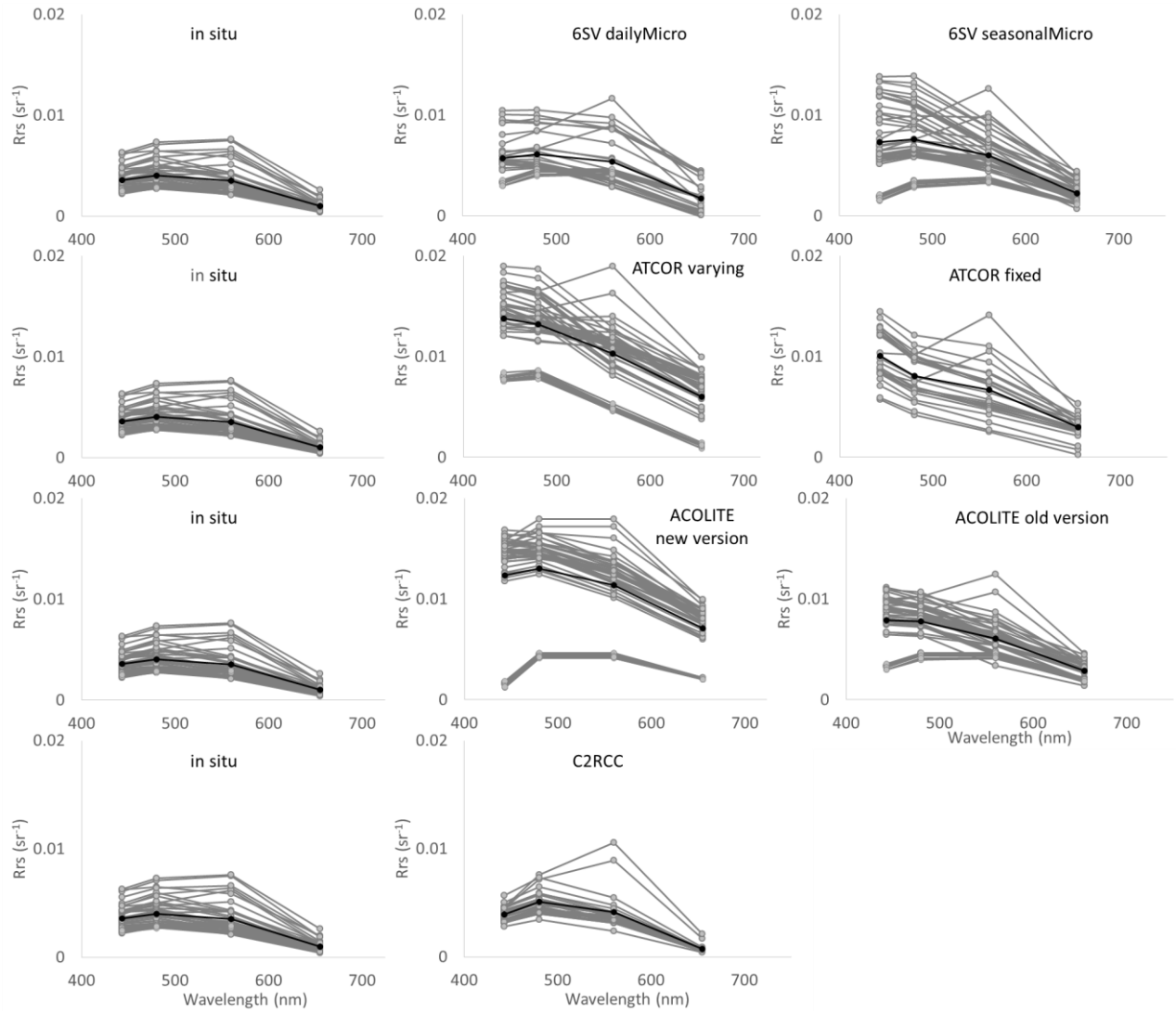

Figure 35 Rrs obtained through all atmospheric correction processors in subalpine lakes for all available match-ups, extracted from 3 by 3 ROIs over in situ measurements stations from L8-OLI imagery and in situ measured. In situ plot is repeated to help visualization. Black line shows mean value for each processor (of in situ measurements in case of in situ plot).

Lake Iseo, the most eutrophic among the subalpine lakes here included, was analysed separately, as characterised by a different type of waters. On the other hand, only few match-ups were available after cloud screening, with one date for each sensor: more match-ups are thus required for a robust analysis. On the other hand, looking at first results for **S2A-MSI,** as clearly shown in Figure 36 and by RMSE in Figure 37, *6SV dailyMicro* (mean $\chi^2 = 0.0037$ sr^{-1}, Figure 38) outperformed all the other processors.

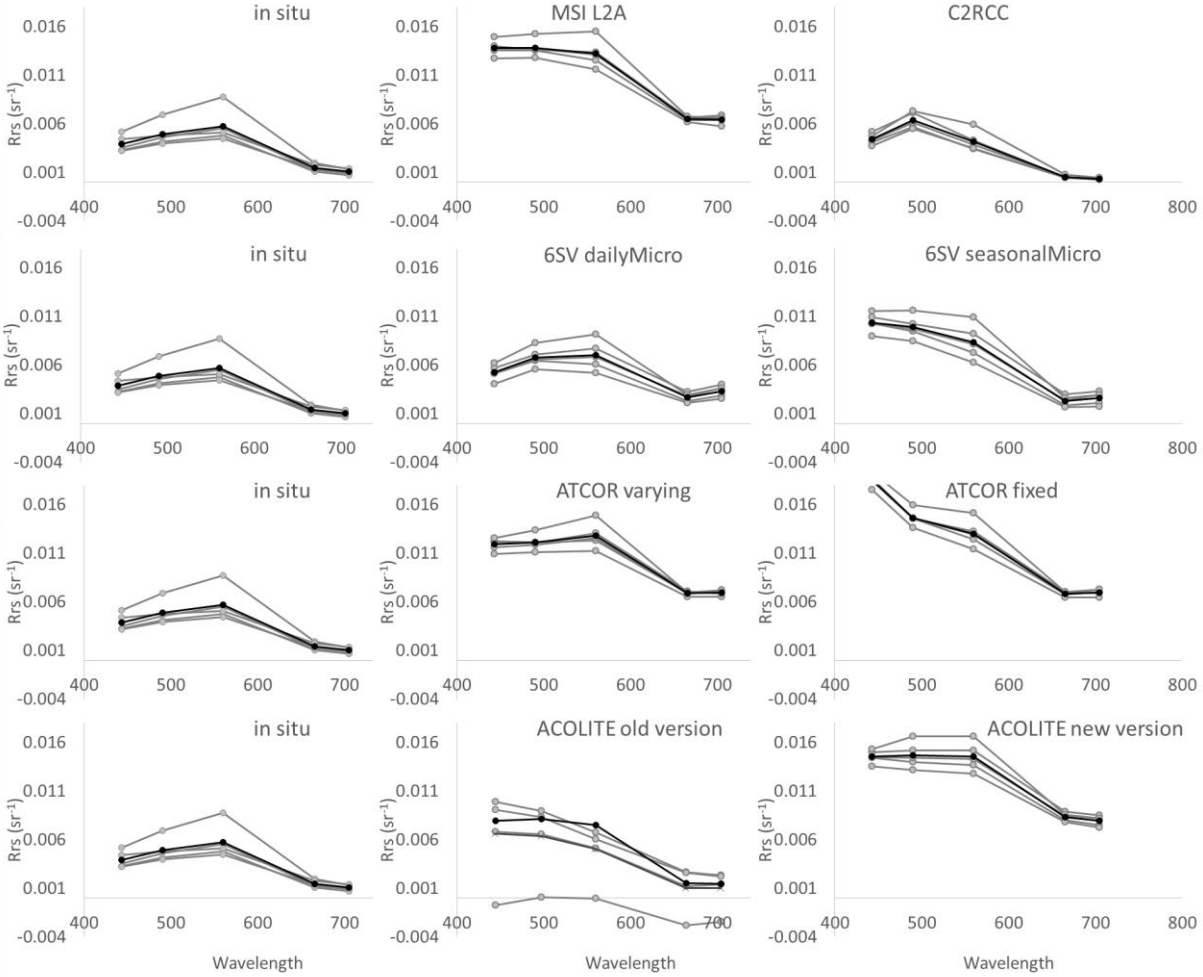

Figure 36 Rrs obtained through all atmospheric correction processors in Lake Iseo for all available match-ups, extracted from 3 by 3 ROIs over in situ measurements stations from S2-MSI imagery and in situ measured. In situ plot is repeated to help visualization. Black line shows mean value for each processor (of in situ measurements in case of in situ plot).

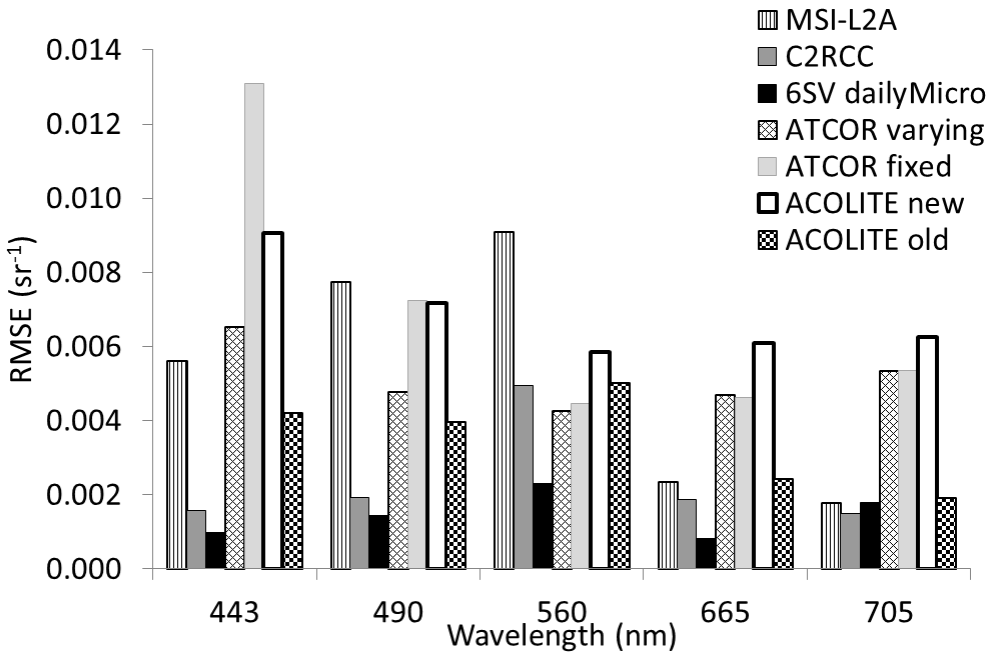

Figure 37 RMSE calculated for atmospheric correction algorithms from S2A-MSI imagery, and in situ measured in Lake Iseo.

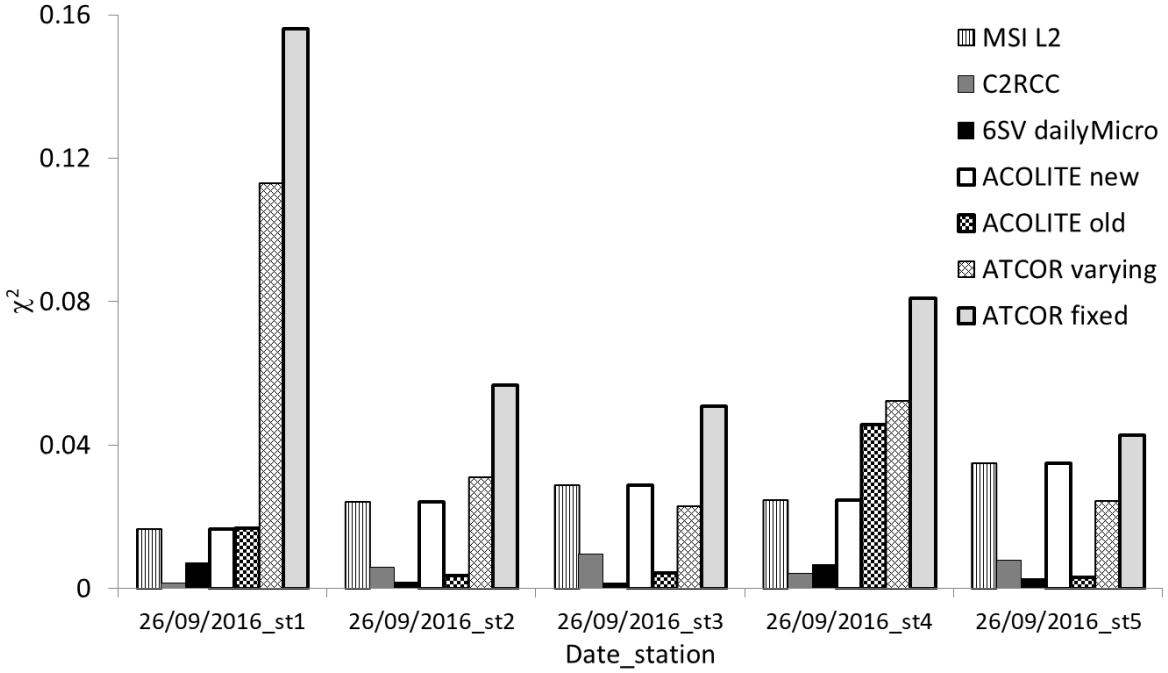

Figure 38 χ^2 calculated for atmospheric correction algorithms from S2A-MSI imagery, and in situ measured in Lake Iseo.

For **L8-OLI** the best estimate was obtained through *ATCOR fixed*, *ACOLITE old* and *6SV dailyMicro* (Figure 39 and Figure 40), for which χ^2 values are shown in Figure 41 (it was omitted for the other algorithms, for which values were much higher, to help visualization). *ATCOR fixed* on the other hand, inverted the slope between the first two bands in most of the match-ups, causing BOMBER (see Sec. 5.2.2) failing retrieving chl-a values from ATCOR *fixed* Rrs.

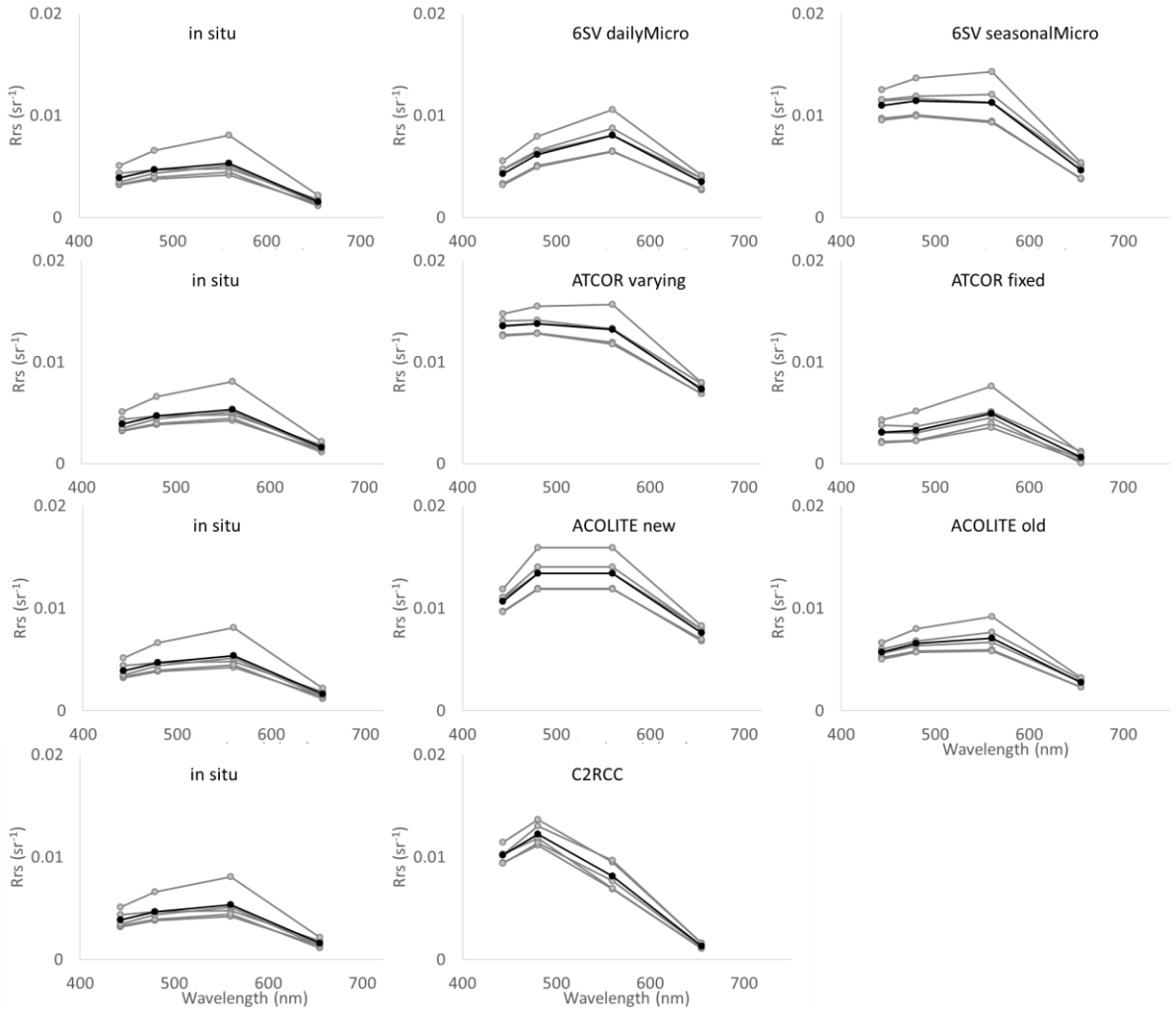

Figure 39 Rrs obtained through all atmospheric correction processors in Lake Iseo for all available match-ups, extracted from 3 by 3 ROIs over in situ measurements stations from L8-OLI imagery and in situ measured. In situ plot is repeated to help visualization. Black line shows mean value for each processor (of in situ measurements in case of in situ plot).

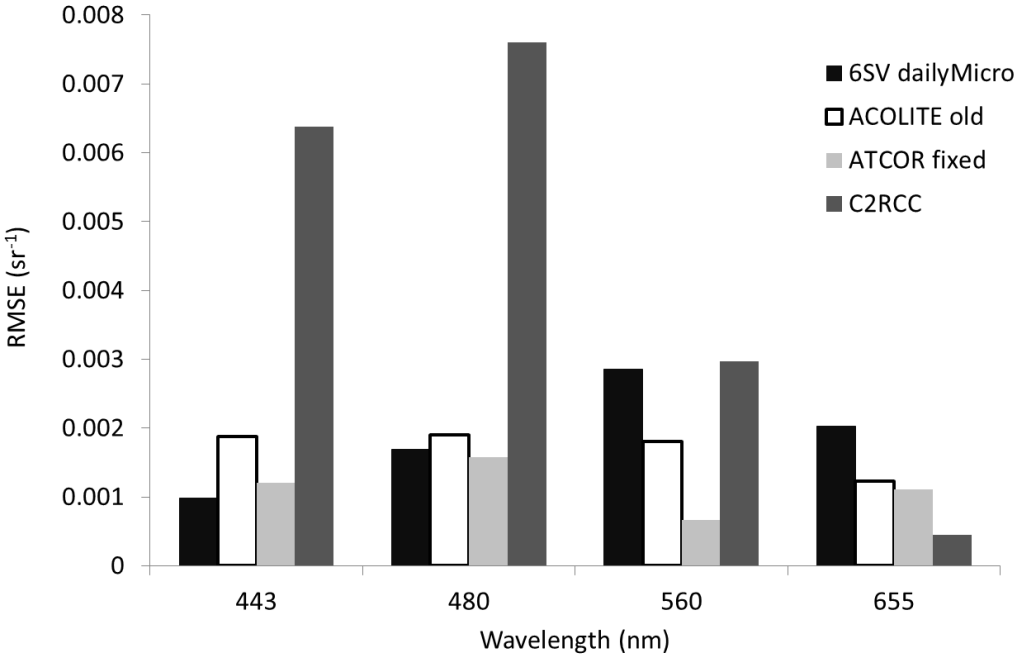

Figure 40 RMSE estimated for the best performing algorithms (only stations with valid values for all) from L8-OLI imagery, and in situ measured in Lake Iseo.

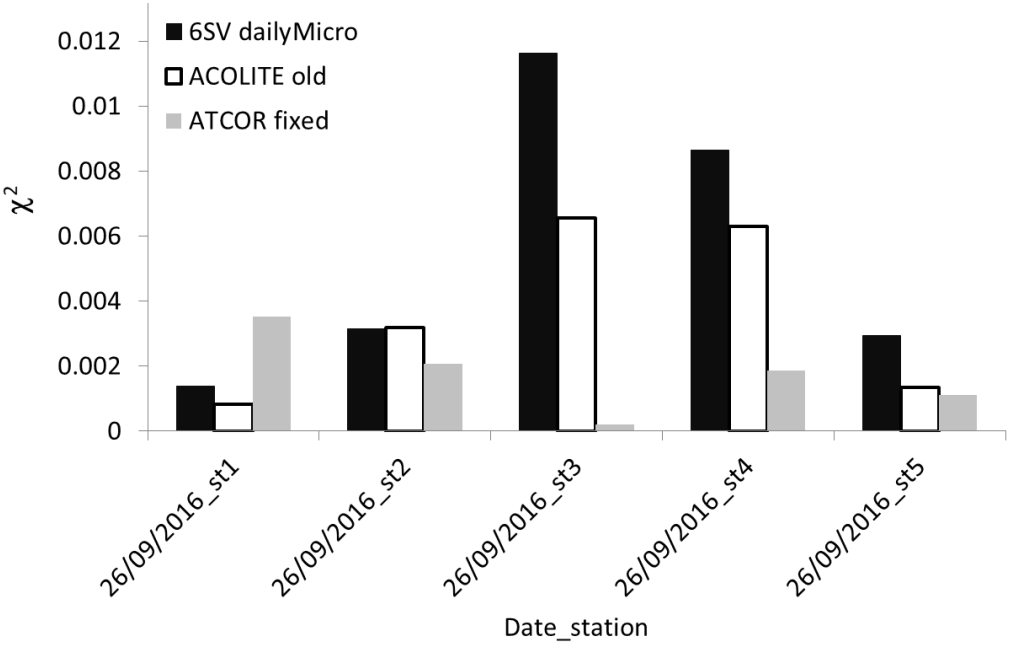

Figure 41 χ^2 calculated for the best performing algorithms (only stations with valid values for all) from L8-OLI imagery, and in situ measured in Lake Iseo.

Finally for **S3A-OLCI**, only one match-up was available after cloud screening, for which results are shown in Figure 42 for all processors: POLYMER is clearly the best performing at shorter bands, while *6SV seasonalMicro* is perfectly matching the *in situ* spectrum at longer wavelengths.

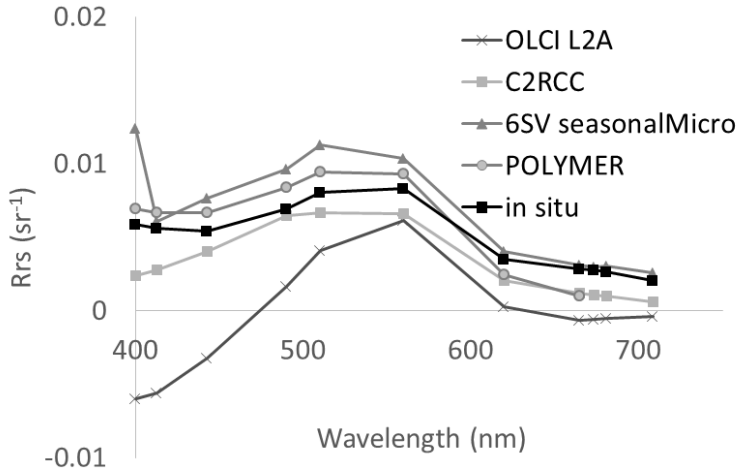

Figure 42 Rrs obtained through different atmospheric correction algorithms, extracted from 3 by 3 ROIs over in situ measurement station in Lake Iseo on 26th July 2017, from S3-OLCI imagery, and in situ measured.

5.1.3 Mantua lakes

Products in Mantua lakes, after cloud screening, were evaluated on two dates for S2A-MSI and one date for L8-OLI, when no simultaneous AERONET inversion products were available in Sirmione AERONET site. Thus only *6SV seasonalMicro* Rrs maps were produced and evaluated. Although this, the 6SV-based algorithm was able, together with ATCOR, which performed at best in both configuration, to capture the typical absorbing peak due to the high chl-a concentration that was measured in four of the *in situ* measurement points (Figure 43). Finally, ACOLITE new was able to capture this same feature, despite the fact it failed retrieving a reasonable shape for the overall Rrs spectrum. For the two bands used for chl-a maps retrieval, bands 5 (705 nm) and 4 (665 nm), the best RMSE was obtained through ACOLITE new and *6SV seasonalMicro* (Figure 44), whose results in longer wavelength were on the other hand among the worst, as shown also by χ^2 in Figure 45. The other processors did not catch this feature or underestimated the ratio between the two bands.

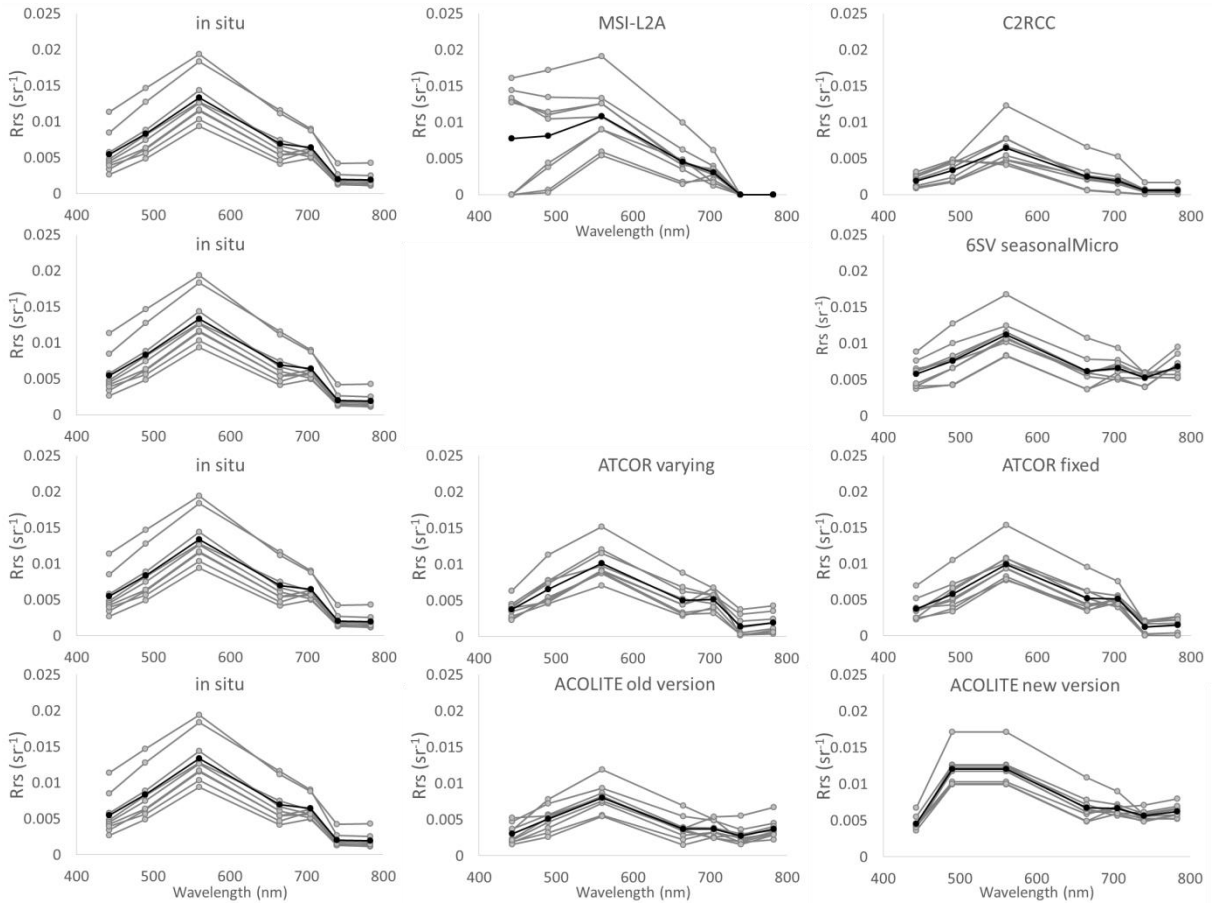

Figure 43 Rrs obtained through all atmospheric correction processors in Mantua lakes for all available match-ups, extracted from 3 by 3 ROIs over in situ measurements stations from S2A-MSI imagery and in situ measured. In situ plot is repeated to help visualization. Black line shows mean value for each processor (of in situ measurements in case of in situ plot).

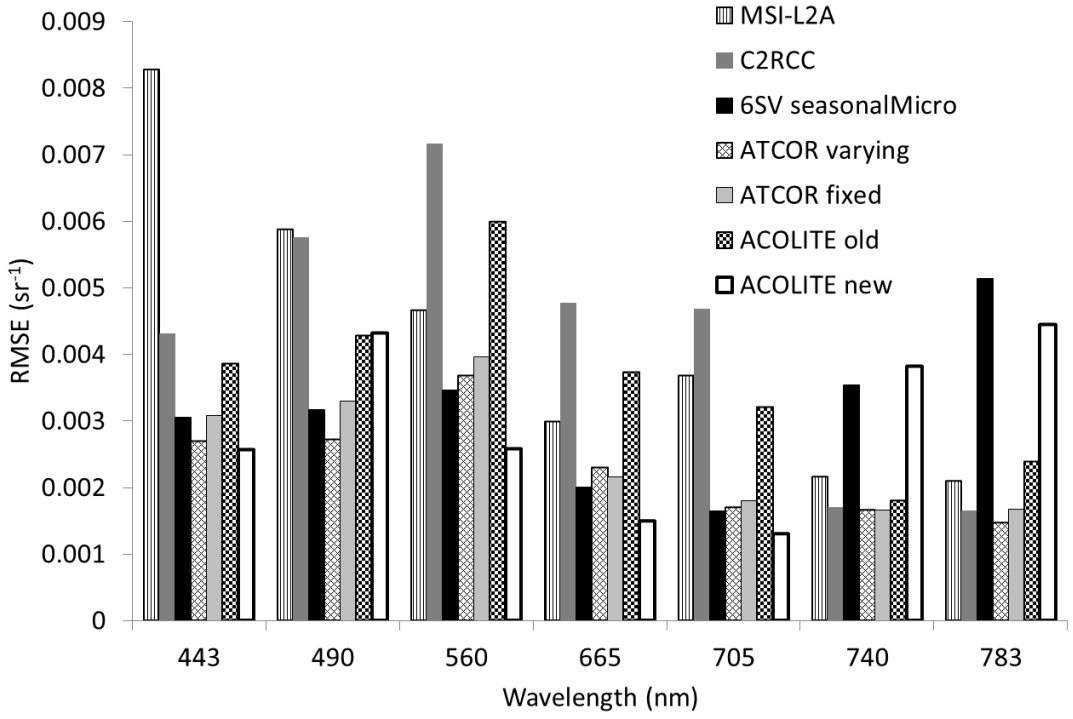

Figure 44 RMSE estimated for the best performing algorithms from S2-MSI imagery and in situ measured in Mantua lakes.

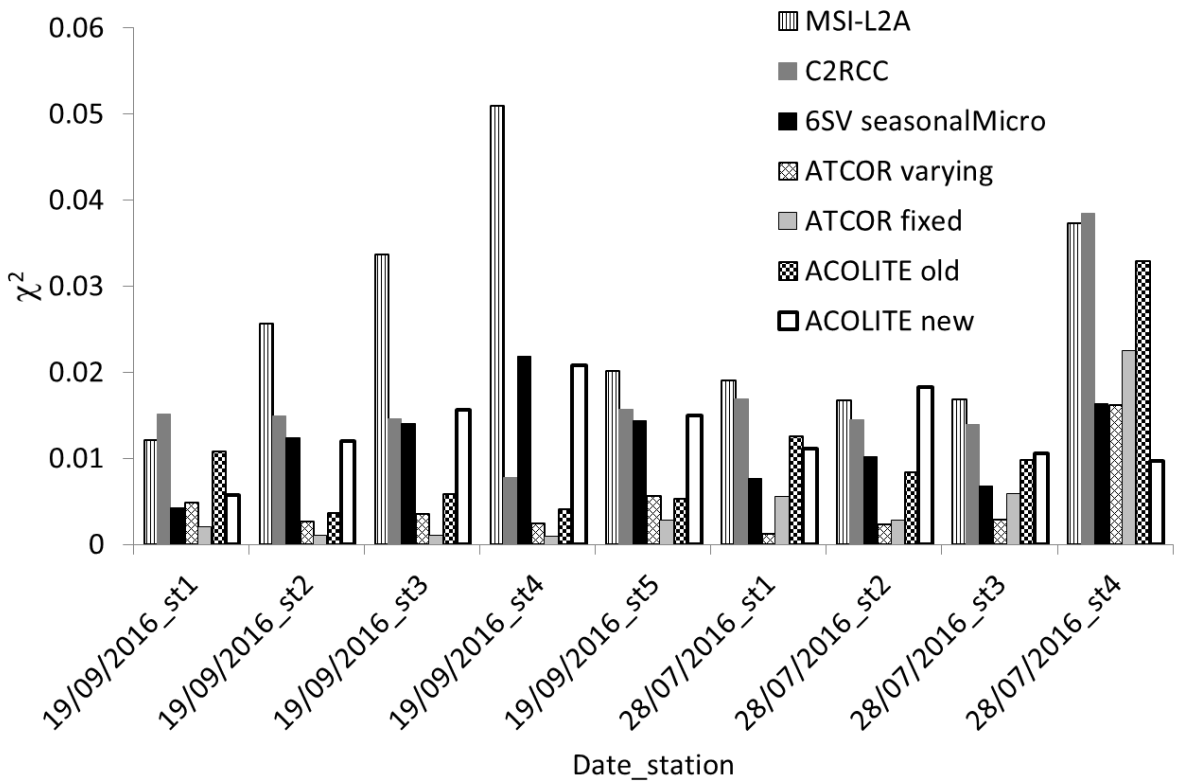

Figure 45 χ^2 calculated for the best performing algorithms from S2-MSI imagery and in situ measured in Mantua lakes.

L8-OLI match-ups (Figure 46) showed good performances for *6SV seasonalMicro*, *ATCOR varying*, and *ACOLITE old*, this last obtaining the best results in terms of χ^2 (Figure 47), and RMSE mainly for shorter wavelengths (Figure 48). C2RCC failed over all the match-ups.

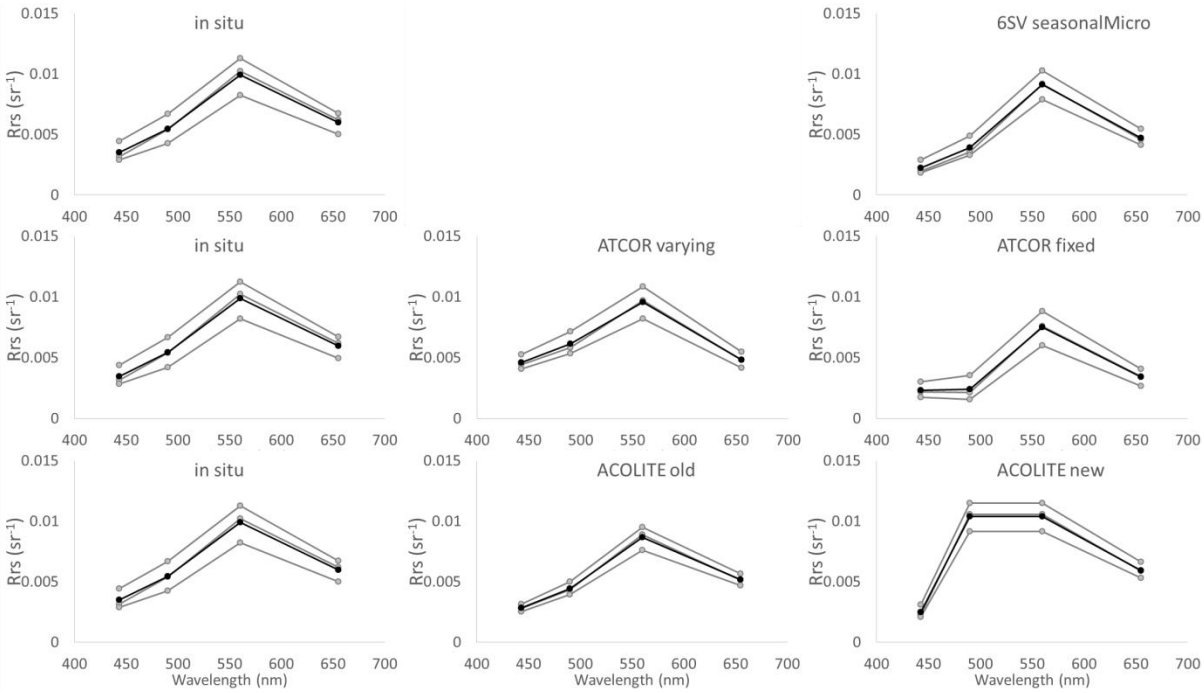

Figure 46 Rrs obtained through all atmospheric correction processors in Mantua lakes for all available match-ups, extracted from 3 by 3 ROIs over in situ measurements stations from L8-OLCI imagery and in situ measured. In situ plot is repeated to help visualization. Black line shows mean value for each processor (of in situ measurements in case of in situ plot).

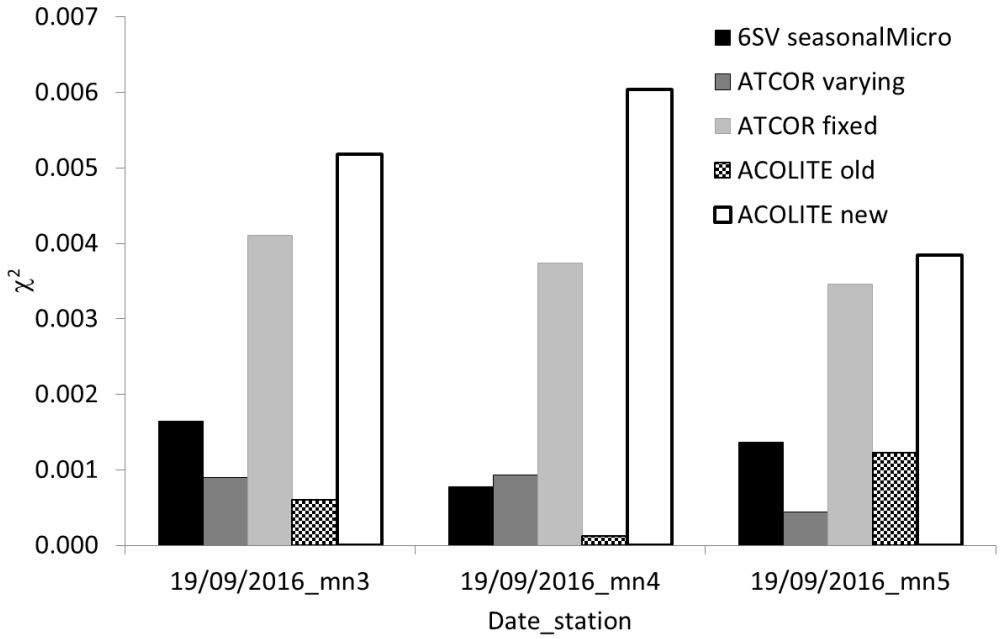

Figure 47 χ^2 calculated from L8-OLI imagery and in situ measured in Mantua lakes.

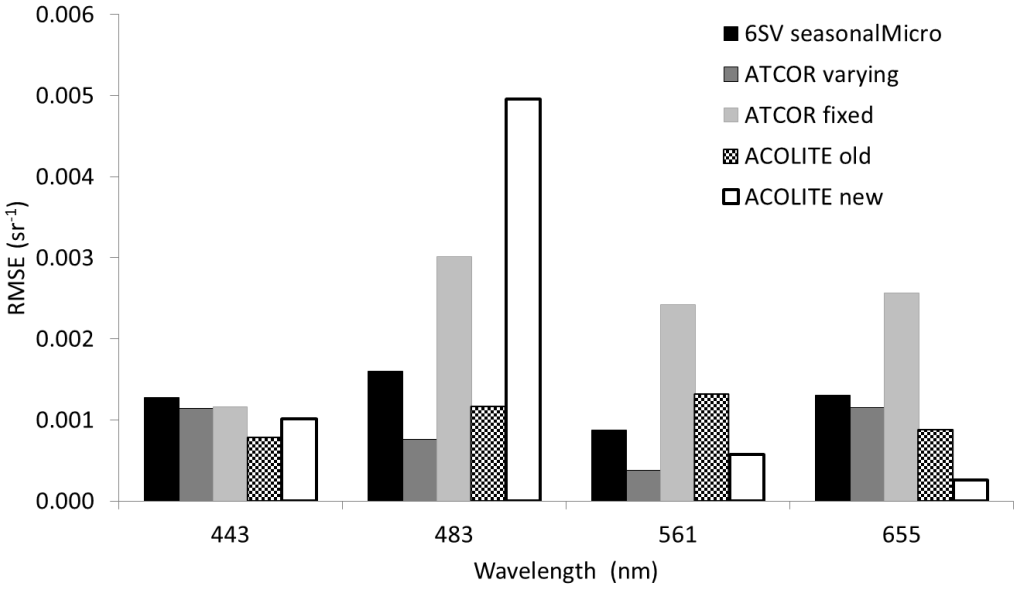

Figure 48 RMSE estimated from L8-OLI imagery and in situ measured in Mantua lakes.

5.1.4 Curonian Lagoon

For S2A, after clouds screening, 3 match-ups were available and used to evaluate atmospherically corrected products over the hyper-eutrophic Curonian Lagoon. As Figure 49 and χ^2 in Figure 50 show, best results were obtained by ATCOR (*fixed* mode only, since not enough DDV objects were found in the image and thus the processing failed in *varying* mode) and *ACOLITE old*. Standard distributed products and *6SV predefined* failed in retrieving good results for the first band and overestimated the ratio between 705 nm and 665 nm, used for chl-a concentration estimation by the empirical algorithm. On the contrary, C2RCC and *ACOLITE new*, failed recognizing this important feature.

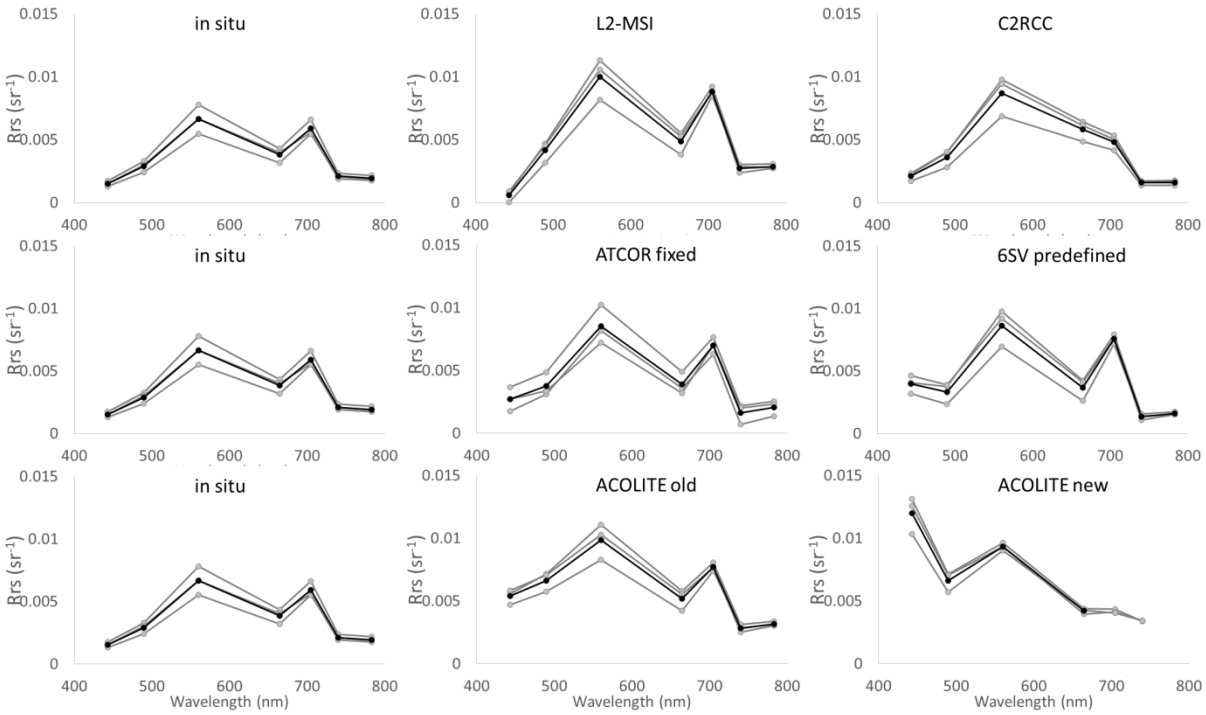

Figure 49 Rrs obtained through all atmospheric correction processors in Curonian Lagoon for all available match-ups, extracted from 3 by 3 ROIs over in situ measurements stations from S2-MSI imagery and in situ measured. In situ plot is repeated to help visualization. Black line shows mean value for each processor (of in situ measurements in case of in situ plot).

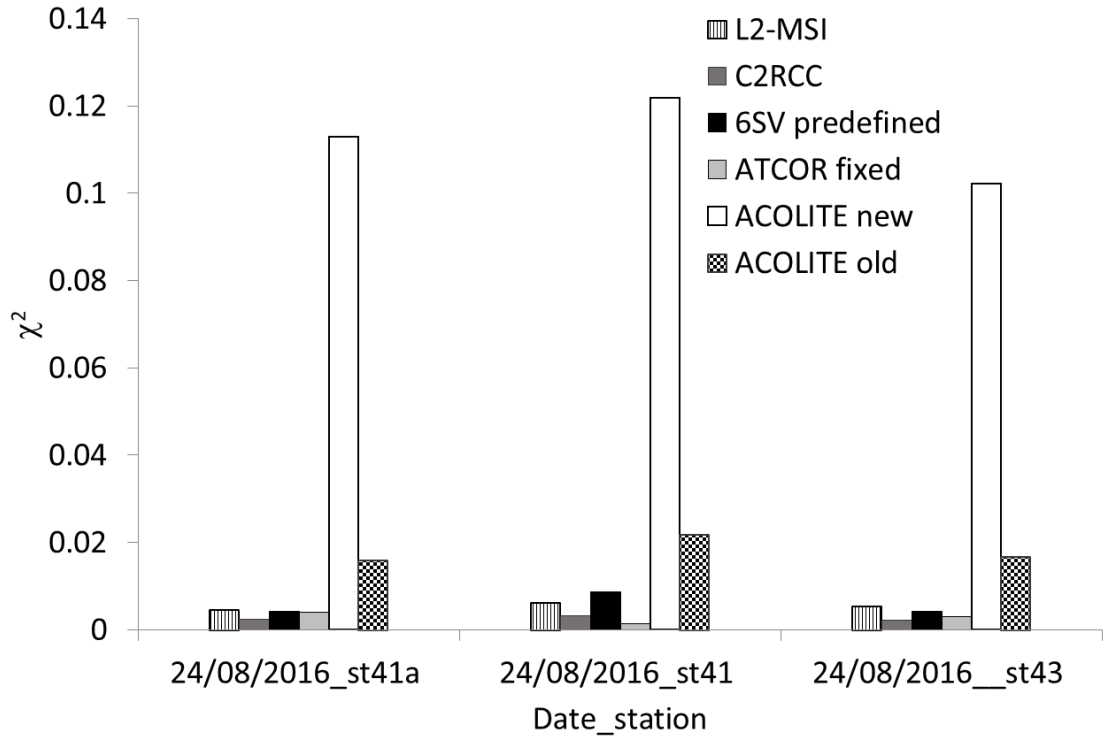

Figure 50 χ^2 calculated for all algorithms not failing from S2A-MSI imagery in Curonian Lagoon, respect to in situ measurements.

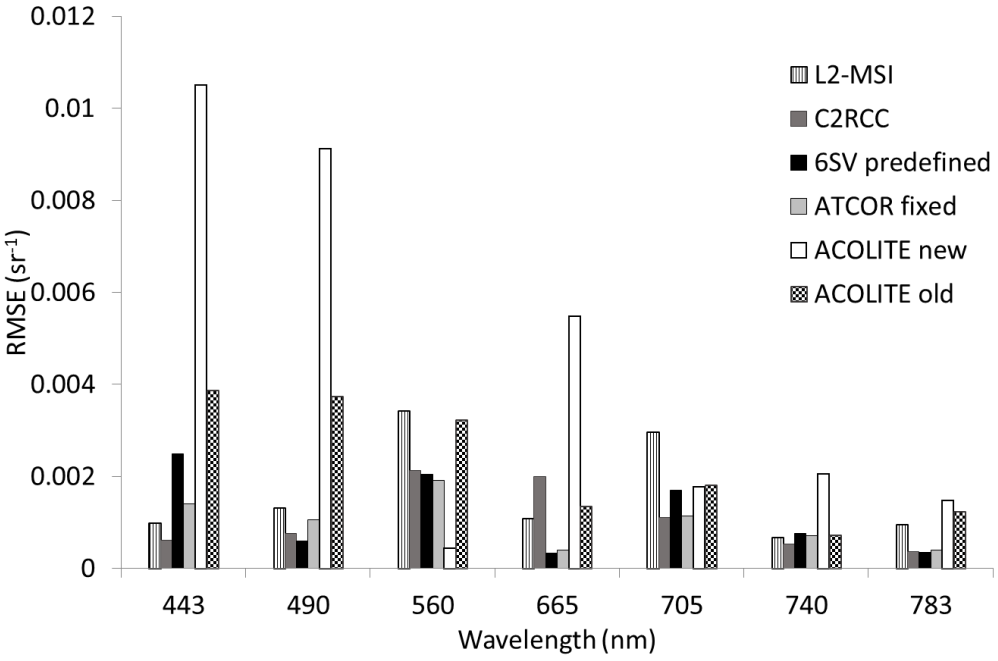

Figure 51 RMSE estimated for all algorithms not failing from S2A-MSI imagery in Curonian Lagoon, respect to in situ measurements.

Similar considerations could be done for S3A-OLCI results (Figure 52), where OLCI standard products (OLCI-L2) underestimate values for first bands (negative in some cases) and together with *6SV predefined* overestimated the 708 nm over 665 nm ratio. In this case, C2RCC was able to capture the feature at 665-708 nm spectral region, but it greatly underestimated this two bands ratio. On average, the best results were obtained by POLYMER (Figure 53, Figure 54).

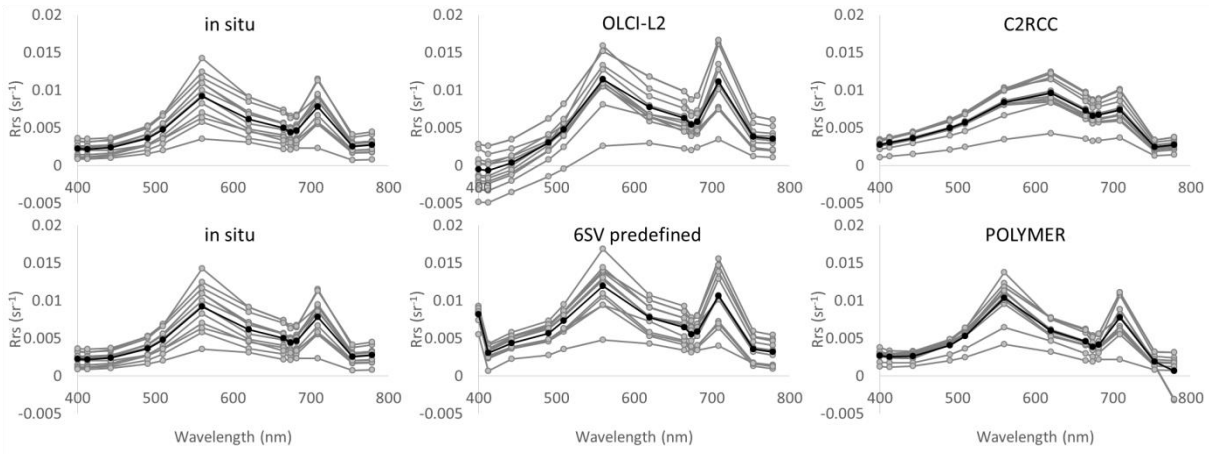

Figure 52 Rrs obtained through all atmospheric correction processors in Curonian Lagoon for all available match-ups, extracted from 3 by 3 ROIs over in situ measurements stations from S3-OLCI imagery and in situ measured. In situ plot is repeated to help visualization. Black line shows mean value for each processor (of in situ measurements in case of in situ plot).

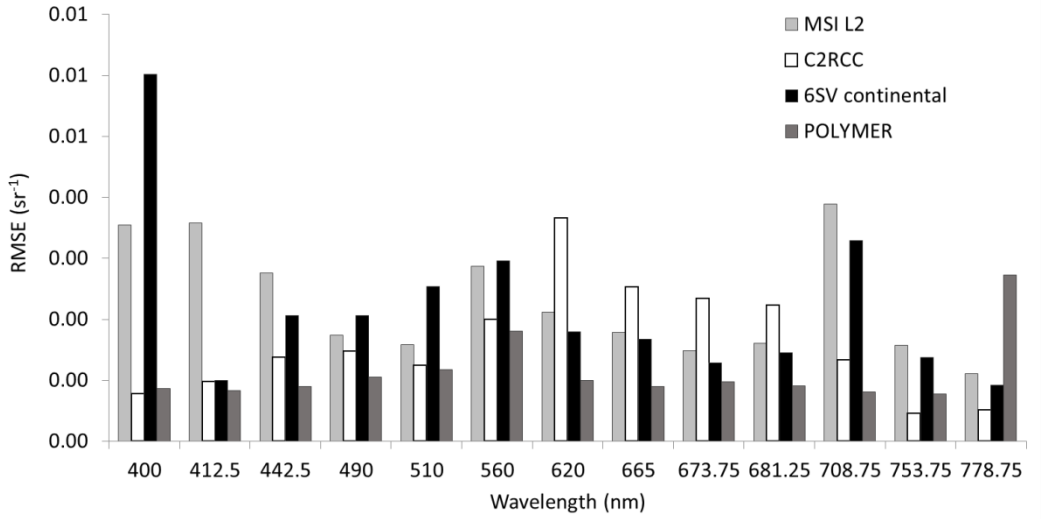

Figure 53 RMSE estimated for all algorithms not failing from S3A-OLCI imagery on Curonian Lagoon, respect to in situ measurements.

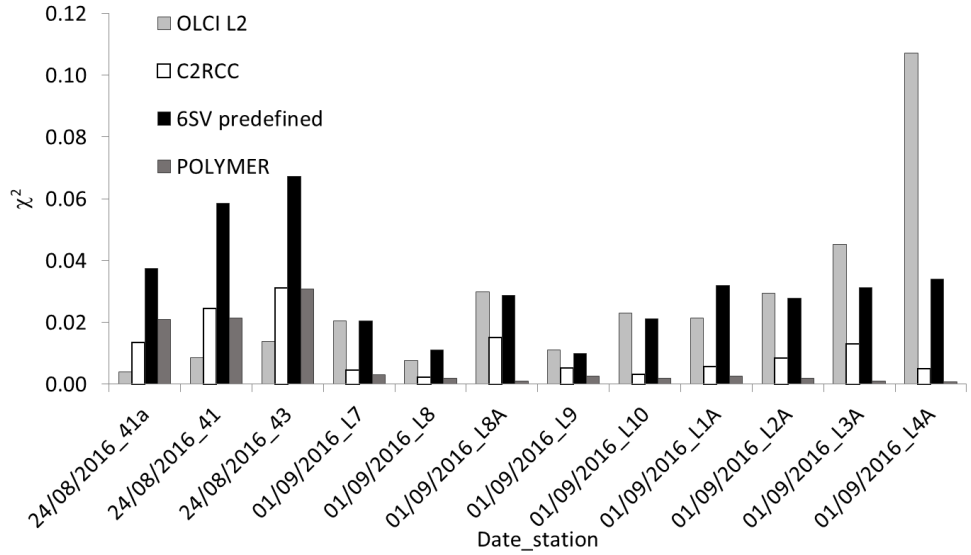

Figure 54 χ^2 calculated for all algorithms not failing from S3A-OLCI imagery on Curonian Lagoon, respect to in situ measurements.

5.2 Chl-a maps validation

5.2.1 Lake Trasimeno

For **S2A/B-MSI** imagery (Figure 55), the two best performing atmospheric correction products, generated by ATCOR (with varying visibility, ATCOR *varying*) and *6SV predefined,* were used to generate through BOMBER chl-a maps, and compared to *in situ* measurements. In addition, chl-a products directly generated by the algorithm embedded in the latest ACOLITE version, *chl_re_gons740*, which uses the red edge algorithm by Gons et al. (2002), were evaluated. The default product already included in previous versions (*ACOLITE old*) used 780 nm (band 6) as a reference, but the *chl_re_gons740* product uses 740 nm (band 5) on MSI, as specified in *ACOLITE Python User Manual* (QV - June 11, 2018). Unfortunately, matching *in situ* measurements were available only for low chl-a concentrations (lower than 5 mg m^{-3}).

Estimated MAE showed similar results for these processors, with ATCOR *varying* performing better with the lowest concentrations.

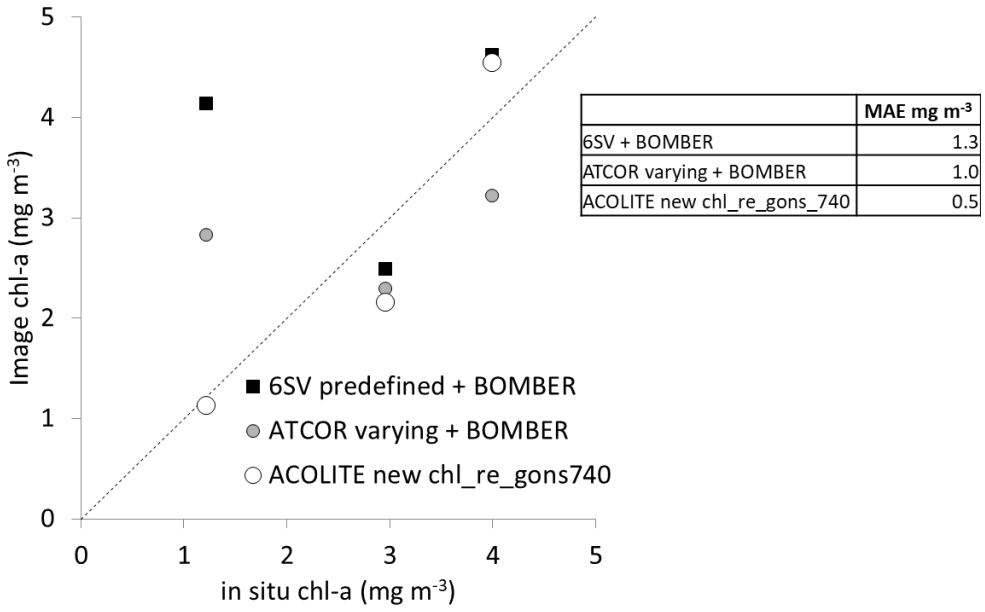

Figure 55 Scatter plot and estimated MAE for chl-a as measured in situ (x-axis) and S2-MSI derived (y-axis) through different algorithms in Lake Trasimeno.

Chl_re_gons740 products showed very good performance, but standard deviation over the 3 by 3 windows used to extract chl-a concentration was very high (up to 3.24 mg m^{-3}, 70% of the mean value). More investigation are thus required both to evaluate this algorithm efficiency, and all the processors at higher chl-a concentration.

For **S3-OLCI** derived products (Figure 56), L2 standard products were completely flagged out, and C2RCC chl-a maps were flagged out in most stations. In addition to the previous case, also two match-ups with higher concentration of chl-a were available. Also chl-a maps directly generated by POLYMER *(POLYMER CHL* in plots) were evaluated: in the maps, chl-a concentration is highly underestimated at higher concentrations and overestimated at lower values. On the other hand, BOMBER maps derived from *6SV predefined* and POLYMER Rrs produced very good results (see MAE in Figure 56).

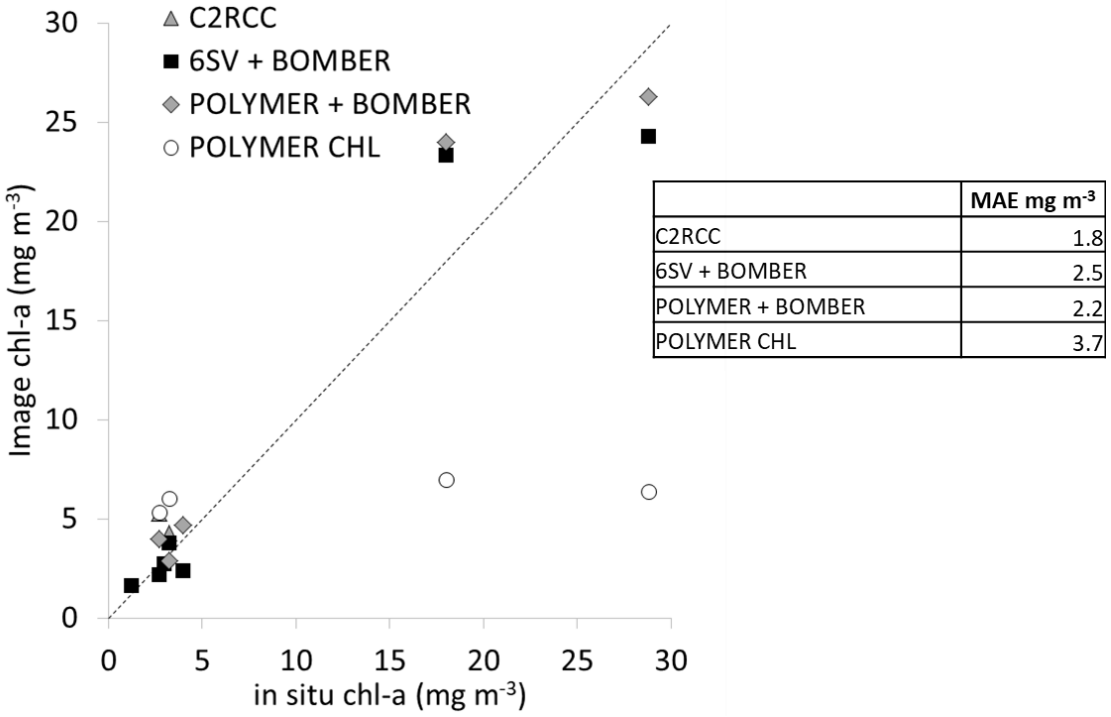

	MAE mg m^{-3}
C2RCC	1.8
6SV + BOMBER	2.5
POLYMER + BOMBER	2.2
POLYMER CHL	3.7

Figure 56 Scatter plot and estimated MAE for chl-a as measured in situ (x-axis) and S3-OLCI derived (y-axis) through different algorithms in Lake Trasimeno. For C2RCC only 2 match-ups were available.

5.2.2 Subalpine lakes

In Subalpine lakes, for **S2-MSI** imagery, chl-a derived products were evaluated for the best performing algorithm products, feeding BOMBER with *6SV dailyMicro* and *ACOLITE new* Rrs products. For *ACOLITE new*, also its embedded chl-a products suggested for lower concentration, *chl_oc2* and *chl_oc3*, were evaluated. For lower chl-a concentrations, *chl_oc2* performed well, in some cases even slightly better than BOMBER, but for larger concentration it tends to underestimate chl-a concentration. BOMBER products derived from *ACOLITE new* Rrs is also underestimating chl-a in the whole range of measured values, while the best estimates were retrieved feeding BOMBER with *6SV dailyMicro* Rrs. This last consideration, confirmed how BOMBER is able, in Subalpine lakes, to retrieve good chl-a estimates even when the overall

spectrum is overestimated, but with a good accordance in terms of shape to corresponding *in situ* measured spectra.

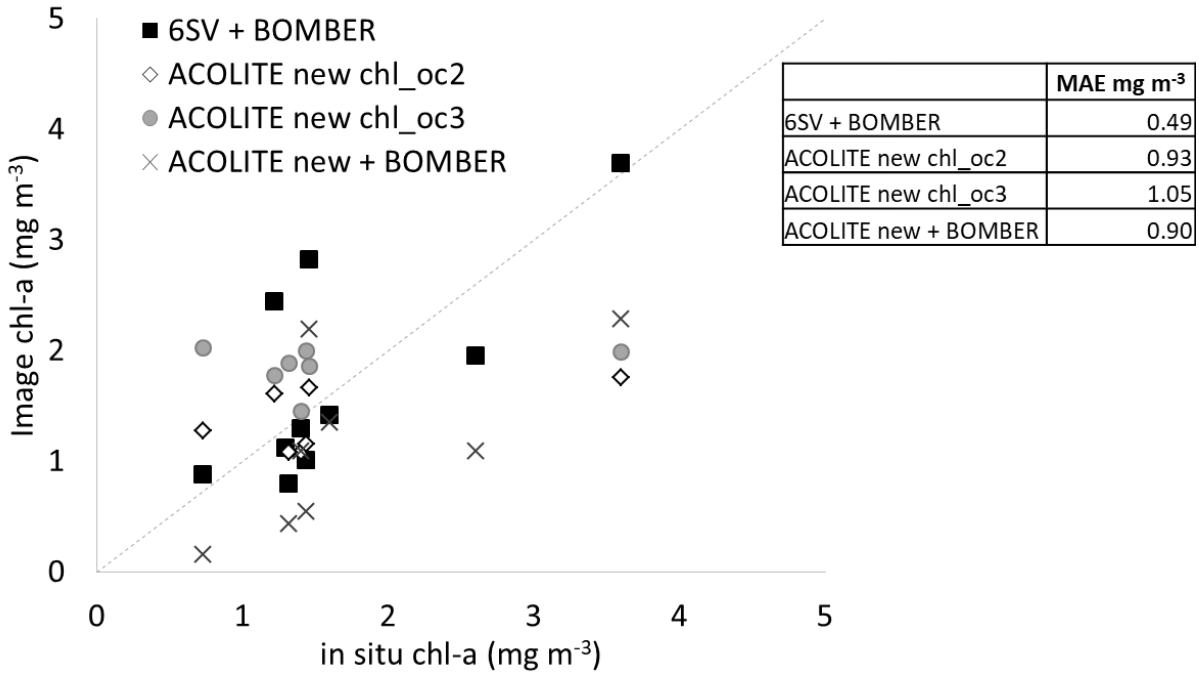

	MAE mg m^{-3}
6SV + BOMBER	0.49
ACOLITE new chl_oc2	0.93
ACOLITE new chl_oc3	1.05
ACOLITE new + BOMBER	0.90

Figure 57 Scatter plot and estimated MAE for chl-a as measured in situ (x-axis) and by S2A/B-MSI derived products (y-axis) through different algorithms in Subalpine lakes.

For **S3-OLCI** derived maps, standard and alternative (C2RCC) products were evaluated, against POLYMER chl-a concentration maps (derived directly by POLYMER*, POLYMER CHL*), and BOMBER products derived both from POLYMER (*POLYMER + BOMBER*) and *6SV dailyMicro* (*6SV + BOMBER*) Rrs. Very similar performances were obtained by *POLYMER + BOMBER*, *6SV + BOMBER,* and *POLYMER CHL* products as shown by MAE in Figure 58.

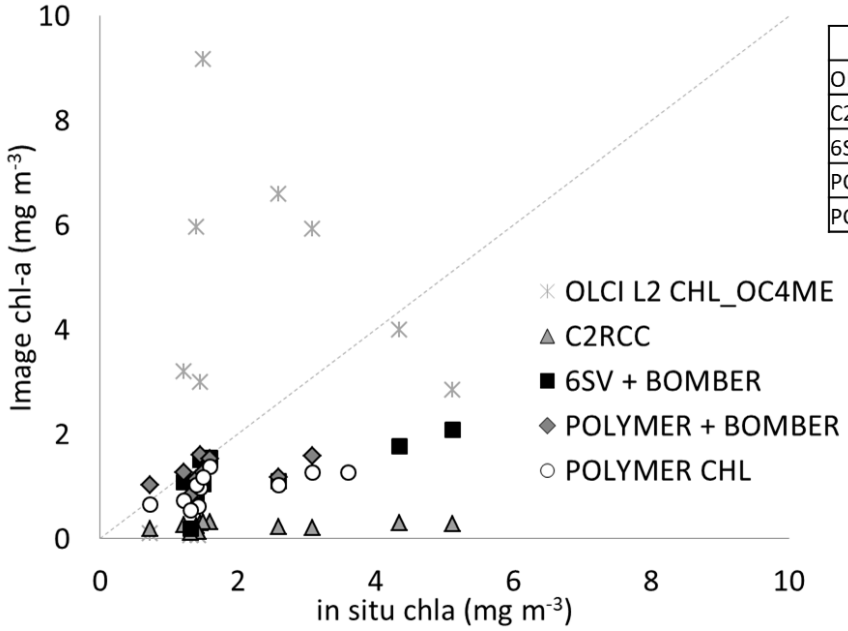

	MAE mg m^{-3}
OLCI-L2 CHL_OC4ME	3.50
C2RCC	1.33
6SV + BOMBER	0.51
POLYMER + BOMBER	0.38
POLYMER CHL	0.61

Figure 58 Scatter plot for chl-a as measured in situ (x-axis) and by S3A-OLCI derived products (y-axis) through different algorithms over Subalpine lakes.

For **L8-OLI**, on dates when *in situ* water samples were available, C2RCC mostly failed, and only 3 match-ups over Lake Maggiore were available. Despite this, it is clearly shown in Figure 59, how *6SV* + *BOMBER* products provided the best estimate (MAE = 0.41 mg m^{-3}).

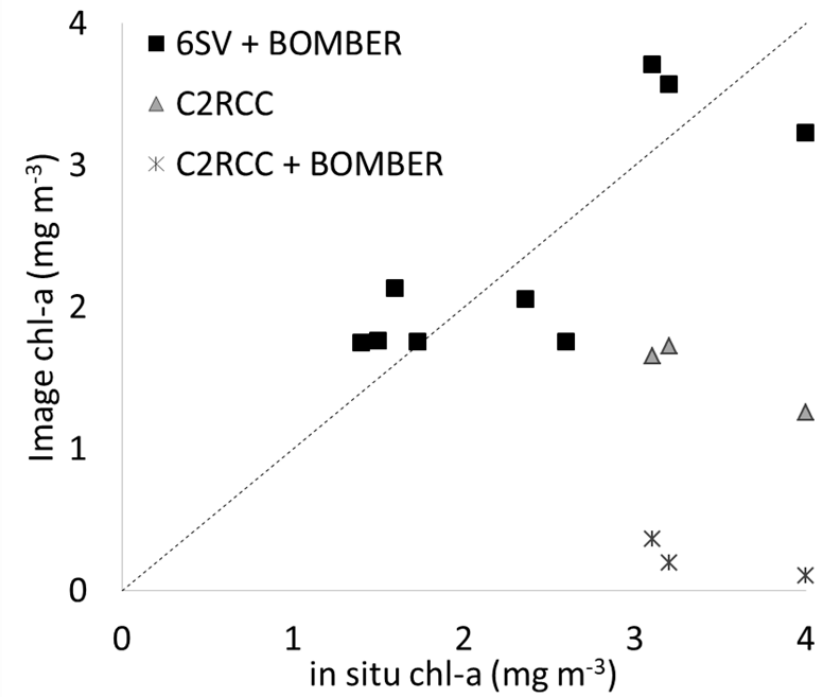

	MAE mg m^{-3}
6SV + BOMBER	0.41
C2RCC	1.89
C2RCC + BOMBER	3.21

Figure 59 Scatterplot for chl-a as measured in situ (x-axis) and L8-OLI derived (y-axis) through different algorithms over Subalpine lakes.

Over **Lake Iseo**, for **S2-MSI** imagery, BOMBER was applied only on *6SV dailyMicro* derived Rrs, since all the other processors were outperformed by it. Larger error were found for larger concentration with MAE equal to 1.17 mg m^{-3}, which indicates that further investigation and improvement are required for this sensor-lake couple. For **L8-OLI** products, in fact, results on the same date were absolutely better, as shown in Figure 60, in particular for BOMBER products, derived from 6SV *dailyMicro* Rrs (*6SV + BOMBER*) and A*COLITE new* chl_oc3 products. MAE values are shown in the table in Figure 60, indicating lower errors for latest ACOLITE products.

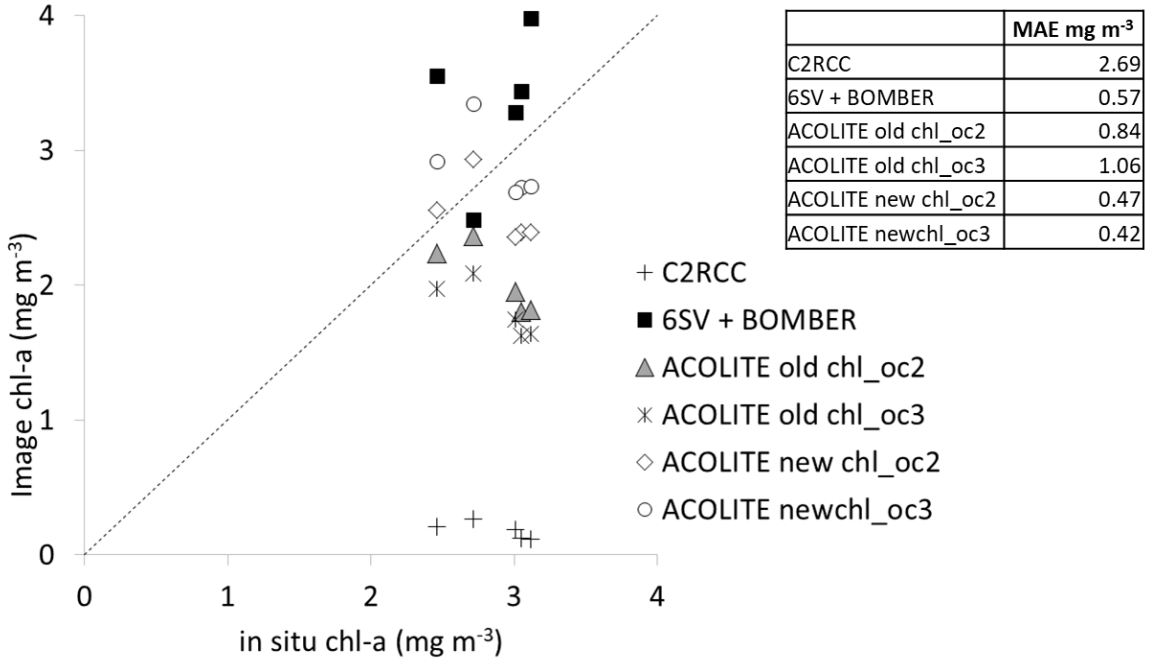

	MAE mg m^{-3}
C2RCC	2.69
6SV + BOMBER	0.57
ACOLITE old chl_oc2	0.84
ACOLITE old chl_oc3	1.06
ACOLITE new chl_oc2	0.47
ACOLITE newchl_oc3	0.42

Figure 60 Scatterplot for chl-a as measured in situ (x-axis) and L8-OLI derived (y-axis) through different algorithms over Lake Iseo. In the table on the right, MAE values for each product is shown.

5.2.3 Mantua *lakes*

The best performing **S2A/B-MSI** Rrs products, at least for band 705 over 665 nm ratio, (*6SV seasonalMicro*, *ATCOR varying* and *fixed*, and *ACOLITE new*) were used to estimate chl-a concentration through the semi-empirical algorithm (Sec. 4.4.2). For completeness, also *ACOLITE new chl_re_gons740* product included in the latest *ACOLITE* version, was validated, since over Lake Trasimeno already showed good performances. The estimates were in agreement between Gons algorithm and empirical algorithm here selected, fed with *ACOLITE new* Rrs. More in general, they were very well performing with MAE = 5.03 and 4.69 mg m^{-3} respectively. For *6SV seasonalMicro*, *ATCOR varying* and *fixed* MAE was respectively 7.53, 5.85 and 4.66 mg m^{-3} (Figure 61).

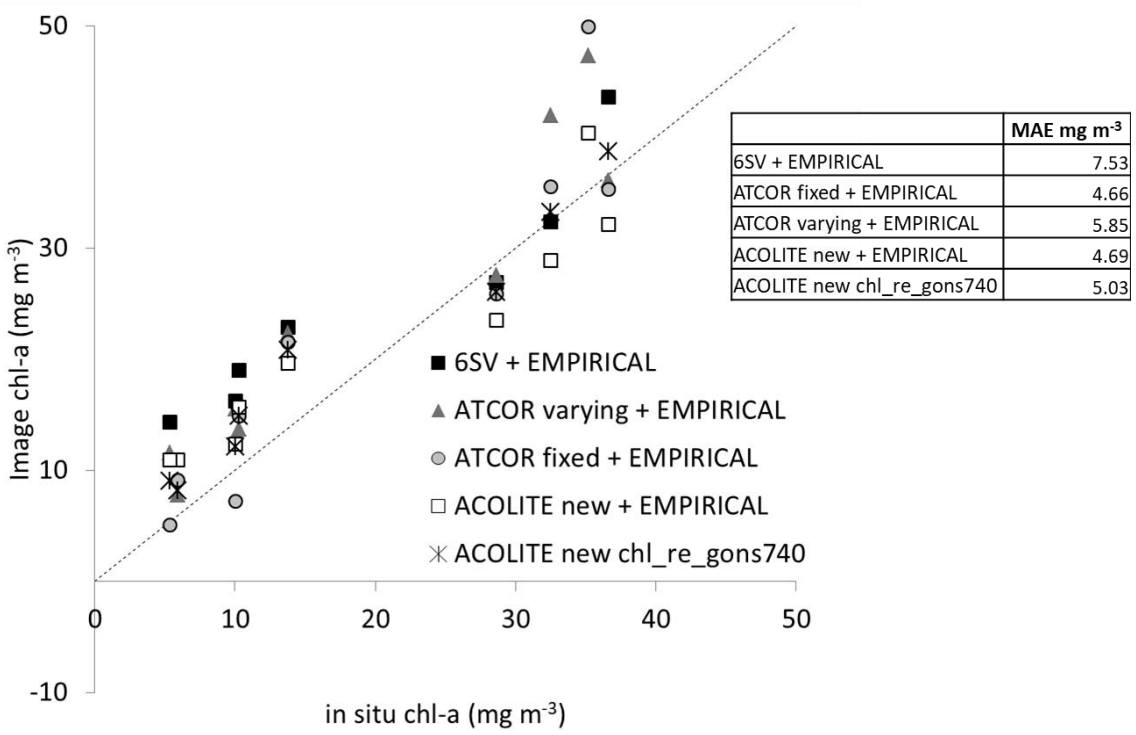

	MAE mg m^{-3}
6SV + EMPIRICAL	7.53
ATCOR fixed + EMPIRICAL	4.66
ATCOR varying + EMPIRICAL	5.85
ACOLITE new + EMPIRICAL	4.69
ACOLITE new chl_re_gons740	5.03

Figure 61 Scatterplot for chl-a as measured in situ (x-axis) and S2-MSI derived (y-axis) through different algorithms in Mantua lakes.

5.2.4 Curonian Lagoon

For Curonian Lagoon no match-ups were available for S2A derived chl-a maps evaluation, while 11 match-ups were available for S3A-OLCI. *CHL_OC4ME* products from standard OLCI product failed over all sampling points. C2RCC products, POLYMER chl-a concentration products, and semi-empirical algorithm products derived both from *6SV predefined* and POLYMER Rrs, were thus compared.

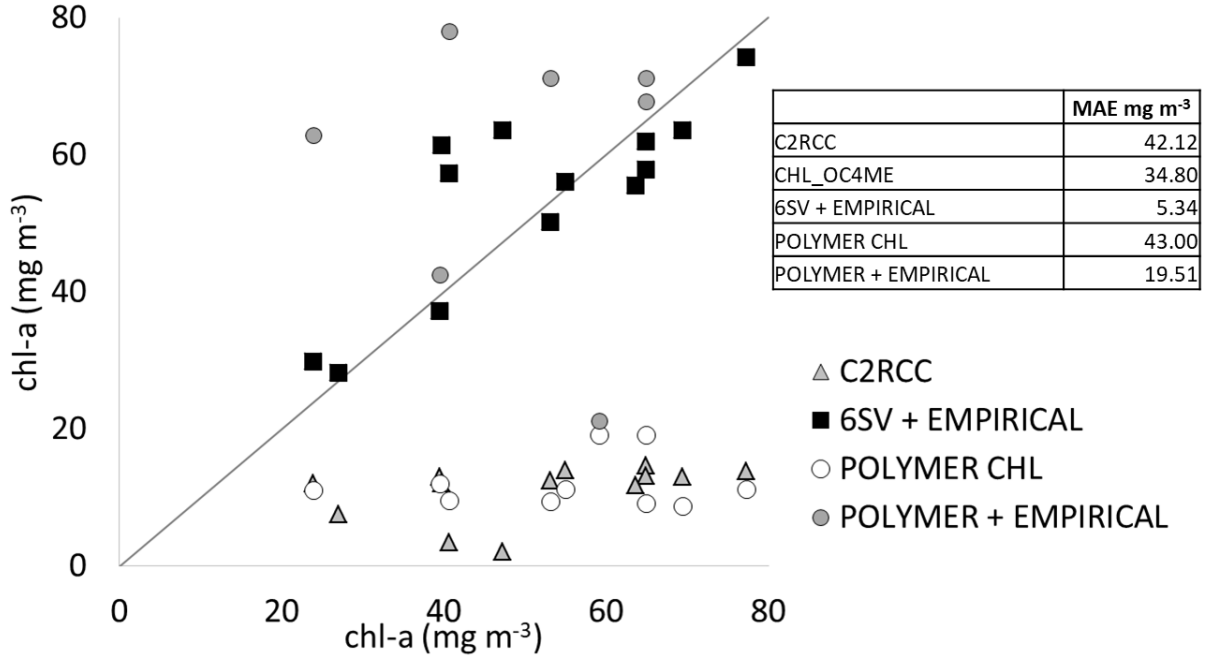

	MAE mg m^{-3}
C2RCC	42.12
CHL_OC4ME	34.80
6SV + EMPIRICAL	5.34
POLYMER CHL	43.00
POLYMER + EMPIRICAL	19.51

Figure 62 Scatterplot for chl-a as measured in situ (x-axis) and S3-OLCI derived (y-axis) through different algorithms over Curonian Lagoon.

The semi-empirical algorithm fed by *6SV predefined* Rrs products outperformed all the other combinations, including chl-a concentration product directly derived by POLYMER (named *POLYMER CHL* in the scatterplot).

5.3 S3-OLCI and S2-MSI maps inter-comparison

In order to avoid the (minor) source of errors (e.g. differences between the hour of field data collection and image acquisition) might arise when comparing satellite to field data a further exercise was carried out by comparing chl-a values as retrieved from coincident observations of MSI and OLCI. As shown in the violin plots for both lakes (Figure 63), chl-a maps showed the same trend in concentration but with a slight overestimation and a wider range by MSI respect to OLCI, mainly over Lake Garda and for dates with lower concentrations in Lake Trasimeno. Violin plots allow also, as expected, to stress the wider distribution, associated to the finer-scale mapping for MSI extracted values.

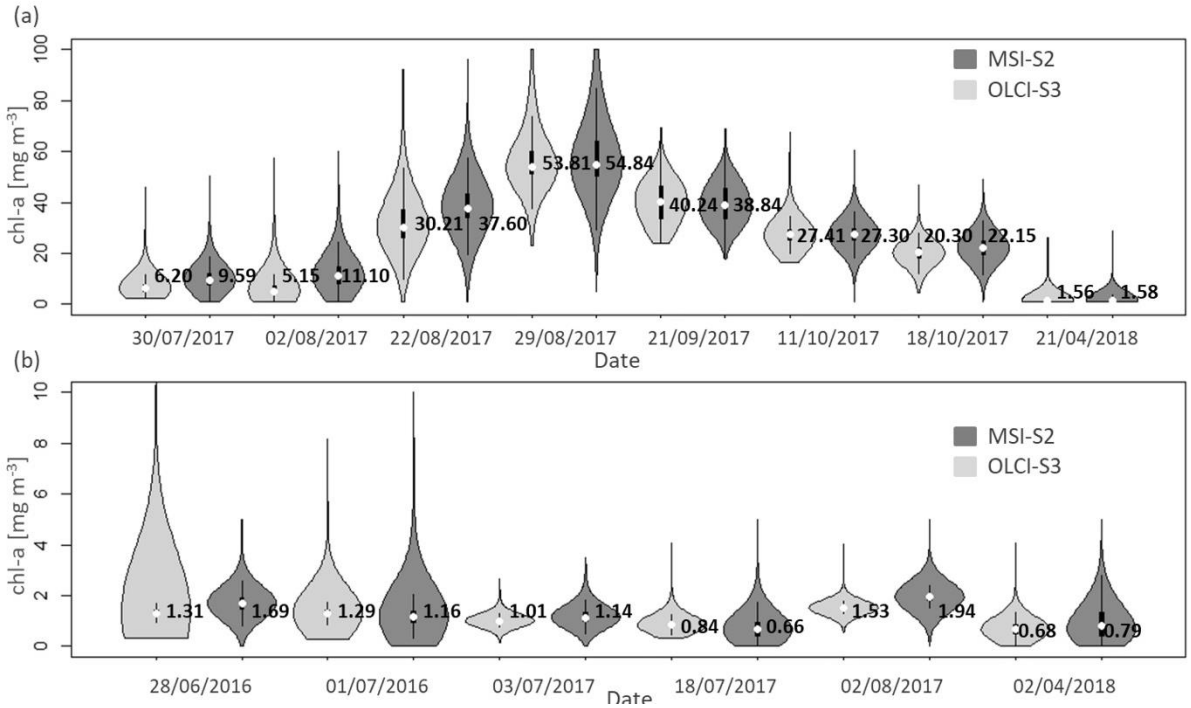

Figure 63 Violin plots for chl-a concentration values for Lake Trasimeno (a) and Lake Garda (b). Labels show median values estimated in each date by each sensor.

On the other hand, extracting mean values from smaller area (3 by 3 for OLCI and 90 by 90 for MSI, about 0.81 Km^2), despite higher variability, MSI showed both overestimated and underestimated values respect to OLCI (Figure 64).

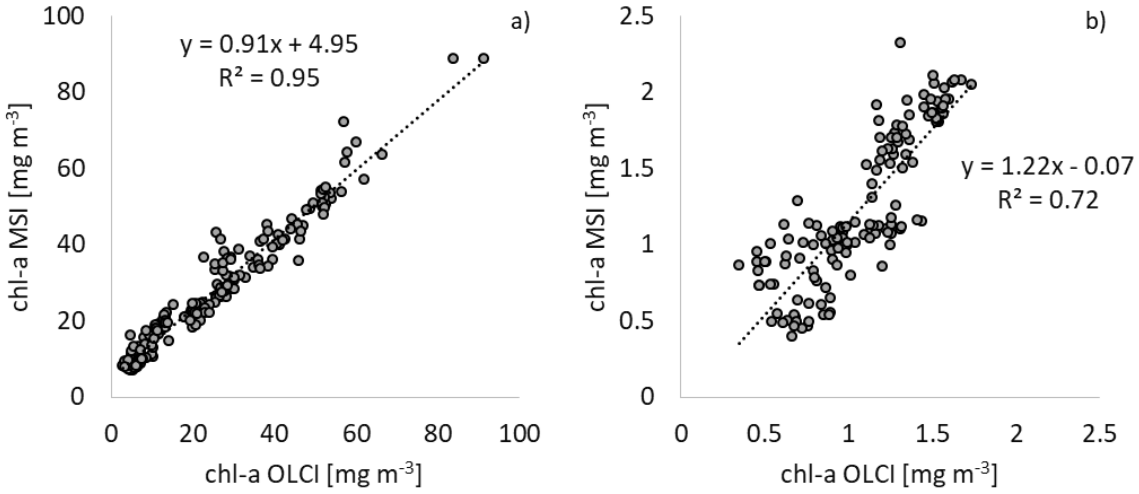

Figure 64 Scatter-plot for chl-a concentration generated from selected ROIS; a) Lake Trasimeno, b) Lake Garda.

In order to move forward users-relevant applications, over protection agencies monitoring stations (indicated in Figure 2), extracted single values from both OLCI and MSI were classified

according to the WFD thresholds, which vary according to lake macro types. In particular, Lake Trasimeno belongs to AL-4 macro type and Lake Garda to AL-3 one[8].

In Lake Trasimeno (Table 11), classification produced the same results mainly for higher values, while different results were obtained for lower values, in particular when values were very close to classes limits (e.g. on 07/08/2017 and 11/10/2017). In Lake Garda (Table 12) values remained always below the best quality level threshold excepted for 2 dates for MSI values, with values still very close to the threshold itself, i.e. 1.9 mg m^{-3}.

On the other hand, mean values obtained for each monitoring station, including all dates by the two sensors, were classified in the same quality level.

Table 11 Water quality classification based on threshold defined for AL-4 lakes macrotype for Lake Trasimeno. For each date/station the value extracted from OLCI and MSI products are reported and colours indicate quality: Light-blue = 'High', Green = 'Good', Yellow = 'Moderate', 'Orange' = 'Poor', 'Red'= 'Bad'.

Date	Station	S3	S2		Date	Station	S3	S2
30/07/2017	Centro Lago	5.40	7.15		29/08/2017	Oasi	39.68	35.99
30/07/2017	Oasi	5.32	11.37		21/09/2017	Centro Lago	35.11	33.87
02/08/2017	Centro Lago	3.77	9.17		21/09/2017	Oasi	34.12	36.89
02/08/2017	Oasi	3.03	8.11		11/10/2017	Centro Lago	26.83	26.18
07/08/2017	Centro Lago	13.53	20.90		11/10/2017	Oasi	22.58	24.70
07/08/2017	Oasi	6.16	8.32		18/10/2017	Centro Lago	21.47	22.21
22/08/2017	Centro Lago	26.17	34.62		18/10/2017	Oasi	15.22	24.31
22/08/2017	Oasi	29.28	31.61		**mean**	**Centro Lago**	**22.64**	**25.45**
29/08/2017	Centro Lago	48.87	49.47		**mean**	**Oasi**	**19.42**	**22.66**

Table 12 Water quality classification based on threshold defined for AL-3 lakes macrotype for Lake Garda. For each date/station the value extracted from OLCI and MSI products are reported and colours indicatequality: Light-blue = 'High', Green = 'Good', Yellow = 'Moderate', 'Orange' = 'Poor', 'Red'= 'Bad'.

Date	Station	S3	S2		Date	Station	S3	S2
28/06/2016	371	1.35	1.95		18/07/2017	Salò	0.58	0.55
28/06/2016	Sirmione-Padenghe	1.30	1.67		02/08/2017	371	1.53	1.82
28/06/2016	Salò	1.21	1.61		02/08/2017	Sirmione-Padenghe	1.74	2.05
01/07/2016	371	1.32	1.12		02/08/2017	Salò	1.49	1.96
01/07/2016	Sirmione-Padenghe	1.13	1.05		02/04/2018	371	0.46	0.96
01/07/2016	Salò	1.18	1.81		02/04/2018	Sirmione-Padenghe	0.77	1.14
03/07/2017	371	1.13	1.13		02/04/2018	Salò	0.54	1.00
03/07/2017	Sirmione-Padenghe	0.94	0.98		**mean**	**371**	**1.11**	**1.28**
03/07/2017	Salò	1.00	1.01		**mean**	**Sirmione-Padenghe**	**1.13**	**1.26**
18/07/2017	371	0.87	0.71		**mean**	**Salò**	**1.00**	**1.32**
18/07/2017	Sirmione-Padenghe	0.89	0.65					

[8] DM 260/2010.

Atmospheric correction products comparison showed the best performance was obtained through POLYMER and 6SV. Thus, in order to generate long time series analysis for time trend investigation in Lake Garda, POLYMER, which does not depend on any other external data availability, was used. To assess the validity of the analysis shown in this chapter, and thus the feasibility of combining MSI and OLCI data, the same image, atmospherically corrected through POLYMER before being ingested by BOMBER, were compared to OLCI 6SV derived chl-a maps. As shown in Figure 65, in the selected dates, the same results were obtained for values >1 mg m^{-3}, while MSI respect to POLYMER tends to underestimate very low values.

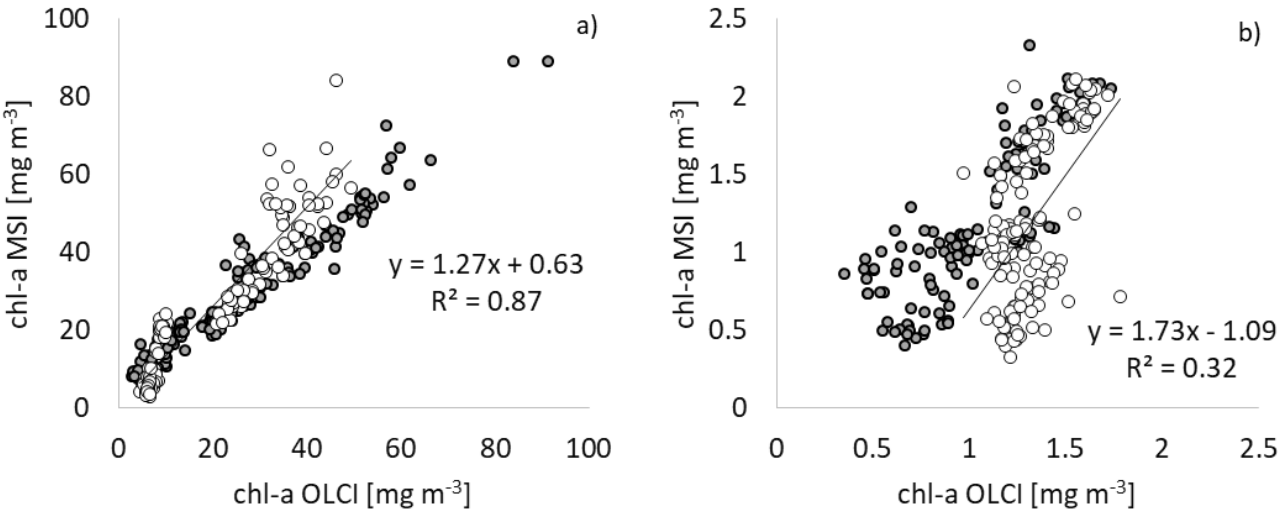

Figure 65 Scatter-plot for chl-a concentration derived from MSI and OLCI products from selected ROIS in Lake Trasimeno (a) and Garda (b); OLCI imagery was atmospherically corrected through 6SV dailyMicro (in grey) and through POLYMER (in white).

6. Environmental applications

6.1 Phytoplankton seasonal and long-time trend and phenology analysis

6.1.1 Introduction

As already mentioned in the introduction section, lakes have been identified as ECVs, being very sensitive to climate change and environmental stressors. Phytoplankton has also been identified as sensitive to environmental change, with changes in overall long-time and seasonal trends, shifts in the seasonality of blooms, or phenology, usually as a consequence of changes in temperature and nutrient pattern (Palmer et al., 2015c). In several studies, this response has been reported in terms of shift in the timing of blooms, duration and magnitude of the peak (e.g., Berger, et al., 2010; Meis et al., 2009; Winder and Sommer, 2012).

Latest satellite imagery will offer the opportunity of investigating these trends through their long times series.

6.1.2 Materials and methods

The sensors used so far in this work, having been launched only few years ago, do not offer a long time series yet, but they have been exploited in this thesis for a first application. In this section, chl-a concentration values were extracted from OLI (only Subalpine lakes, where validated), OLCI and MSI available time series maps (obtained by the best performing methods, as described in Sec. 5), over selected regions, corresponding to regional or district protection agencies sampling points in Subalpine lakes and Lake Trasimeno. In particular, a 5 by 5 cloud free pixels region was defined over each point, and mean and standard deviation of chl-a concentration were extracted. Moreover, previously validated MERIS derived chl-a concentration maps, were exploited to enlarge the time series, from 2003 to 2012. In Subalpine lakes, MERIS imagery was processed through C2R (Odermatt et al., 2010). In Lake Trasimeno, although C2R performed well in general (Giardino et al., 2008), plotting results time series with *in situ* data, an underestimation during intensive bloom was clearly shown, despite an excellent performance over date characterised by lower chl-a concentration (Figure 68). To overcome this problem, the MPH algorithm available as a tool in SNAP was used on intensive bloom dates, and time series (MPH and C2R derived) were

merged together. MPH exploits bottom-of-Rayleigh reflectance peaks in the red and near-infrared bands above a baseline, drawn between the bands at 664 nm, and 885 nm and it was already successfully used to detect intensive algal blooms in GLaSS project (2015). Criterion for selecting the processor to be applied on each date was based on the presence or absence of the characteristic peak round 708 nm, already at TOA Rayleigh corrected reflectance level.

Satellite-derived and *in situ* time series were then plotted against time to stress potential seasonal trends, using seasonal boxplot to identify seasonal peaks.

As shown in seasonal boxplot in results, for Lake Trasimeno a clear pattern during the year was observed, with large values of chl-a concentration in late summer and autumn. The analysis was thus carried out annually, fitting a Gaussian function of time to each annual series for each station. The shifted Gaussian function in Eq. 18 is empirical and chosen as in Platt et al. (2008) and Zhai et al. (2011), since its parameters can have a physical interpretation.

$$B(t) = B_0 + \frac{h}{\sqrt{2\pi}\sigma} e^{-\frac{(t-t_m)^2}{2\sigma^2}} \quad [\text{Eq. } 18]$$

B_0 is the background value of chlorophyll concentration, *h* the integral of the chl-a concentration under the curve, σ the peak width, and t_m (day of year; doy) the peak date. Thus $H = \frac{h}{\sqrt{2\pi}\sigma}$ is the amplitude of the bloom. Bloom initiation was defined as the time when the chlorophyll concentration $B(t) - B_0$ reaches 20% of H. Both seasonal pattern and phenology data were compared within the lake to observe potential differences among different areas and across the years.

In subalpine lakes, usually a first growth phase was observed in late winter, a second one in late spring, and a third one in autumn, but with several peaks recorded in summer in several years. As several peaks within the same season occurred, it was not possible to fit a Gaussian curve for every year and season: for this reason the analysis was thus carried out comparing average seasonal parameters, dividing each year as January-April, May-August, and September-December, with, for each year, the date of the highest peak and its magnitude in each quarter.

Finally, exploiting the long time series, a trend tests was conducted, through a Seasonal Kendall test (Hirsch and Slack, 1984), as in Boyer et al. (1999) and Räike et al. (2003), to stress eventual long period trends in trophic conditions. The test is a modification of the Mann-Kendall test, a non-parametric test, which allows taking into account seasonal patterns in the search for

monotonic trends over time (Hirsch and Slack, 1984), available in the TimeTrends software provided by Niwa, New Zeeland (https://www.niwa.co.nz/freshwater/management-tools/water-quality-tools/analysis-of-water-quality-trends). In the original Mann-Kendall test, the statistic S, which is the difference between the number of pairwise slopes that are positive minus the number of negative pairwise slopes, is calculated by listing values in temporal order. The null hypothesis condition is the absence of temporal trends in the data time series, with a confidence limit of 5%. In seasonal modification, the same statistic is calculated on each season *i* separately and then the results are combined by summing all statistic S_i for each season *i* over all seasons to form the overall test statistic S*k*. Along with this test, the Sen Slope estimator is calculated as an estimate of median annual slope, calculating the median annual slope respect to all possible pairs of values in each season. Temporal trends were considered meaningful if p-value was less than 0.05 and if the calculated Sen's Slope was at least 1% of the median value.

To ensure the robustness of the results, a second test was conducted. It is a seasonally adjusted parametric trend test, which first removes seasonality from data fitting a GAM curve (generalized Additive Model, Hastie and Tibshirani, 1990) with seven degrees of freedom, to the annual pattern. Residuals are calculated as the difference between measured values and predicted value from GAM plus overall mean of data. These residuals are then used for a linear regression looking for possible trends. As in the first test, the null hypothesis is that slope is not meaningfully different from zero with a confidence level of 5%. For this task, the slope was considered meaningful if estimated slope per year was at least 1% of the median value.

6.1.3 Results

6.1.3.1 Lake Trasimeno

Over Lake Trasimeno seasonal trend was clearly visible in time series plot and seasonal boxplot (Figure 66 and Figure 67), with highest peaks concentrated in late summer-autumn, when usually cyanobacteria blooms occurred. Intensity of the bloom varied along years, with lowest value in 2003, 2006, and 2007, and this pattern was shown by both *in situ* and satellite-derived chl-a concentrations.

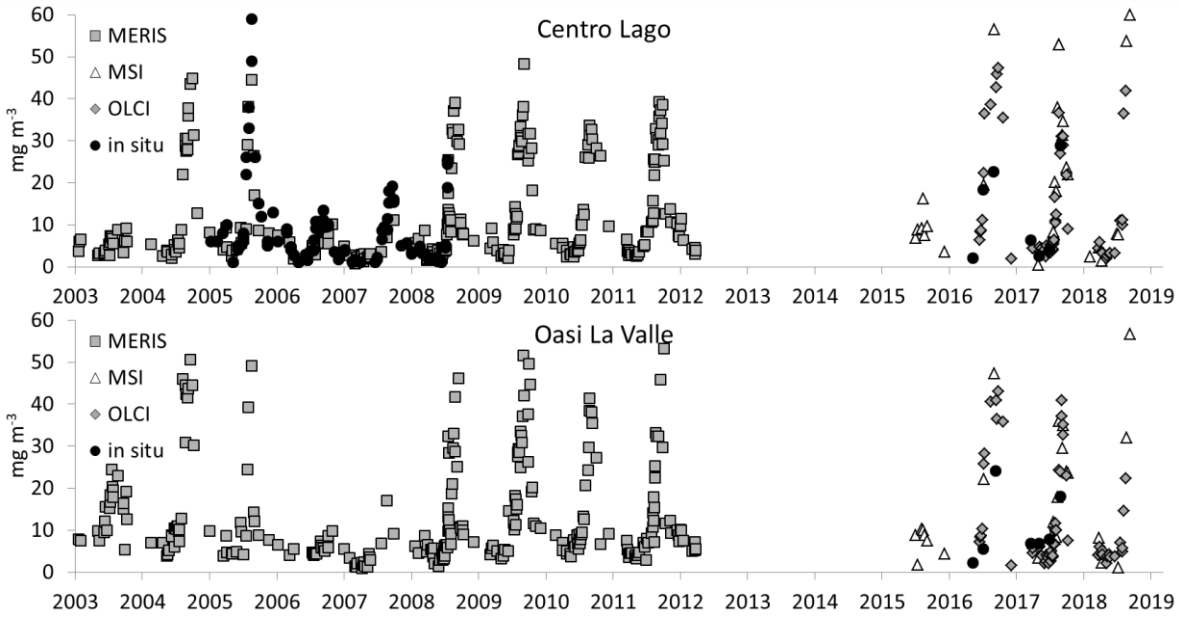

Figure 66 Chl-a concentration in Lake Trasimeno over the two ARPA Umbria monitoring stations, obtained from all available remote sensing maps and in situ measurements from January 2003 to September 2018 (n=494 for Centro Lago and 362 for Oasi La Valle stations).

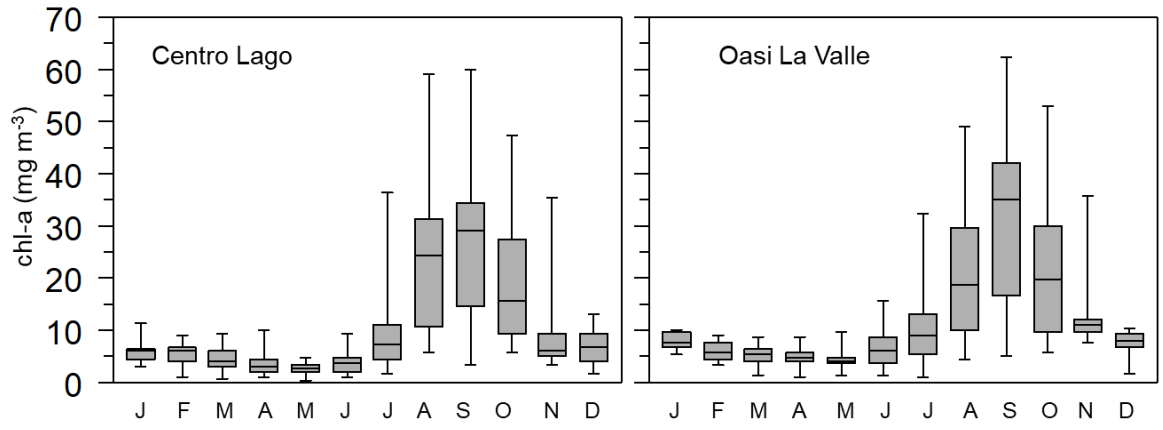

Figure 67 Seasonal boxplot for chl-a concentration in Lake Trasimeno over the two ARPA Umbria monitoring stations, obtained from all available remote sensing maps and in situ measurements from January 2003 to September 2018 (n=494 for Centro Lago and 362 for Oasi La Valle stations).

Phenology analysis showed strong differences in both starting date of phenology and maximum peak date. In particular the bloom reached its maximum on the earliest date in 2005, and on the latest in 2006. Duration of the bloom ranged between 3.36 days in 2003 (in Centro Lago, it was 5.14 for Oasi in 2015) and 29.26 in 2017. In 2018, only data until end of September were available, thus, even if Gaussian curve was able to fit time series, only day of peak is reported, in italic.

Table 13 Phenology analysis results. for each station/year tm (day of year of the peak; doy) is reported together with bloom initiation (t20, doy) the background value of chl-a concentration (B0), and the amplitude of the bloom (H). When data could not be fit by the Gaussian curve the doy of the maximum chl-a value for the year is reported in italic.

	tm		t20		B0 (mg m^{-3})		H (days)	
Year	**Centro**	**Oasi**	**Centro**	**Oasi**	**Centro**	**Oasi**	**Centro**	**Oasi**
2003	233	222	161	121	4.2	9.33	3.36	12.53
2004	260	*253*	206		10.35		25.72	
2005	*230*	*230*						
2006	306	*306*	261		5.06		4.76	
2007	*275*	244		172		2.46		15.02
2008	241	244	183	185	6.53	7.78	22.99	22.71
2009	250	255	185	185	12.45	15.56	21.04	19.59
2010	249	250	185	202	8.5	9	20.88	28.84
2011	258	264	198	204	10.14	10.04	22.65	22.94
2015	*235*	233		204		5.42		5.14
2016	267	264	214	188	18.35	17.13	27.33	18.14
2017	248	259	200	204	8.3	7.69	29.26	24.8
2018	*251*	*168*						
Mean	**249**	**241**	**192**	**185**	**10**	**9**	**21.65**	**18.86**

In Centro Lago station an increasing trend was shown by Seasonal Kendall's test (Table 14 and Figure 68) with a Median annual slope of 0.173 mg m^{-3} per year, while a negative slope was assessed for Oasi La Valle station, -0.277 mg m^{-3} per year.

Table 14 Seasonal Kendall Test results for Lake Trasimeno. In bold, meaningful Sen Slope.

Lake	Station	Median value	p-value	Median annual Sen slope	5% confidence limit	95% confidence limit
Trasimeno	Centro Lago	6.45	0.0	**0.173**	0.091	0.271
Trasimeno	Oasi	8.75	0.0	**-0.277**	-0.405	-0.155

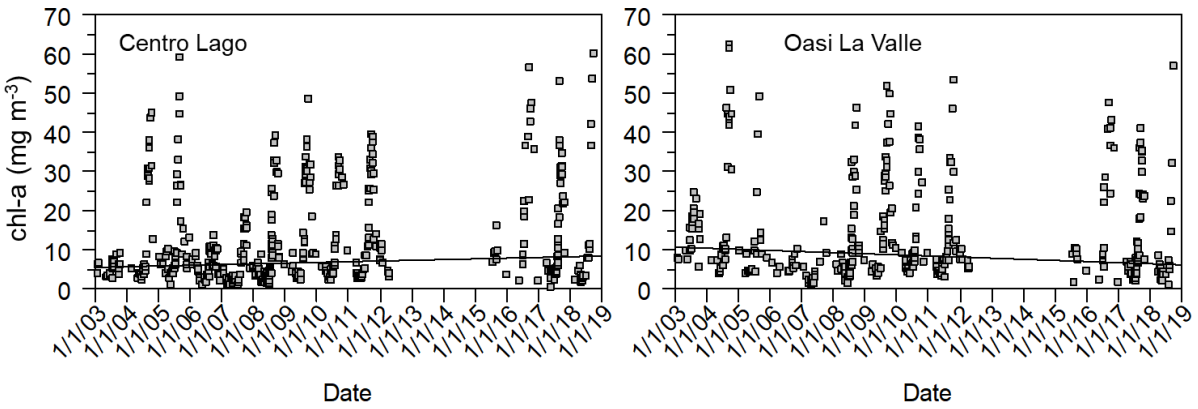

Figure 68 Trasimeno time serie for Centro Lago and Oasi La Valle stations and Sen's Slope as estimated frothrough Seasonal Kendall's test.

The slight trend was already visible in MERIS time series and confirmed by Kendall Test run for the period 2003-2012 only: the Median annual Sen Slope was 0.374 mg m^{-3} (p-value = 0) for Centro Lago station and not meaningful for the southern station (Oasi La Valle)

From the whole time series, the second test, Seasonal adjusted trend test, confirmed these trends, showing an increasing trend for Pelagic station and a negative trend for the other, as shown in Table 15.

Table 15 Seasonal Adjusted Trend test results for Lake Trasimeno. In bolt characters meaningful slope

Station	H_0: no slope	Slope per year	Standard Error	p-value
Centro Lago	Rejected	**0.336**	0.085	0
Oasi	Rejected	**-0.21**	0.104	0.044

6.1.3.2 Subalpine lakes

As shown in seasonal boxplot for subalpine lakes (Figure 69), seasonal trends were also present in subalpine lakes, but with a completely different patterns: phytoplankton productivity reached its maximum during spring, and, even if not every year, in autumn. On the other hand, single blooms were also recorded during summer period, also due to cyanobacteria blooms, especially in August-September (e.g. blooms described in Sec. 6.3).

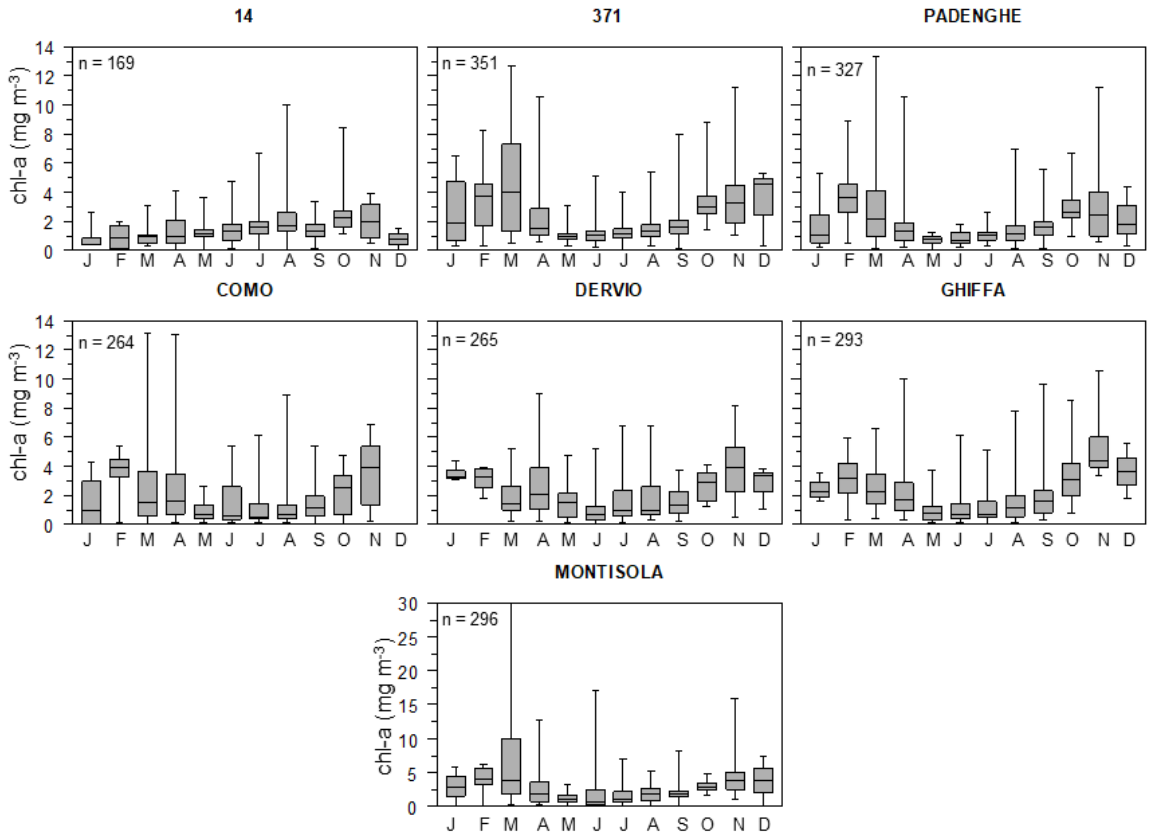

Figure 69 Seasonal boxplot for chl-a concentration in selected stations: 14, 371 and Padenghe in Lake Garda; Como and Dervio in Lake Como; Ghiffa in Lake Maggiore; Montisola in Lake Iseo.

Since the method used for Lake Trasimeno was thus not here applicable, seasonal mean and peaks were extracted for selected stations time series, and shown in Figure 70 to assess different behaviour along time and among stations. Obviously, results are conditioned by image availability, but still allowed to show some interesting pattern in time series. First of all, it is notable as the most cases, pattern among year remained more or less the same in all three seasons, i.e. the year with the highest values in the first quarter, was the one with highest values also in second and third quarters (mostly for years 2003-2006 and 2009-2011).

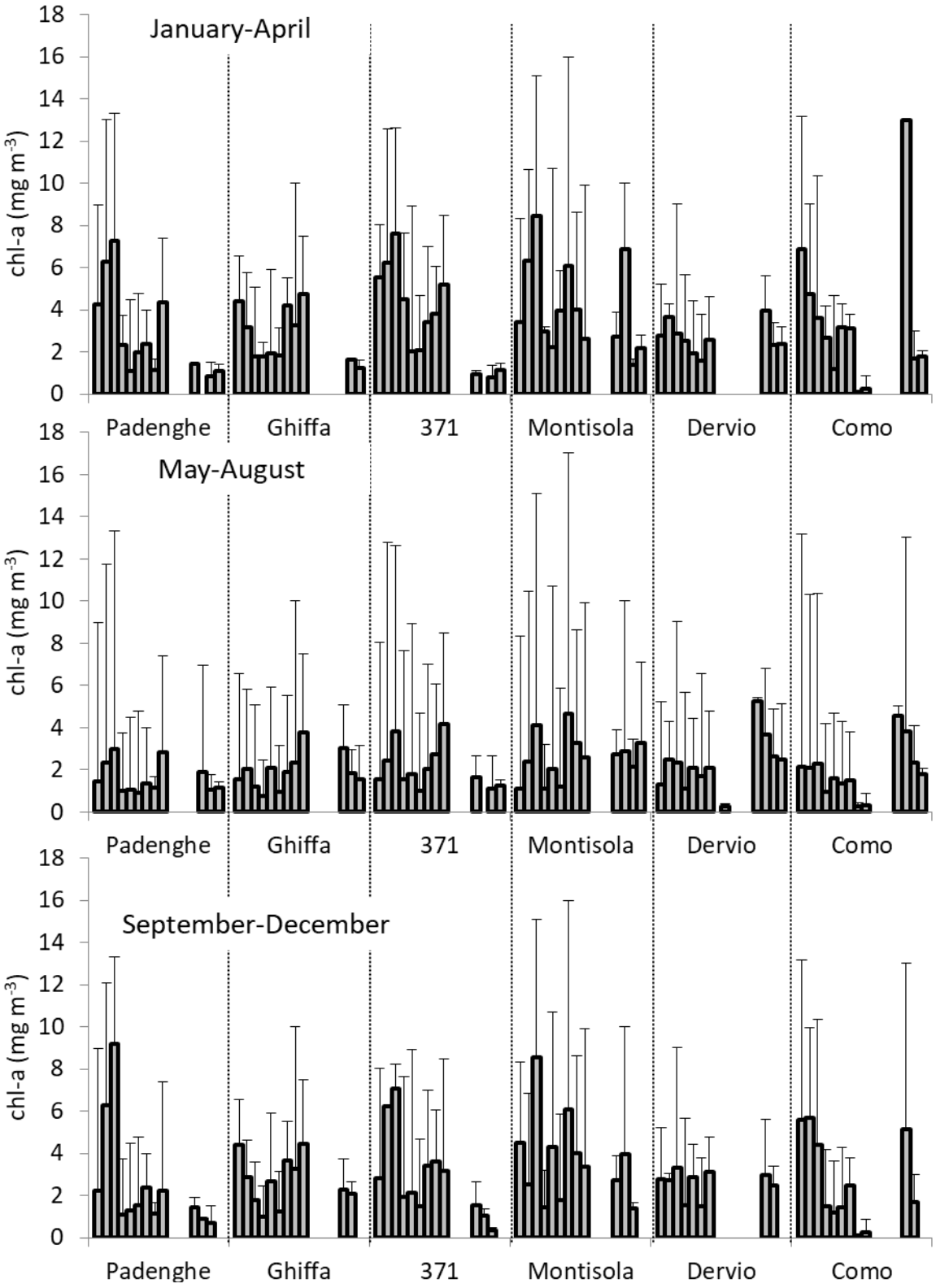

Figure 70 Histograms of mean chl-a values for each year (from 2003 to 2018) and station, divided by seasons. Error bars shows maximum concentration for each season.

Considering all available values since 2003 to 2018, Seasonal Kendall test revealed a slight increasing trend for all lakes, stronger for Lake Maggiore and Iseo (Table 16 and Figure 71).

In addition Lake Garda in particular, a more pronounced, but still small, trend was recorded for Northern area (station 14), respect to South-West (Padenghe) and South-East (371) basins. Also in Lake Como, the slope was more pronounced in Northern station (Dervio).

Table 16 Seasonal Kendall Test results for Subalpine lakes. In bold, meaningful Sen Slope.

Lake	Station	Median value	p-value	Median annual Sen slope	5% confidence limit	95% confidence limit
Garda	371	1.27	0	**0.037**	0.027	0.047
	14	1.37	0.013	**0.071**	0.028	0.093
	Padenghe	1.09	0	**0.042**	0.033	0.051
Como	Como	0.76	0	**0.052**	0.027	0.082
	Dervio	1.43	0	**0.093**	0.068	0.123
Maggiore	Ghiffa	1.30	0	**0.103**	0.083	0.125
Iseo	Montisola	1.65	0	**0.104**	0.083	0.126

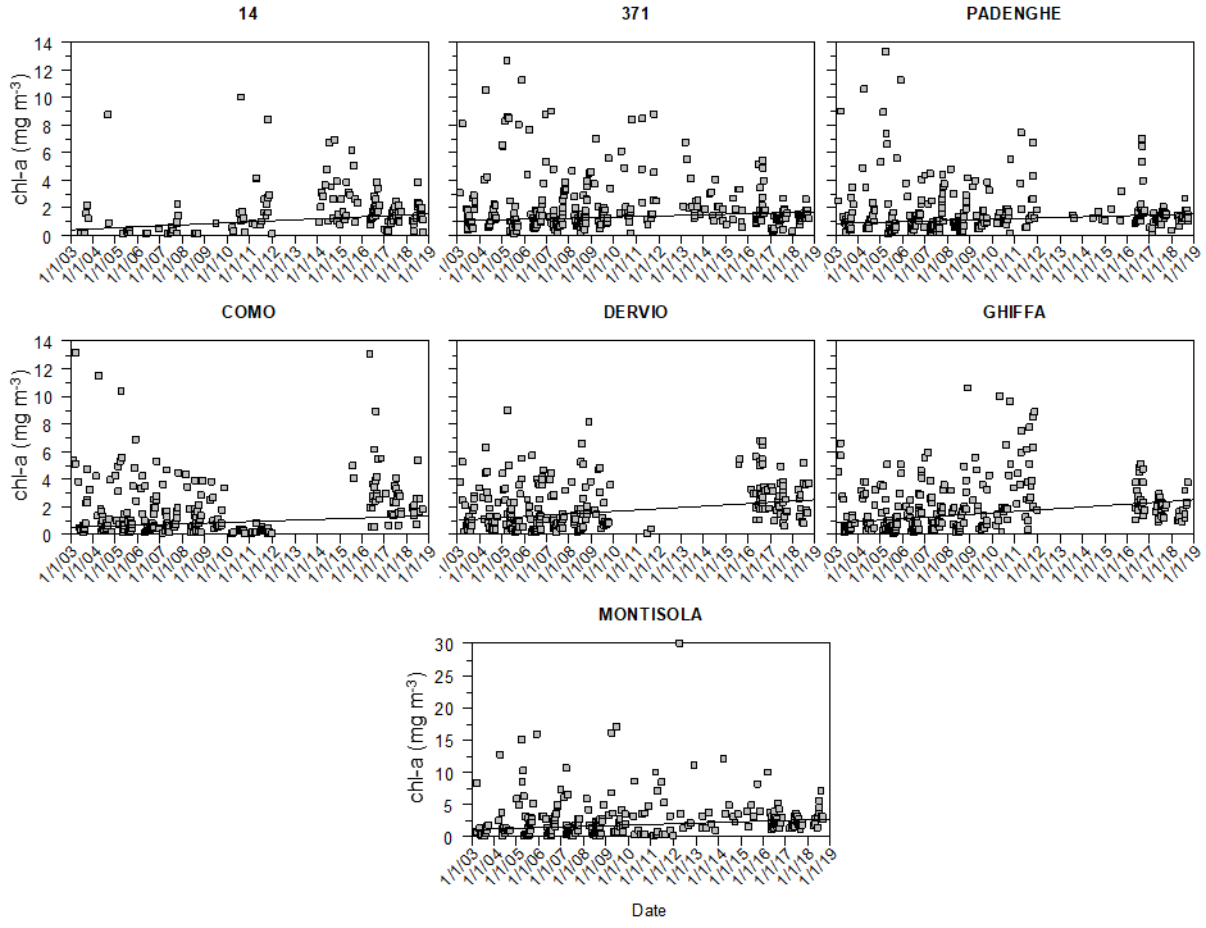

Figure 71 Chl-a concentration and Kendall Slope as obtained through Seasonal Kendall test, obtained from all available remote sensing maps and in situ measurements from January 2003 to September 2018, in selected stations: 14, 371 and Padenghe in Lake Garda; Como and Dervio in Lake Como; Ghiffa in Lake Maggiore; Montisola in Lake Iseo.

These trends were only partially confirmed by the Seasonal Adjusted Trend test, confirming only the trend for lakes Como, Maggiore and Iseo: the test was not able to refuse the hypothesis of no slope presence in Lake Garda.

Table 17 Seasonal Adjusted Trend test results for subalpine lakes. In bold characters, meaningful slope.

Station	H_0: no slope	Slope per year	Standard Error	p-value
Como	Rejected	**0.084**	0.025	0.001
Dervio	Rejected	**0.107**	0.018	0.000
Ghiffa	Rejected	**0.115**	0.02	0.000
Montisola	Rejected	**0.082**	0.035	0.019
Padenghe	Fail to reject	-0.004	0.017	0.789
14	Fail to reject	0.049	0.027	0.073
371	Fail to reject	-0.024	0.018	0.171

On the other hand, increasing trend in chl-a is in accordance with water temperature time trend: in Rogora et al. (2018) study, positive trends of water temperature were recorded in all the lakes during the decade 1994–2004, with warming rates between 0.02 and 0.05°C/year. In addition for this thesis, water level values recorded from 2003 to 2018 for each lake, collected by ARPA Lombardia, were analysed through the same Seasonal Kendall's test: a decreasing trend in water level was observed for all lakes excepted, as for chl-a, for Lake Garda as reported in Table 18, confirmed by the Seasonal adjusted trend test.

Table 18 Seasonal Kendall's test for lakes water level (2003-2018).

Lake	Median value	p-value	Median annual Sen slope
Lake Maggiore	61.9	0	-0.657
Lake Como	39.4	0	-0.494
Lake Garda	47.5	0	0.343
Lake Iseo	47.9	0	-0.57

6.2 WFD classification

6.2.1 Introduction

As a second application, chl-a maps time series extracted from available and validated imagery, was exploited to simulate the implementation of remotely sensed data in support of WFD monitoring activities. The sampling protocols adopted across European Union suggest a minimum number of samples per year for phytoplankton analysis, on a seasonal basis, which means four samples per year. Monitoring plans are a compromise between the effort/cost required from the

agencies in charge of monitoring and the need of describing the seasonal ecological variability in the water body analysed. Some member states, including Italy, increased this frequency to 6 samples per year, including in addition to the four seasonal samples, two other samples in transitional period, when phytoplankton is rapidly changing (Bresciani et al., 2011; Giardino et al., 2014b). Chl-a concentration is than averaged along each year and compared to chl-a limits used to classify the water bodies.

On the other hand, even increasing the frequency, results of the classification can be strongly influenced by date sampling choice, mainly whenever rapid blooms occurred, and by sampling site points position, whenever chl-a concentration variability within the lake is high.

Including remote sensing data could allow to capture extreme and transient events. The improvement provided by the exploitation of remote sensing data for this second case is fully described in the next chapter, on phytoplankton bloom detection, as well as some works in the latest two decades, on the application of remote sensing data over inland and coastal waters (e.g. Chen et al., 2007, in the Gulf of Finland; Gohin et al., 2008 in French Atlantic continental shelf and the English Channel, Kratzer et al., 2014, Sweden coastal areas; Bresciani et al., 2011, in subalpine lakes; and Alikas et al., 2015, in Swedish and Estonian large lakes).

6.2.2 Material and methods

Since application over subalpine lakes has been already assessed and fully described by Bresciani et al. (2011), although for MERIS time series only, Lake Trasimeno whole time series, already used in the previous chapter, were exploited here to simulate the advantage obtained from introducing chl-a remote sensing derived data into WFD classification process over this lake.

Time series was divided according to Italian official protocol for sampling lake phytoplankton, according to WFD (Buraschi et al., 2008), as reported in Table 19.

Table 19 Reference ranges defined by official protocol for sampling lake phytoplankton, according to WFD (Buraschi et al., 2008).

Season	Reference range
Winter	1 January–20 March
Spring	1 April–15 May
Summer	1 July–31 August
Autumn	1 October–31 November
Spring–summer transition	15 May-15 June
Summer–autumn transition	1 September–1October

For each year and defined season, a random date among available in chl-a maps time-series was chosen and for each year the six values thus obtained were averaged, to simulate the WFD results gathered with *in situ* sampling frequency. Then, the whole time series was included and average value for each year was used to classify surface water lake, according to chl-a concentration limits defined in Wolfram et al., 2009.

6.2.3 Results

Results in histogram in Figure 72 clearly show the impact of date choice in both lake sampling stations: classification resulted different in 2004, 2005, 2009, 2010, 2011, 2016, 2017 in both directions, towards classes of better or worse quality.

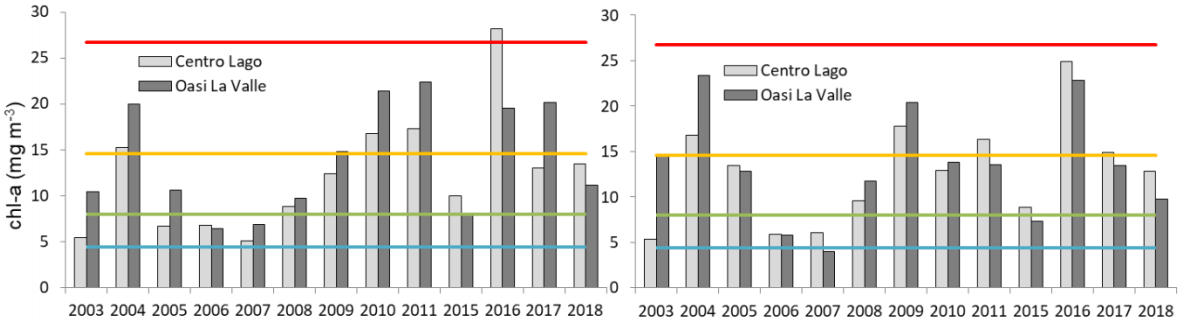

Figure 72 Yearly mean chl-a concentration (mg m^{-3}) in Lake Trasimeno in Centro Lago and Oasi La Valle monitoring stations, obtained using random samples for each sampling season (left) and all available data (right). Horizontal lines indicate WFD boundaries for water quality status classification based on chl-a concentration, respectively, blue: high/good status, green: good/moderate, yellow: moderate/poor, red: poor/bad (Wolfram et al., 2009).

6.3 Algal bloom in subalpine lakes

6.3.1 Introduction

The development of cyanobacterial blooms has become a serious problem in recent decades, since many species are able to produce secondary metabolites toxic to many organisms, including humans.

Cyanobacteria thus can potentially harm lake ecosystems through food web disturbance and anoxia due to massive bloom events, affecting the lake ecosystem, human health (water supply, food contamination), and the economic activities linked to fishery and the recreational use of lakes. On the other hand, being one of the world's oldest known organisms (Schopf, 2000), cyanobacteria can adapt very well to environmental changes, being able to migrate vertically in the water column looking for light and nutrients (Gallina et al., 2013). In addition, several recent studies showed how temperature increase could positively influence the presence of these

organisms (Gallina et al., 2011; Paerl and Paul, 2012). As reported by Callieri et al. (2014), blooms of *Dolichospermum lemmermannii* can be occasionally recorded even in deep subalpine lakes, as supported by nutrient pulses deriving from the mineralization of organic matter deposited along the lakeshore and released through runoff during rainfall events.

To plan possible measures for managing and protecting natural ecosystems affected by extensive cyanobacteria blooms, it is important to obtain timely and synoptic information (Bresciani et al., 2016a), but the typical dynamics of cyanobacterial blooms, which also have a very fast replication rates, make it difficult to perform a quantitative monitoring of number of cells and spatio-temporal distribution as surface blooms can appear and disappear quickly, often within few hours (Sellner et al., 2003; Agha et al., 2012). For this reason, *in situ* measurements alone could not even record the phenomenon occurrence or not be able to assess its spatial distribution on a larger scale. The capability of latest sensors imagery of capturing these phenomena, as a support to limnologic measurements, was thus assessed, exploiting L8-OLCI and S2A-MSI imagery over subalpine lakes, during a cyanobacteria bloom event, occurred in summer 2016, results being published in Bresciani et al. (2018). As S3A-OLCI imagery became available after 2017 reprocessing, when available on additional dates, OLCI derived maps were also integrated in the analysis, decreasing sampling time frequency. S3A imagery was not used for Lake Idro, being the lake too small to be investigated with OLCI 300 m spatial resolution.

6.3.2 Materials and methods

The assessment of the bloom events by using the chl-a concentration as a proxy, was developed first from L8 and S2A (and later S3A) imagery acquired in late summer, being this period the most likely season of cyanobacterial bloom events in subalpine deep lakes, in particular, from August to September 2016. During this period, some blooms were observed in subalpine lakes, and water samples for phytoplankton species and composition were also available for four (Maggiore, Como, Idro and Garda) of the five investigated lakes. The taxonomic composition and density of phytoplankton were analysed under a Zeiss inverted microscope according to Utermöhl's method (1958) by ISE-CNR and ARPA Lombardia. Phytoplankton organisms were identified at the species level or, if not possible, assigned to a genus only. Lakes have been sampled once, during August, except Lake Maggiore, where two samples have been collected in September.

A common image-processing chain was applied to all sensors to obtain Top Of Atmosphere (TOA) radiances, as described in Sec. 4.2. Atmospheric correction was performed through *6SV dailyMicro*

for L8-OLI and S2A-MSI imagery, through POLYMER for S3-OLCI, and chl-a maps were derived through BOMBER (Sec. 0, b, 4.4.1).

6.3.3 Results

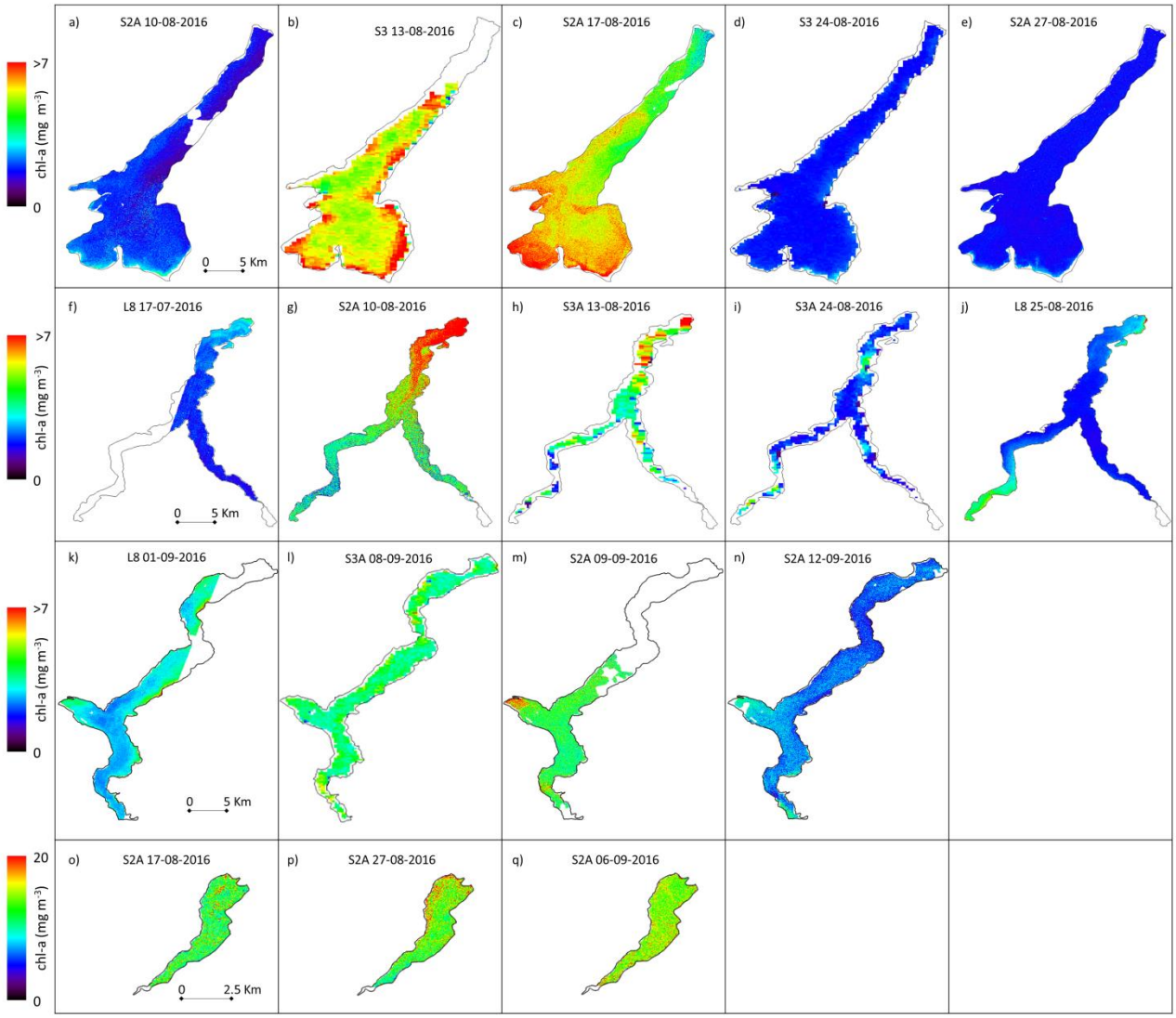

Figure 73 Chl-a concentration maps for the time windows of algal bloom events on each lake. From the top: Garda (a–e), Como (f–j), Maggiore (k–n) and Idro (o-q).

Chl-a concentration maps in Figure 73 show the bloom events detected in the 2016 for Garda, Maggiore, Como, and Idro. In case of Lake Iseo imagery analysis did not revealed any significant quick bloom in the same period occurred and therefore it was left out from the analysis. In Lake Garda, chl-a concentration was higher during the bloom in particular in the Southern part of the lake, where it increased up to 8 mg m^{-3}. The same increase is very clear in the Northern part of Lake Como (up to 10 mg m^{-3}): on this period spatial pattern allowed also recognising the bloom extension from the North, towards Southern part of the lake. Also in Lake Maggiore the increase

was more evident in the western area (up to 7 mg m^{-3}), where Toce Western tributary is located. Finally, for Lake Idro, for which also *in situ* data showed the presence of cyanobacteria since the first decade of August, it is very clear the different spatial pattern, with higher values concentrating in a smaller part of the lake during the bloom event.

Specifically, in Lake Idro the phytoplankton analysis (August 10th) detected the presence of cyanobacteria (40% of the total abundance), represented in terms of abundance mainly by *Chroococcus* cfr *turgidus* (27%), Chrysophytes, represented by the genus *Ochromonas* (27%), and in a smaller part (8.7%) by the Diatom *Fragilaria crotonensis*, although reaching 52.5% as biomass.

In Lake Garda, the phytoplankton sample of August 2016 revealed a *Dolichospermum lemmermannii* bloom. Different species of cyanobacteria, belonging to Chroococcales and Oscillatoriales, with the genus *Aphanothece* (*A. clathrata* and *A. nidulans*) and *Planktothrix rubescens*, *Pseudoanabaena limnetica* and *Tychonema bourrellyi* respectively, were found in the sample analysed for Lake Como on August 11th. However, in terms of biomass *Planktothrix rubescens* (51.2%) and *Tychonema bourrellyi* (21%) are the dominant species.

Lake Maggiore was affected by a cyanobacteria bloom in September 2016. Three samples were taken for phytoplankton analysis in Lake Maggiore on September 10th, 19th and 26th respectively. The sample of September 10th revealed a surface bloom of *Dolichospermum lemmermanni* in the southern part of the lake (91.1% in terms of density, with minor contribution by *Microcystis aeruginosa* (5%) and *D. planctonicum* (2.5%)). In the central part of Lake Maggiore *Oscillatoriales* were found. The blooms were mainly due to *Pseudoanabaena* spp., an unusual condition in Lake Maggiore, as this taxon commonly blooms in eutrophic water bodies (Mayer et al., 1997; Zwart et al., 2005). Also, in the two samples collected in the central station, several species belonging to *Oscillatoriales* have contributed to the algal bloom, among which *Pseudananabaena* dominated, both in terms of density (68.6%) and biomass (47.2%). *Dolichospermum* genera (*D. lemmermannii* e *D. planctonicum*) contributed respectively to 27.9% and 7.6% in terms of biomass.

In order to complete the analysis, and to understand the whole environmental conditions in which these rapid events can occur, meteorological data (from ARPA Lombardia monitoring stations next to the lakes), potentially affecting algal growth, were considered over the events time window.

Nutrients arriving from the lake catchment area, as a result after rainfall events, can stimulate phytoplankton growth, especially in oligo-mesotrophic lakes (Morabito et al., 2012), and, combined with a seasonal increase in water temperature, it would facilitate *D. lemmermannii*

proliferation (Olrik et al., 2012; Salmaso et al., 2015). Calm conditions are known to be advantageous for buoyant cyanobacteria which move toward the euphotic zone in response to reduced turbulent mixing (Jöhnk et al. 2008; Zilius et al., 2014), and in the days of surface blooms analysed in this study, wind was relatively calm (Figure 74).

In Figure 74, precipitation, air temperature and wind velocity are shown in the period analysed for this case study. Data show that, for deep lakes, short-term weather conditions of precipitation and air temperature were not directly correlated with blooms phenomena.

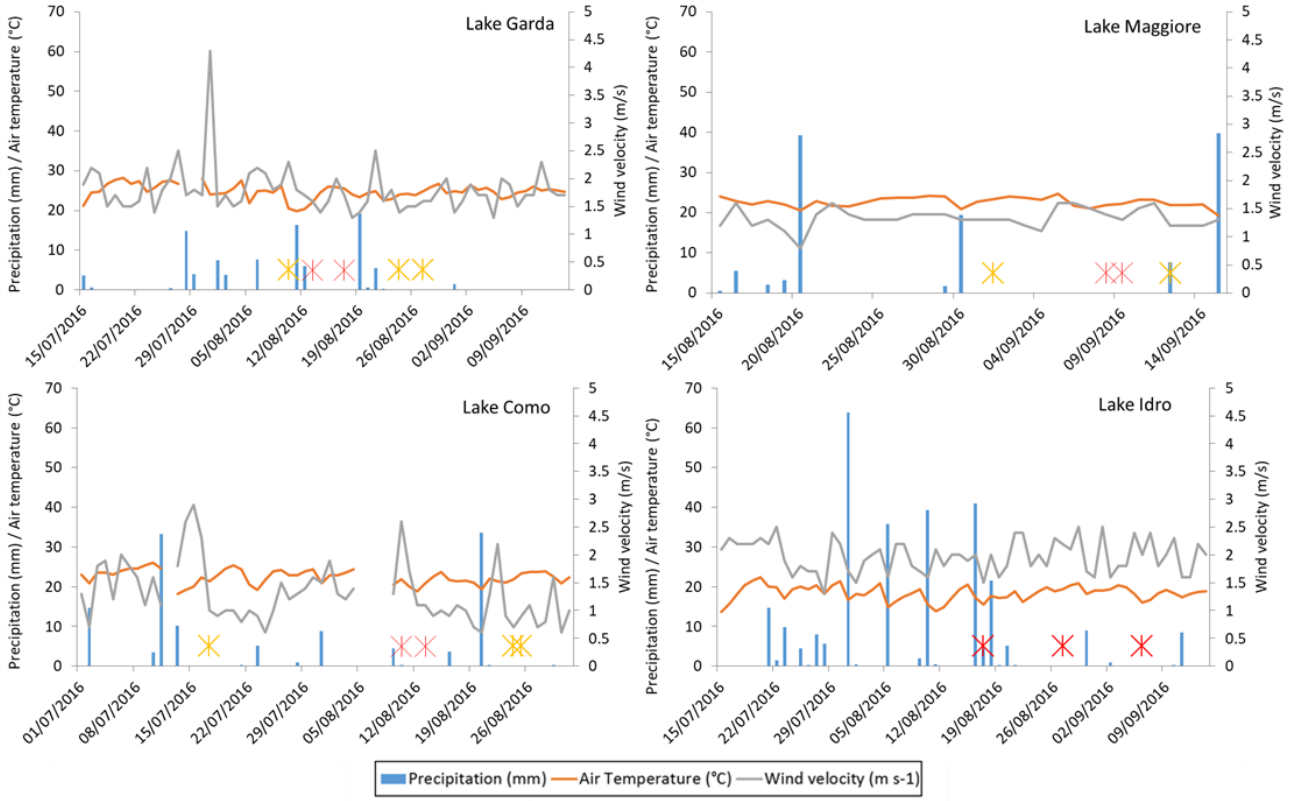

Figure 74 Precipitation, air temperature and wind speed from some ARPA meteorological stations next to the lakes. Stars indicate images dates (red stars indicate the dates of the image in which blooms were detected).

6.3.4 WFD perspective

In Figure 75, the histograms of the chl-a concentration distribution for each image related to the WFD scale status are shown. The results show the advantages to use synoptic view characterizing the whole water surface of the single lakes. Results from maps obtained from Lake Garda and Lake Maggiore on dates without the blooms are comparable to median results from long time series analysis (sec. 6.1.3.2).

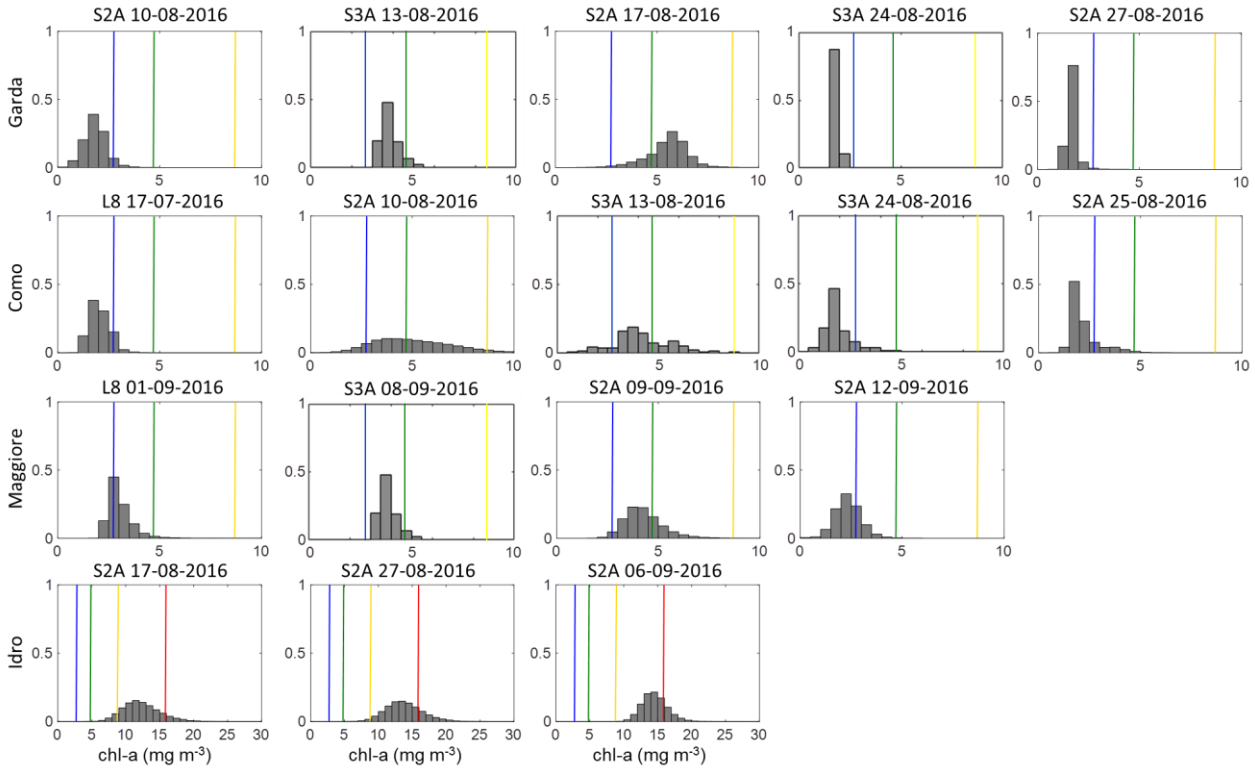

Figure 75 Chl-a concentration (mg m^{-3}) distribution for each image: chl-a concentration on x-axis and fraction of total pixel on y-axis. Vertical lines indicate WFD boundaries for water quality status classification based on chl-a concentration, respectively, blue: high/good status, green: good/moderate, yellow: moderate/poor, red: poor/bad (Wolfram et al., 2009).

The detection and the analysis of the characteristics and spatial and temporal trend of these rapid events were carried out through remote sensing techniques, while traditional limnological measurements alone would not have been enough to completely describe and, in some cases, even to identify these blooms. For example, in Lake Garda the bloom was directly observed during IRA-CNR radiometric field campaigns on 17th August 2016. Chl-a concentration that was measured in the same day by the Provincial Environmental Agency (APPA) in the monitoring point in the Northern part of the lake, would not have allowed to identify the bloom in the southern area (Figure 73 c). Considering chl-a concentration in all the stations used by different agencies for lake monitoring, values extracted by images in the lake showed that even if measures had been collected on these days in all the monitoring stations, only some of them would have identified the huge variation in chl-a concentration, and none of them would have shown the highest concentration. In the south-eastern basin, the estimated chl-a concentration reached 8.91 mg m^{-3}, with a coefficient of variation of 0.87.

In Lake Como, the bloom was detected by *in situ* measurements on August 2016 11th and 17th in a Northern and in a Southern part respectively: remote sensing products, differently from punctual

measurements, allowed describing the spatial distribution of the bloom, not uniformly distributed in the lake, even with the coarser resolution of S3A-OLCI.

7. Conclusions and perspectives

The results of this thesis confirmed the suitability of S3-OLCI sensors, as an improved successor of MERIS and of other ocean colour sensors, for resolving the water leaving reflectance in optically complex waters, and for supporting water quality monitoring in medium size lakes. In addition, although not primarily designed for observing the optical properties of water, this study is also showing how the higher spatial resolution imagery of S2A/B-MSI and L8-OLI have suitable characteristics to support the fine-scale environmental monitoring.

The scope to evaluate the state-of-the-art of the processors for the atmospheric correction was achieved by using a consistent set of reference measurements collected in the field during satellite overpasses; more than 200 match-ups of satellite and *in situ* data were collected. The results of the comparison show that, for S3A-OLCI, the best results for the atmospheric correction were obtained both by the 6SV-based algorithm, parametrised by specific aerosol microphysical properties and by POLYMER. The Rrs values computed from both algorithms were then directly used to retrieve chl-a concentrations. To the aim, the inversion of the bio-optical model implemented in the BOMBER code was used as it provided the best match to *in situ* chl-a measurements. For S2A/B-MSI and L8-OLI, the best results for the atmospheric corrections were obtained from 6SV and by ACOLITE. Overall, since both 6SV and BOMBER have been parametrised with site-specific data (i.e. AERONET and the specific inherent optical properties of the investigated lakes), these results are suggesting that methods for converting at-satellite radiances into chl-a concentrations perform well when the site-specific knowledge of optical properties of both water and atmosphere are used to constrain model's calibration. This is particularly relevant in case of clear water lakes as, in turbid eutrophic waters, all the processors were converging to same Rrs values (in particular for ACOLITE-old version, 6SV and POLYMER). In case of turbid waters, also the chl-a products generated by the latest version of ACOLITE provided similar results to BOMBER, while the Neural Network C2RCC mostly failed or highly underestimated chl-a concentrations.

The comparative analysis of chl-a concentration mapped with BOMBER from high spatial S2A/B-MSI (corrected with 6SV) and from high frequent S3A-OLCI (corrected with POLYMER) resolutions,

showed a very good match. The agreement was found in both subalpine lakes and Lake Trasimeno. This result is encouraging the synergistic use of S2A/B and S3A/B sensors (with S3B not analysed in this study) to support environmental applications based on satellite technology.

The environmental applications developed in this study demonstrated the benefit of remote sensing to operational lake waters monitoring, such as the WFD reporting and the algal bloom monitoring. In particular, it is clear how the synoptic observations from space allow to investigate and characterize the spatial and temporal variability of phytoplankton, both seasonally and along years. To the aim, the multi-temporal dataset from S2 and S3 was extended to MERIS in order to cover the latest 15 years. The results in subalpine lakes, where the seasonal trend tests on chl-a values derived from both remote sensing and field data was accomplished, showed a slight trend towards higher concentration for all lakes except for Garda. For Lake Trasimeno an increasing trend, in the Pelagic station *Centro Lago* was also assessed, while a decreasing trend occurred towards the coast, nearby the *Oasi La Valle*.

For capturing algal blooms, the observations from all sensors were considered relevant because a short revisit time is a key element to catch the blooms dynamic, typically characterised by a high degree of change. In particular, three fine-scale algal blooms (characterised by cyanobacteria) were detected in subalpine lakes in summer-autumn 2016 by combining S2A-MSI and L8-OLI. The results underlined how synoptic data at pixel size from 10 to 30 m are relevant to identify blooms occurring in circumscribed limited areas (e.g. South-West basin in Lake Garda, Northern area in Lake Como, West basin in Lake Maggiore).

For the WFD perspective, the use of multi-temporal satellite data allowed to assess the improvement in water quality classification. In particular, in Lake Trasimeno satellite data showed how classification results might change depending on the date of sampling. Then, in case of algal blooms, the analysis revealed how punctual measurements (as *in situ* measurements are) besides not providing a complete description at the lake-scale, might fail in catching the bloom.

To conclude, the results achieved in this study confirmed the applicability of the latest generation sensors to generate water quality products in lake waters, in particular for the clear blue deep lakes in the Italian subalpine ecoregion, in the turbid and shallow Lake Trasimeno, and in the eutrophic Curonian Lagoon, then largest in Europe. However, although satisfying results were already achieved with currently available techniques, there is room for improvement.

In particular, an effort in the investigation of how the examined processors perform in environmental conditions not covered by this study is needed for e.g. mapping algal blooms in ample range from low to high concentrations; for retrieving Rrs in case of high concentrations aerosols and/or water vapour, as in North Italy could often occur. These situations, even if rare might in fact occur and might be interesting for users as they might deal with early warning applications.

Then, in this study, performances of atmospheric correction algorithms were evaluated in the part of the spectrum involved downstream the processing chain in chl-a retrieval, while many other bio-physical parameters can be retrieved from satellite data. A further effort could be made to fully characterize the impact of different processors on other water quality indicators such as the suspended particulate matter or the coloured dissolved organic matter.

An investigation of the impact of adjacency effects, often augmented by accidental orography, due to lands nearby lakes, would be also needed to evaluate a possible improvement of atmospheric correction processors. To the aim, a future study might include other tools, such as iCOR (De Keukelaere et al., 2018), that take care of adjacency effects.

Finally, since field data is the main reference to measure the accuracy of satellite-derived products, it would be extremely important to characterize also the accuracy of *in situ* measurements. These measurements are in fact collected and analysed with different protocols and methods, depending on the country, on lake type or on the involved institution. Therefore, a look forward to the results that are going to be achieved by international projects (such as the H2020 EOMORES, HYPERNETS, MONOCLE) dealing with this issue is relevant to continue the validation exercise initiated in this study. In particular, these projects are setting up a series of fixed spectrometers for autonomously collect high frequency Rrs that, by collecting measured every e.g. 30 minutes, enable to compile relevant data-base of *in situ* data. In particular, one of this systems (namely the EOMORES WISPStation) is already working in both Lake Trasimeno and in the Curionan Lagoon since summer 2018; while a system belonging to HYPERNETS network (www.hypernets.eu) should be placed in Lake Garda at the end of 2019.

Finally, it is also time to look forward to the near-future hyperspectral satellite missions (e.g. ASI-PRISMA, DLR-ENMAP, NASA/JPL-SBG, with PRISMA to be launched on 22 February 2019). Imaging spectrometry offers in fact unique opportunities to both retrieve bio-geochemical parameters in aquatic ecosystems and to improve atmospheric corrections due to its capacity in measuring at

continuous wavelengths and thus describing all the features due to absorption and scattering processes of sun light passing throughout water and atmosphere layers.

ANNEX I - Atmospheric correction algorithms

In this appendix, all the algorithms and processors used in this thesis for atmospheric correction are described, together with options and configurations selected case by case:

a) a 6SV based algorithm
b) POLYMER
c) ATCOR
d) ACOLITE
e) Sen2Cor – MSI Level2A
f) OLCI Level2 products
g) C2RCC

a. 6SV

The 6SV code (Second Simulation of the Satellite Signal in the Solar Spectrum – Vector, Vermote et al., 2006) is the vector version of 6S, a basic RT code used for calculation of look-up tables (LUTs) in the MODIS atmospheric correction algorithm, based on the approximations and implementation of the successive order of scattering (SOS) algorithm. 6S simulates the atmospheric radiative transfer in the 400-2500 nm spectral range at a spectral resolution of 2.5 nm. It was used in this thesis through an interface realised by CNR-IREA to include as input to 6SV also microphysical properties of aerosols as provided by AERONET stations close to study areas, and specific sensors Spectral Response function. 6SV allows in fact to simulate for each defined band the radiative transfer, according to the geometry of the acquisition and the atmospheric condition over the target area. Columnar ozone and water vapour concentrations can be defined through both predefined models as in Table 20, or user-defined values. The gaseous transmission is calculated from a random exponential band model: Goody and Yung (1996) model is used for water vapour and Malkmus (1967) model for Oxygen, Ozone, Carbon dioxide, methane, and nitrous oxide. 6SV assumes that all gases apart from water vapour and ozone are uniformly mixed within the atmosphere and of constant density over time (Proud et al., 2010). Aerosol type can also be defined both through predefined models, characterized by different percentage of four different components (dust-like, water-soluble, oceanic, and soot), which can be also defined by the user. In

addition, it allows to describe aerosol through microphysical properties (particles size distribution and Complex Refractive Index, $m = n - ik$, which describes scattering and absorption properties of atmospheric particulate matters) as estimated through sunphotometers measurements.

Table 20 Atmospheric profiles available for 6SV parametrization.

Code	Atmospheric profile	Water Vapour (g/cm^2)	Ozone (cm-atm)
0	No gaseous absorption	0	0
1	Tropical	4.120	0.247
2	Mid-latitude Summer	2.930	0.319
3	Mid-latitude Winter	0.853	0.395
4	Subarctic Summer	2.100	0.480
5	Subarctic Winter	0.419	0.480
6	US standard 62	1.420	0.344

Finally, aerosol load can be described both through visibility values or Aerosol Optical Thickness (AOT) at 550 nm.

In particular in this thesis, where AERONET sites were available close to target area, and thus for Subalpine Italian lakes (with ISPRA and Sirmione AERONET sites), AERONET values of AOT and microphysical properties were used parametrizing 6SV, if data were available within a time interval of 3 hours from each image acquisition (***6SV DailyMicro*** in plots). On these sites, to test the suitability of the method when no measurements were available, an alternative correction was applied, with aerosol microphysical properties defined using a median seasonal curve as defined in Annex II (***6SV SeasonalMicro*** in plots). AOT and water vapour concentration have been then provided to 6SV from MODIS-Aqua/Terra products, retrieved from NASA Giovanni interface (https://giovanni.gsfc.nasa.gov/giovanni/, Acker and Leptoukh, 2007). OMI-Aura (Ozone Monitoring Instrument) products were used for Ozone concentration.

For the other study areas (Lake Trasimeno and Curonian Lagoon) where no AERONET stations are available, MODIS and OMI products were used to select concentrations, while fixed predefined models were used, Marine and Continental, characterized by aerosol components as described in Table 21 for Curonia and Trasimeno, respectively (***6SV predefined*** in plots).

Table 21 Aerosol models selected for atmospheric correction, and relative percentage of aerosol components as defined in 6SV.

	Dust-Like	Oceanic	Water-Soluble	Soot
MARITIME	0	95	5	0
CONTINENTAL	70	0	29	1

As output, for each band λ, 6SV provides, among others, the integrated values of global, water, ozone, CO_2, oxygen, NO_2, CH_4, and CO gaseous transmittance; total, Rayleigh, and aerosol scattering transmittance; and direct, diffuse and environmental irradiance. In addition, it provides three coefficients $x_a(\lambda), x_b(\lambda)$, and $x_c(\lambda)$ applicable to obtain water reflectance ρ_w from Radiance at Top of Atmosphere $L_{toa,}$ as in Eq. 19. For each site, target elevation was accounted for, and a Lambertian ground surface was assumed.

$$\rho_w(\lambda) = \frac{L_{toa}(\lambda)\, x_a(\lambda) - x_b(\lambda)}{1 + x_c(\lambda)\,(L_{toa}(\lambda)\, x_a(\lambda) - x_b(\lambda))} \; [Eq.\,19]$$

The 6SV-derived atmospherically corrected ρ_w was then converted into Rrs above water dividing it by π.

b. POLYMER

POLYMER (POLYnomial based algorithm applied to MERIS, Steinmetz et al., 2011), developed by HYGEOS is an algorithm for multi-sensor atmospheric correction, used in the frame of the Ocean Colour Climate change Initiative and in operational services since 2008. It includes a water model inside the process of atmospheric correction, dealing at the same time with issues due to glint, absorbing aerosols and adjacency effects. The strength of POLYMER is due to the fact that it takes into account the whole spectrum to model atmospheric contribution.

The signal is first corrected for the effect of ozone transmission and of the Rayleigh scattering, and a first guess of the glint contribution $\rho_{\mathrm{mol+gli}}(\lambda, V_{\mathrm{wind}})$ is removed, estimated as in Cox and Munk (1954), using the wind speed values provided by ECMWF (European Centre for Medium-RangeWeather Forecasts). The total contribution of Rayleigh scattering, the sun glint and the coupling between Rayleigh scattering and sun glint is calculated with the Successive Order of Scattering radiative transfer code SOS and stored in look-up tables.

$$\rho'(\lambda) = \frac{\rho_{TOA}(\lambda)}{t_{oz}} - \rho_{\mathrm{mol+gli}}(\lambda, V_{\mathrm{wind}}) \; [Eq.\,20]$$

where t_{oz} is the ozone transmission, depending on the total ozone concentration obtained from ECMWF data. The atmosphere contribution and the residual sun glint are than modelled as a polynomial with three terms:

$$\rho_{ag}(\lambda) \approx T_0(\lambda)c_0 + c_1\lambda^{-1} + c_2\lambda^{-4} \; [Eq.\,21]$$

where $T_0(\lambda)$ is the transmission factor calculated as in Eq. 22.

$$T_0(\lambda) \approx e^{-\tau_m(\lambda)\left(1-0.5\,e^{-\frac{\rho_{gli}}{\rho_{gli,0}}}\right)\left(\frac{1}{\mu_s}+\frac{1}{\mu_v}\right)} \quad [Eq.\,22]$$

In equation 22, μ_s and μ_v are the cosines of the solar and view zenith angles, and τ_m is the Rayleigh optical thickness: $\tau_m(\lambda) \approx 0.00877\lambda^{-4.05}$. ρ_{gli} is the glint contribution estimated at the first step and $\rho_{gli,0}$ is the threshold equal to 2% used to switch between the direct (in the sun glint areas, where $\rho_{gli} > \rho_{gli,0}$) and diffuse (outside sun glint areas, where where $\rho_{gli} < \rho_{gli,0}$) transmission factors.

A second model, a bio-optical water reflectance model, is than used to estimate water reflectance just above the surface from the chlorophyll concentration [chl] and the backscattering coefficient of non-co-varying particles bbNC(λ) as in Morel (1988) and Morel and Maritorena (2001):

$$\rho^{+}_{\mathrm{wmod}}([chl], b_{bNC}, \lambda) = \begin{cases} \rho^{+}_{\mathrm{wMM}}([chl], b_{bNC}, \lambda) & \lambda < 700\ nm \\ \dfrac{\rho^{+}_{\mathrm{wS}}(\lambda)\rho^{+}_{\mathrm{wMM}}([chl], b_{bNC}, 700nm)}{\rho^{+}_{\mathrm{wS}}(700nm)} & \lambda \geq 700\ nm \end{cases} \quad [\mathrm{Eq.}\,23]$$

where

$$\rho^{+}_{\mathrm{wMM}}([chl], b_{bNC}, \lambda) = 0.544\ \rho^{-}_{\mathrm{wmod}}([\mathrm{chl}], \mathrm{bbNC}, \lambda) = f\frac{0.5b_w(\lambda) + b_{bp}(\lambda) + b_{bNC}(\lambda)}{a(\lambda)} \quad [Eq.\,24]$$

with $b_w(\lambda), b_{bp}(\lambda)$, and $b_{bNC}(\lambda)$ being the scattering coefficient of pure water multiplied by a factor 1.3 for taking into account salinity effects, and the backscattering coefficients of particles and of non-covarying particles, respectively. $a(\lambda)$ is total absorption. As shown in equation 23, the model is extended from 700 nm to 900 nm, by using the similarity spectrum for turbid waters (Ruddick et al., 2006).

The conversion to reflectance above the surface is done by assuming that the radiance in-water is Lambertian.

The estimate of the polynomial parameters (c_0, c_1, and c_2), $[chl]$, and b_{bNC} are estimated through the spectral matching between water reflectance estimated by the two different models. Starting from a starting couple of values $([chl], b_{bNC})$, an iterative process calculates $\rho^{+}_{\mathrm{wmod}}(\lambda)$, then used to retrieve $\rho_{ag}(\lambda)$ as the difference between $\rho'(\lambda)$ and $t(\lambda)\rho^{+}_{\mathrm{wmod}}(\lambda)$.

The tuple (c_0, c_1, and c_2), is estimated through polynomial fit to $\rho_{ag}(\lambda)$. The RMSE (Root Mean Squared Error) of this fit is thus evaluated along the spectrum and used as cost function. The final

values of $([chl], b_{bNC})$ are obtained by a n-dimensional iterative minimization technique of the cost function, using a simplex method as described in Nelder and Mead (1965). At the end of the process, $\rho_w(\lambda)$ is finally obtained as:

$$\rho_w(\lambda) = \frac{\rho'(\lambda) - T_0(\lambda)c_0 + c_1\lambda^{-1} + c_2\lambda^{-4}}{t(\lambda)} \quad [Eq.25]$$

As output, *POLYMER* provides both ρ_w, from which Rrs is obtained dividing by π, glint reflectance and chl-a concentration maps.

c. ATCOR

ATCOR (Richter and Schläpfer, 2014) is a software using look-up tables calculated through MODTRAN®5 RT code. In particular, in this thesis, ATCOR-2 module for multispectral sensors was used. It allows an image-based atmospheric correction with automatic retrieval of visibility and water vapour concentration, if dedicated bands are available for the sensor (at list red and near Infrared, best combination: 1.6 and 2.2 µm), as in the case of MSI and OLI sensors, exploiting known radiometric behaviour of Dark Dense Vegetation objects.

Before starting the process of atmospheric correction, ATCOR pre-classifies image pixels as land, water, haze, clouds, as shadows pixels. If the sensors has a SWIR band, dark pixels in this band are searched in the image (over land only), defined by the constrain ρ(SWIR) < threshold, where threshold is 5(10)%, or increased to 10(15)%, or 12(18)%, if less than 1% of image pixels are detected as dark, at 2.2(1.6) µm.

If red and NIR bands are available, radiance in these bands in reference pixels is used to define the visibility as the intersection with the at sensor simulated radiance (through LUTs values of path radiance, atmospheric transmittance, global flux and geometry, Figure 76).

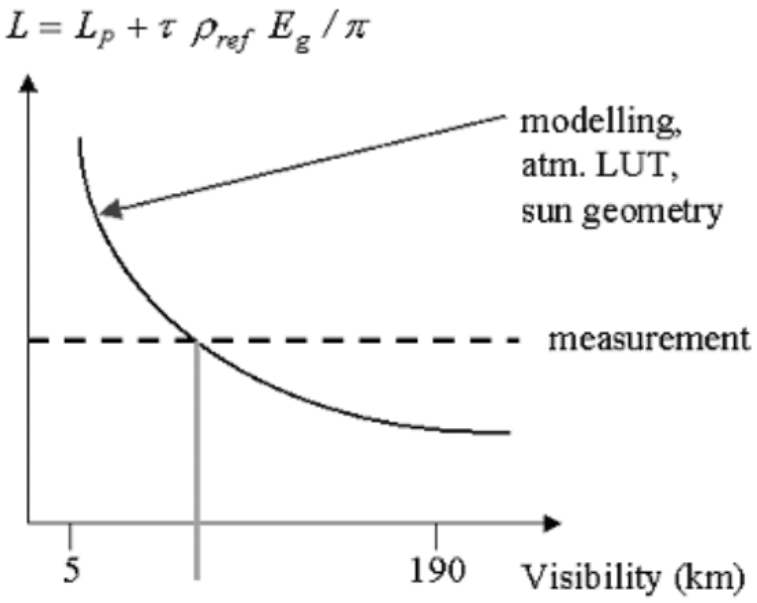

Figure 76 Schematic sketch of visibility determination in reference pixel. Source (Richter and Schläpfer, 2012).

If SWIR bands are available, for reference pixels, correlation between red and blue bands to the SWIR band is considered and visibility is estimated automatically. The SWIR reflectance is calculated assuming a visibility of 23, and thus ρ_{red} is calculated as:

$$\rho_{red} = 0.5\rho_{2.2} \text{ or } \rho_{red} = 0.25\rho_{1.6}\ [Eq. 26]$$

and from ρ_{red}, ρ_{blue} is calculated as in Eq. 27:

$$\rho_{blue} = 0.5\rho_{red} + 0.005\ [Eq. 27]$$

Visibility is estimated for Red and Blue channels as the intersection of the at sensor simulated radiance curves (through LUTs values of path radiance, for a given geometry and transmittance τ and at ground irradiance E_g) and the retrieved ρ_{red} or ρ_{blue} respectively. Path radiance is estimated as:

$$L_{PATH} = L_{TOA} - \frac{\tau\rho_{ref}E_g}{\pi}\ [Eq. 28]$$

Where ρ_{ref} is ρ_{blue} or ρ_{red}, and E_g is the surface irradiance.

The ratio among L_{PATH} at Red over Blue is thus used to retrieve the aerosol model, comparing it to the same ratio for four different aerosol models (*rural, urban, maritime, desert*), obtained through MODTRAN simulation:

$$d = \frac{L_{PATH}^{red}/L_{PATH}^{blue}}{L_{PATH,MODTRAN}^{red}/L_{PATH,MODTRAN}^{blue}} \; [Eq.29]$$

The model giving the closest d value to 1 is thus selected.

Alternatively, a definition through external data of the visibility and the type of aerosol is possible.

Since aerosol retrieval does not use bands sensitive to water vapour absorption (bands around 820, 940, and 1130 nm), the retrieval of water vapour concentration can be assessed after aerosol retrieval through the APDA algorithm (Schlaepfer et al., 1998). At the same time, the water vapour algorithm depends on aerosol properties. It is retrieved as the depth of the absorption feature in correspondence of one of the three dedicated channels, respect to values in other two neighbouring bands, not affected by water absorption, used as reference.

$$R_{ADPA}(\rho, u) = \frac{L_{TOA,2}(\rho_2, u) - L_{PATH,2}(u)}{w_1\left(L_{TOA,1}(\rho_1) - L_{PATH,1}\right) + w_3\left(L_{TOA,3}(\rho_3) - L_{PATH,3}\right)} [Eq.30]$$

where '1' and '3' indicates window channels (respectively in the 850-890 nm region and 1010-1050 nm region), '2' indicates a channel in the absorption region (910-950 nm), and *u* indicates the water vapour column. w_i are weighting factors determined as:

$$w1 = (\lambda 3 - \lambda 2)/(\lambda 3 - \lambda 1) \; [Eq.31]$$

and

$$w3 = (\lambda 2 - \lambda 2)/(\lambda 3 - \lambda 1) \; [Eq.32]$$

In order to estimate ρ_2, a linear regression is performed between ρ_1 and ρ_3, which are not significantly influenced by water vapour content:

$$\rho_{2\,(u=0)} = w_1\rho_1 + w_3\rho_3 \; [Eq.33]$$

and Eq. 30 becomes

$$R_{ADPA}(u) = \frac{\rho_2\,\tau_2(u)E_{g2}(u)}{\rho_2\,\tau_2(u=0)E_{g2}(u=0)} [Eq.34]$$

ATCOR employs four values of water vapour columns (*u*=0.4, 1.0, 2.0, 2.9, 4.0 cm) to calculate an exponential fit function:

$$R_{ADPA}(u) = e^{-\alpha+\beta\sqrt{u}} \; [Eq.35]$$

then inverted to found *u*. Starting with *u*=1.0 cm, the process is iterated and the water vapour maps with the smallest standard deviation in the 940 nm and 1130 nm region are selected. Finally, if both regions are available, the average or the linear regression of these two water vapour maps can be used.

In this work, atmospheric correction with ATCOR was performed both allowing visibility and water vapour concentration automatic estimation from images (***ATCOR varying*** in plots), and using Rural (for lakes) or Maritime (in Curonian Lagoon) aerosol models, with the same visibility and water vapour concentration used with 6SV (***ATCOR fixed*** in plots). Rrs values were retrieved dividing ATCOR products by π.

d. ACOLITE

ACOLITE is an atmospheric correction processor for the L8-OLI and S2-MSI developed at RBINS. It performs both the atmospheric correction and the retrieval of some WQPs. An older version of this processor (Vanhellemont and Ruddick, 2015, 2016) was initially used in this thesis to correct images simultaneous to field campaigns. These images were than reprocessed through the latest version ('Python 'public beta' 20180419.0'), but results were kept and compared.

The latest version (***ACOLITE new***) allows performing atmospheric correction, through both previous version method (called ***ACOLITE old*** in plots) based on E*xtrapolation extraction* method, and the *Dark Spectrum Fitting* (DSF) algorithm (Vanhellemont and Ruddick, 2018), this second as a default and recommended by authors.

Rayleigh correction is firstly applied, using LUTs, generated through 6SV (Vermote et al., 2006), and reflectance retrieved through normalization. With '*Extrapolation extraction*' method aerosol type is determined from the ratio ε of reflectance in two bands, using red and NIR bands, only over water pixels where the marine contribution in those bands can be assumed to be zero, or NIR and SWIR bands. In the default configuration, here used after some test using all possible combinations for OLI and MSI, SWIR bands are used, with a pixel per pixel variable aerosol type (which can also be kept fixed). Aerosol contribution is estimated from SWIR bands, assuming negligible water contribution, and spectral ε is thus derived using the simple exponential extrapolation by Gordon and Wang, 1994.

DSF method is based on the hypothesis that there are pixels in the scene with approximately null surface reflectance in at least one of the sensor bands, which are used to retrieve atmospheric

path reflectance at this band. After atmospheric gas transmittance and sky reflectance correction, a dark reflectance ρ_{dark} is calculated sorting along bands total reflectance by brightness and fitting them, for example, with an ordinary least squares regression (OLS). Aerosol optical thickness is thus estimated at 550 nm using the ρ_{dark} in each band by interpolating the path reflectance for the different τ_a defined in LUTs. Finally, the lowest root-mean-squared difference (RMSD) between the ρ_{dark} and the estimated ρ_{path} for specific bands could be used instead to select between models.

e. *Sen2Cor* – MSI Level2A

Sen2Cor (Müller-Wilm et al., 2013) is a processor developed by Telespazio-Vega for and in collaboration with ESA. It is dedicated to MSI sensor for the generation of Level-2 products, performing the atmospheric, terrain and cirrus correction on ρ_{toa} products. It is composed in four different modules, which include the scene classification in nine different classes, four for clouds (including cirrus), cloud shadows, vegetation, soils or deserts, water and snow. The algorithm for the atmospheric correction is performed using a set of Look-up tables generated via libRadtran and a rural-continental aerosol type is considered. The atmospheric correction module is an adaptation of ATCOR software into Python. Cirrus correction is included.

Sen2Cor provides as output surface reflectance, converted into Rrs dividing atmospheric corrected products by π. In addition, Sen2Cor does not resample bands before atmospheric correction, which have been thus resampled to 10 m through Sentinel-2 toolbox.

Sen2Cor is since August 2016 used to produce MSI Level2A (L2A) imagery, publicly distributed through Copernicus Open Access Hub, and since then, L2A products for this thesis have been directly downloaded from it (**MSI-L2A** in plots).

f. OLCI Level2 products

OLCI Ocean Colour L2A products (V2.23) were downloaded to be compared as a standard product, to the other products obtained in this study. They contain water reflectance atmospherically corrected, together with aerosol optical depth at 865 nm (T865) and Ångström exponent (A865), Photosynthetically Active Radiation (PAR), algal pigment concentration based on the Ocean Colour for MERIS (OC4Me) algorithm (Morel et al., 2007; O'Reilly et al., 1998), for OLCI called CHL_OC4ME, and Diffuse Attenuation coefficient at 490 nm (Morel et al., 2007), KD490_M07.

The Baseline atmospheric correction (BAC) algorithm is based on the algorithm developed for MERIS (Antoine and Morel, 2011), designed for Open Waters. It is divided in three major steps:

- Glint and white caps correction. Glint is corrected only if the value is comprised into a predefined interval. If it is higher than the upper limit, it is not corrected and pixel is flagged as 'high glint'.
- To handle situations where the Near Infrared (NIR) water-leaving radiance is not negligible, i.e. high scattering waters with high chl-a or TSM concentrations, a so-called Bright Pixel Correction (BPAC, Moore et. al. 1999; Moore et al., 2017) is integrated within BAC. Reflectance corrected for stratospheric aerosol, gaseous absorption, sun glint, Rayleigh, is used to identify the so-called 'bright pixels', over sediment loaded waters: the water-leaving reflectance is computed at 709, 779, 865 and 885 nm, solving a coupled hydrological and atmospheric optical model in the NIR (700 - 900 nm); it is implemented in terms of the IOPs, and uses LUTs built through Hydrolight (Mobley and Sundman, 2013) simulations.
- Rayleigh (molecular scattering) contribution ρ_r is determined from LUTs, corrected for local variations in atmospheric pressure. The aerosol type and load are estimated from the NIR bands at 779 and 865 nm (λ_{IR1} and λ_{IR2}). The scheme starts computing the ratio $[\rho_{path}/\rho_r]$ at the two wavelengths λ_{IR1} and λ_{IR2}, after removing eventual marine signal, where ρ_{path} is measured by the sensor and ρ_r is pre-computed. A set of aerosol thickness $\tau a(\lambda_{IR1})$, corresponding to the value of $[\rho_{path}/\rho_r]$ at λ_{IR1} and associated each one to a given aerosol model, is converted into the equivalent set at λ_{IR2}, using the spectral attenuation coefficients of each aerosol. Again, several values of the ratio $[\rho_{path}/\rho_r]$ at λ_{IR2} are obtained. Finally, the two aerosol models whose ratio bracket the one actually measured at λ_{IR2} are selected. A "mixing ratio" is determined as:

$$X = \frac{[\frac{\rho path}{\rho r}]_A - [\frac{\rho path}{\rho r}]_{A1}}{[\frac{\rho path}{\rho r}]_{A2} - [\frac{\rho path}{\rho r}]_{A1}} \quad [Eq.36]$$

where the ratios identified by subscripts A, A1 and A2 are respectively the actual ratio (measured at 778 nm) and the two tabulated ratios that most closely bracket $[\frac{\rho path}{\rho r}]_A$. *X* is used to weight the two bracketing values selected.

g. C2RCC

C2RCC (Brockmann et al., 2016) is a processor based on NN techniques, originally developed by Doerffer and Schiller (2007, 2008b) as *Case2Regional* processor and then improved through the CoastColour (www.coastcolour.org) project, available for L8-OLI, S2-MSI, and S3-OLCI.

It uses, for NN training, a large database of radiative transfer simulations of water leaving radiances and TOA radiances, to perform the inversion of spectrum for the atmospheric correction, to determine the water leaving radiance from the TOA radiances, and inherent optical properties of the water body, in a coupled system of an in-water and an atmospheric radiative transfer modelling. The in-water modelling is performed using the *Hydrolight* model (Mobley and Sundman, 2013), parametrize through a bio-optical model with five components for scattering and absorption, defined at 443 nm: pigment absorption (*apig*), detritus absorption (*adet*), gelbstoff absorption (*agelb*), a white scatterer for calcareous sediments (*bwhit*), and a typical sediment scatterer (*btsm*). *Apig* is used as a proxy of chl-a concentration, *bwhit* and *btsm* for TSM concentration, to which IOPs are converted through scaling factors.

C2RCC is used for the alternative atmospheric correction over Case-2-waters, for OLCI L2A products. Since in the distributed products only chl-a and TSM concentration products are included, with the aim to compare Rrs spectra, OLCI L1B images were processed with it, using the C2RCC processor included in SNAP software.

ANNEX II - Characterization of aerosol optical properties over selected case study areas

a. Materials and methods

For atmospheric correction through 6SV *dailyMicro* algorithm, AOD, columnar precipitable water and Ozone concentration, and aerosol microphysical properties are required but not always available from AERONET stations.

Exploiting in eight different channels direct sun measurements, and Almucantar and Principal Plane Retrieval Inversion, AERONET sun-photometers provide information about aerosol optical properties. In particular, they provide, among other parameters:

- Aerosol Optical Depth (AOD) in eight different channels in the 340-1640 nm region,
- aerosol particle size distribution in 22 bins,
- complex index of refraction at four different wavelengths,
- columnar Ozone concentration (DU),
- columnar precipitable water.

AOD, Ozone and Water vapour can indeed be gathered from other sensors products, such as Nasa's MODIS and OMI (Ozone Monitoring Instrument, on Aura platform). These estimates can be easily accessed through NASA Giovanni Web Interface (https://giovanni.gsfc.nasa.gov/giovanni/). On the other hand, no information are given on microphysical properties. For this reason, in order to understand the boundary of the variability of these parameters and trying to define a standard model, based on site-specific information, an analysis of available time series of these measurements was carried out.

In particular, data were analysed over Lake Garda from AERONET Sirmione_Museo_GC station, used for the atmospheric correction of Garda, Mantua and Iseo lakes images, and over Lake

Maggiore from AERONET Ispra station, used for lakes Maggiore, and Como and suitable for the smaller subalpine lakes in their region.

Available level 1.5 data of aerosol optical properties were downloaded from AERONET webpage, from October 2014 to June 2017 for Sirmione station and from June 1997 and June 2007 for Ispra station. Data were divided according to the four seasons and only data comprised in the time window of satellites time overpass were taken into account. This time window was:

- from 09:45 to 10:45 and from 09:15 to 10:15 UTC time for, respectively, S2 and S3 for AOT, O3 and H2O;
- from 8:30 to 11:30 for the inversion products.

Data were averaged to obtain seasonal values excepted for particle size distribution. AOT values at 550 nm used by 6SV were estimated for each measurements through an exponential function along wavelength before averaging them to obtain an average seasonal value.

Finally, the functional boxplot tool (Sun and Genton, 2011), an exploratory tool for visualizing functional data which provides the envelope of the 50% central region, the median curve and the maximum non-outlying envelope, was exploited to retrieve seasonal median curve of particles size distribution.

Averaged AERONET and EO retrieved atmospheric parameters were than used for atmospheric correction and results were compared to atmospheric corrected products obtained using synchronous AERONET measurements, when available.

b. Results

From station located in Sirmione, from October 2014 to June 2017, and the one located in Ispra, from June 1996 to June 2017, an amount of 1130 and 27880 AERONET measurements, respectively, were used to estimate mean AOD, Ozone and precipitable water over Lake Garda (Figure 77).

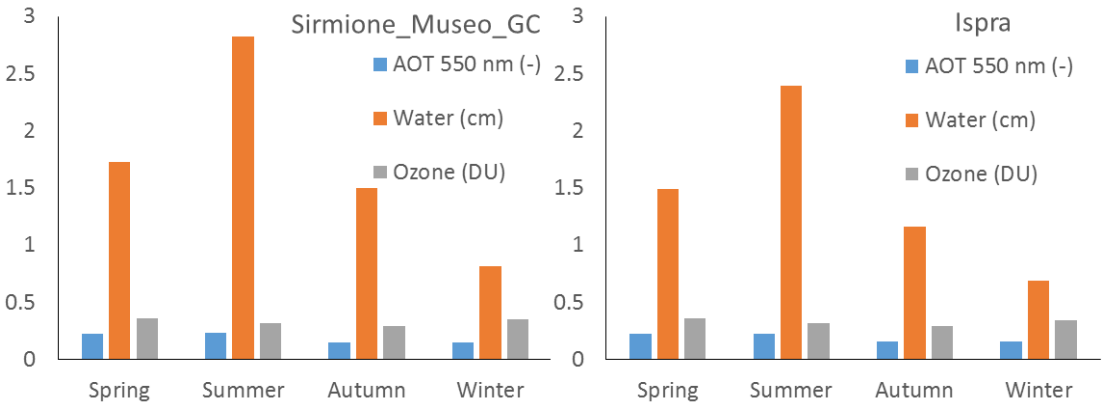

Figure 77 Seasonal mean values for AOT at 550 nm, total column precipitable water content, Ozone concentration for Sirmione_Museo_GC and Ispra AERONET stations.

Moreover, 554 and 2593 inversion products, respectively, were used to define seasonal aerosol size distribution and refractive index values (Figure 78-Figure 79).

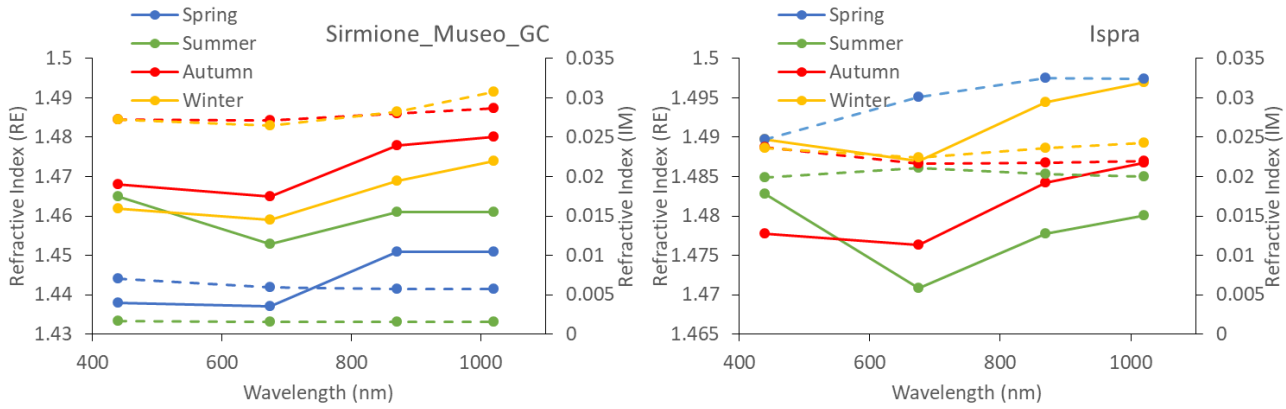

Figure 78 Seasonal mean refractive index values for Sirmione_Museo_GC and Ispra AERONET stations.

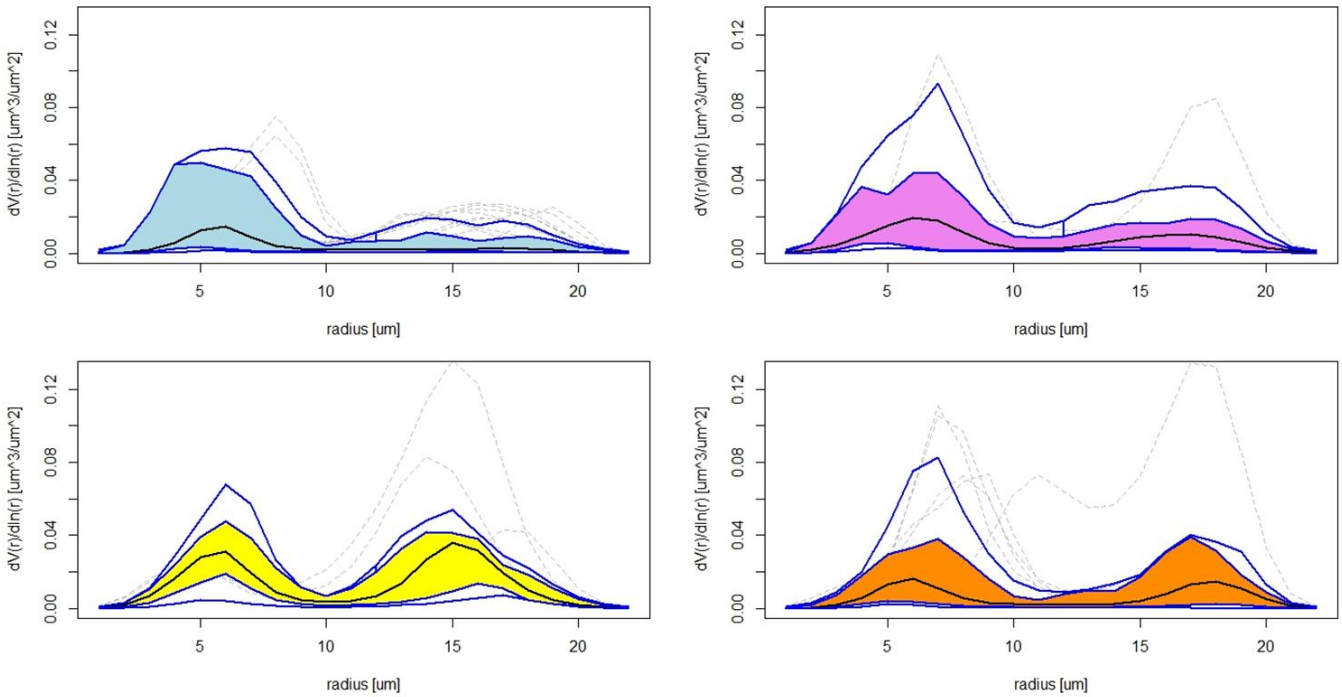

Figure 79 Seasonal functional boxplot results for particles size distribution obtained in Sirmione_Museo_GC AERONET station. In blue at top left: winter, in pink at top right: spring, in yellow at bottom left summer, and in orange bottom right: autumn.

ANNEX III – Publications and activity results presentation

In the framework of this PHD thesis the current papers were published or submitted for publication:

1. **Cazzaniga, I.**, M. Bresciani, V. Della Bella, R. Padula, R. Colombo, C. Giardino. Sentinel-3-OLCI and Sentinel-2-MSI derived Chlorophyll-a maps inter-comparison for two large Italian lakes. (Accepted on 15th December 2018 in Remote Sensing Letters Journal).
2. Bresciani, M., **I. Cazzaniga**, M. Austoni, T. Sforzi, F. Buzzi, G. Morabito, and C. Giardino. 2018. Mapping phytoplankton blooms in deep subalpine lakes from Sentinel-2A and Landsat-8. Hydrobiologia. https://link.springer.com/article/10.1007/s10750-017-3462-2.
3. Pinardi M., M. Bresciani, P. Villa, **I. Cazzaniga**, A. Laini, V. Tóth, A. Fadel, M. Austoni, A. Lami, C. Giardino. 2018. Spatial and temporal dynamics of primary producers in shallow lakes as seen from space: intra-annual observations from Sentinel-2A. Limnologica 72: 32-43.
4. Vaičiūtė, D., C. Giaridno, M. Bresciani, S.G.H. Simis, M. Bučas, E. Lukšys, **I. Cazzaniga**, I. Reusen. Water quality assessment of the Curonian Lagoon using the hyperspectral Airborne Prism EXperiment (APEX) sensor. (Submmitted to Remote Sensing).
5. Giardino, C., M. Bresciani, F. Braga, **I. Cazzaniga**, L. De Keukelaere, E. Knaeps, V.E. Brando. 2017. Bio-optical Modeling of Total Suspended Solids. In Bio-optical Modeling and Remote Sensing of Inland Waters. D.R. Mishra, I. Ogashawara, A.A. Gitelson (eds.).
6. Bresciani, M., C. Giardino, R. Lauceri, E. Matta, **I. Cazzaniga**, M. Pinardi, A. Lami, M. Austoni, E. Viaggiu, R. Congestri, M. Morabito. 2016. Earth observation for monitoring and mapping of cyanobacteria blooms. Case studies on five Italian lakes. Journal of Limnology.

Results were presented in the following meeting, congresses, or conferences:

7. **Cazzaniga, I.**, G. Luciani, C. Giardino, M. Bresciani, R. Colombo. Valutazione dei prodotti di qualità delle acque lacustri da immagini Sentinel 2 e 3. XXII Conferenza Nazionale ASITA. November 2018, Bolzano (Italy) (in print).
8. Giardino, C., M. Bresciani, **I. Cazzaniga**, A. Hommersom, P. Groetsch, M. Pires. Satellite observations autonomous in situ sensors and ecological modelling: a case study in Lake Trasimeno. GloboLakes-GEO AquaWatch Workshop, August 2018, Stirling, Scotland, UK.

9. Giardino, C., M. Bresciani, **I. Cazzaniga**. Satellite remote sensing of chl-a in subalpine Italian lakes in the last 15 years. ELLS-IAGLR-2018, September 2018, Evian, France.
10. **Cazzaniga, I**., M. Bresciani, C. Giardino, D. Vaiciute. Qualification of atmospheric correction and water quality retrieval from OLCI for European inland and transitional waters. 4th S3VT meeting, March 2018, Darmstadt (Germany).
11. Giardino, C., M Bresciani, **I. Cazzaniga**, D. Vaiciute, V. Toht V. Qualification of water quality retrieval from OLI-MSI-OLCI for European inland waters. ASLO 2017 Aquatic Sciences Meeting.
12. **Cazzaniga, I.**, C. Giardino, M. Bresciani, C. Elli, G. Valerio, M. Pilotti. Assessing heat fluxes and water quality trends in subalpine lakes from EO. Geophysical Research Abstracts 19, EGU 2017, Vienna (Austria).
13. **Cazzaniga, I.**, Bresciani, M., C. Bassani, G. Morabito, C. Giardino. Valutazione degli effetti della correzione atmosferica sulla stima dei parametri di qualità delle acque. XX Conferenza Nazionale ASITA, November 2016, Cagliari (Italy).
14. **Cazzaniga, I.**, M. Bresciani, C. Giardino, C. Bassani. Assessment Of Atmospheric Correction Methods Of Sentinel-2 In Italian Lakes. 1st Sentinel-2 Validation Team Meeting, November 2016, Rome.
15. Bresciani, M., C. Giardino, M. Pinardi, **I. Cazzaniga**, D. Vaiciute, M. Austoni, G. Morabito. Exploitation of Sentinel-2 for mapping phytoplankton in productive inland waters. 1st Sentinel-2 Validation Team Meeting, November 2016, Rome.
16. **Cazzaniga, I.**, Bresciani, M, C. Giardino, A. Rampini. Methods and tools for assessing impacts of saharan dust deposition in Lake Garda from remote sensing data. 33rd SIL Congress, August 2016, Torino (Italy).
17. Bassani, C., **I. Cazzaniga**, C. Manzo, M. Bresciani, F. Braga, C. Giardino, V.E. Brando. Atmospheric and adjacency correction of Landsat-8 imagery over inland and coastal waters near AERONET-OC sites. ESA Living Planet Symposium, May 2016, Prague.
18. **Cazzaniga, I.**, C. Giardino, M. Bresciani, K. Poser, S. Peters, A. Hommersom, et al.. Global LAkes Sentinel Services: evaluation of Chl-a trends in deep clear lakes. ESA Living Planet Symposium, June 2016, Venise (Italy).

References

- Acker, J.G. and G. Leptoukh. 2007. Online Analysis Enhances Use of NASA Earth Science Data. Eos, Trans. AGU 88(2): 14-17.
- Adler-Golden, S.M., M.W. Matthews, L.S. Bernstein, R.Y. Levine, A. Berk, S.C. Richtsmeier, P.K. Acharya, G.P. Anderson, J.W. Felde, J.A. Gardner, M.L. Goke, L.S. Jeong, B. Pukall, A.J. Ratkowski, and K.B. Hsiao-Hua. 1999. Atmospheric correction for shortwave spectral imagery based on MODTRAN4. In SPIE Proceedings Imaging Spectrometry 3753: 61-69.
- Agha, R., S. Cires, L. Wörmer, J. A. Domínguez and A. Quesada, 2012. Multi-scale strategies for the monitoring of freshwater cyanobacteria: reducing the sources of uncertainty. Water Research 46(9): 3043–3053.
- Aisté, P., H. Mazur-Marzec, and A. Razinkovas-Baziukas. 2009. Toxic cyanobacteria blooms in the Lithuanian part of the Curonian Lagoon. Oceanologia 51(2): 203-216.
- Albert, A., and C.D. Mobley. 2003. An analytical model for subsurface irradiance and remote sensing reflectance in deep and shallow case-2 waters. Optics Express 11 (22): 2873–2890.
- Ali, K., D. Witter, and J. Ortiz. 2013. Application of empirical and semi-analytical algorithms to MERIS data for estimating chlorophyll a in Case 2 waters of Lake Erie. Environ. Earth Sci. 71: 4209-4220.
- Alikas, K., K. Kangro, R. Randoja, P. Philipson, E. Asuküll, J. Pisek, and A. Reinart. 2015. Satellite-Based Products for Monitoring Optically Complex Inland Waters in Support of EU Water Framework Directive. International Journal of Remote Sensing 36 (17): 4446–4468.
- Al Shehhi, M.R.; I. Gherboudj, J. Zhao, H. Ghedira. 2017. Improved atmospheric correction and chlorophyll-a remote sensing models for turbid waters in a dusty environment. ISPRS Journal of Photogrammetry and Remote Sensing 133: 46-60.
- Antoine, D. and A. Morel. 2011. MERIS ATBD 2.7 - Atmospheric Correction of the MERIS observations Over Ocean Case 1 waters. Available at https://earth.esa.int/documents/700255/2042855/MERIS_ATBD_2.7_v5.1+-+2011.pdf (Last accessed on 10/5/2018).
- ARPA Lombardia. 2005. Laghi di Mantova: Studio della qualità di acque superficiali e sedimenti Available at: http://www.arpat.toscana.it/notizie/eventi/pre2008/ev_2005_monitoraggioacque_atti_8_arpa_lombardia_laghi_mn.zip?searchterm=None (Last accessed on 15/5/2018)
- ARPA Umbria. 2012. Tutela ambientale del lago Trasimeno. Available at: http://www.arpa.umbria.it/AU/pubblicazioni/trasimeno_book.pdf. Last accessed on 27/8/2018.
- ARPA Umbria. 2014. Valutazione dello stato ecologico e chimico dei corpi idrici lacustri dell'Umbria. Available at http://www.arpa.umbria.it/pagine/acque-superficiali (Last accessed on 13/5/2018).
- ARPA Umbria. 2017. Valutazione dello stato ecologico e chimico dei corpi idrici lacustri (2013-2015). Available at http://www.arpa.umbria.it/pagine/acque-superficiali (Last accessed on 13/5/2018).
- Arst, H., and T. Kutser. 1994. Data processing and interpretation of sea radiance factor measurements. Polar Research 13: 3-12.

- Australian Government, 2000. National Water Management Strategy of Australia and New Zeland.
- Bailey, S.W., B.A. Franz, and P.J. Werdell. 2010. Estimation of near-infrared water-leaving reflectance for satellite ocean color data processing. Opt. Express 18: 7521.
- Bassani, C., I. Cazzaniga, C. Manzo, M. Bresciani, F. Braga, C. Giardino, T. Schroeder, S. Kratzer, and V.E. Brando. 2016. Atmospheric and adjacency correction of Landsat-8 imagery over inland and coastal waters near Aeronet-OC sites. In Ouwehand, L. (ed), European Space Agency, (Special Publication) ESA SP. ESA SP, Prague.
- Barbanti, L. 1974. Morfologia della conca lacustre. In: M. Gerletti (Ed.), Indagini sul Lago di Garda. IRSA Quaderni 18, Roma: 101-115.
- Berger, S.A., S. Diehl, H. Stibor, G. Trommer, and M. Ruhenstroth. 2010. Water temperature and stratification depth independently shift cardinal events during plankton spring succession. Global Change Biology 16: 1954-1965.
- Berk, A., P.K. Acharya, L.S. Bernstein, G.P. Anderson, P. Lewis, J.H. Chetwynd, and M.L. Hoke. 2008. Band Model Method for Modeling Atmospheric Propagation at Arbitrarily Fine Spectral Resolution. U.S. Patent #7433806, issued October 7, 2008.
- Berk, A., P. Conforti, R. Kennett, T. Perkins, F. Hawes, and J. van den Bosch. 2014. MODTRAN6: a major upgrade of the MODTRAN radiative transfer code. Proceedings of SPIE 9088, Algorithms and Technologies for Multispectral, Hyperspectral, and Ultraspectral Imagery XX: 90880H.
- Bernardo, N., F. Watanabe, T. Rodrigues, and E. Alcântara. 2017. Atmospheric correction issues for retrieving total suspended matter concentrations in inland waters using OLI/Landsat-8 image, Advances in Space Research 59(9): 2335-2348.
- Bernstein, L.S., S.M. Adler-Golden, R.L. Sundberg, R.Y. Levine, T.C. Perkins, A. Berk, et al. 2005a. A new method for atmospheric correction and aerosol optical property retrieval for VIS-SWIR multi- and hyperspectral imaging sensors: QUAC (QUick atmospheric correction), in: Proc. IEEE Int. Geosci. Rem. Sens. Symp. (IGARSS'05), July 25-29, 2005. 5: 3549-3552.
- Bernstein, L.S., S.M. Adler-Golden, R.L. Sundberg, R.Y. Levine, T.C. Perkins, A. Berk, et al. 2005b. Validation of the QUick Atmospheric Correction (QUAC) algorithm for VNIR-SWIR multi- and hyperspectral imagery, in: Shen, S.S., Lewis, P.E. (Eds.), SPIE Proc., Algorithms and Technologies for Multispectral, Hyperspectral, and Ultraspectral Imagery XI. 5806: 668-678.
- Binding, C.E., T.A. Greenberg, J.H. Jerome, R.P. Bukata, and G. Letourneau. 2011. An Assessment of MERIS Algal Products during an Intense Bloom in Lake of the Woods. Journal Of Plankton Research 33 (5): 793–806.
- Botha, E.H.,V.E. Brando, J.M. Anstee, A.G. Dekker, and S. Sagar. 2013. Increased spectral resolution enhances coral detection under varying water conditions, Rem. Sens. of Environm. 131: 247–261.
- Boyer, J.N., J.W. Fourqurean, and R.D. Jones. 1999. Seasonal and Long-term Trends in the Water Quality of Florida Bay. Estuaries 22(2B): 417-430.
- Brando, V. E., and A. Dekker. 2003. Satellite hyperspectral remote sensing for estimating estuarine and coastal water quality. IEEE Transactions on Geoscience and Remote Sensing 41(6): 1378-1387
- Brando, V. E., F. Braga, L. Zaggia, C. Giardino, M. Bresciani, E. Matta, D. Bellafiore, C. Ferrarin, F. Maicu, A. Benetazzo, D. Bonaldo, F.M. Falcieri, A. Coluccelli, A. Russo, and S. Carniel. 2015. High-resolution satellite turbidity and sea surface temperature observations of river plume interactions during a significant flood event. Ocean Science 11(6): 909.

- Bresciani, M., C. Giardino, D. Longhi, M. Pinardi, M. Bartoli, and M. Vascellari. 2009. Imaging spectrometry of productive inland waters. Application to the lakes of Mantua. Italian Journal of Remote Sensing 41: 147-156.
- Bresciani, M., D. Stroppiana, D. Odermatt, G. Morabito, and C. Giardino. 2011. Assessing Remotely Sensed Chlorophyll-a for the Implementation of the Water Framework Directive in European Perialpine Lakes. Science of the Total Environment 409 (17): 3083–3091.
- Bresciani, M., R. Bolpagni, F. Braga, A. Oggioni, and C. Giardino. 2012a. Retrospective assessment of macrophytic communities in southern Lake Garda (Italy) from in situ and MIVIS (Multispectral Infrared and Visible Imaging Spectrometer) data. Journal of Limnology 71(1): 180-190.
- Bresciani, M., C. Giardino, and E. Matta. 2012b. Mapping macrophyte of Garda lake by remote sensing technique, Developing remote sensing technique approach (WP.3.3.2): Implementing monitoring systems using remote sensing techniques (WP.3.3.4), Project EULAKES.
- Bresciani, M., M. Rossini, G. Morabito, E. Matta, M. Pinardi, S. Cogliati, T. Julitta, R. Colombo, F. Braga, and C. Giardino. 2013. Analysis of within- and between-day chlorophyll-a dynamics in Mantua Superior Lake, with a continuous spectroradiometric measurement. Marine and Freshwater Research 64(4): 303–316.
- Bresciani, M., C. Giardino, R. Lauceri, E. Matta, I. Cazzaniga, M. Pinardi, A. Lami, M. Austoni, E. Viaggiu, R. Congestri, and G. Morabito. 2016a. Earth observation for monitoring and mapping of cyanobacteria blooms. Case studies on five Italian lakes. Journal of Limnology.
- Bresciani M., C. Giardino, M. Pinardi, et al. Exploitation of Sentinel-2 for mapping phytoplankton in productive inland waters. In: 1st Sentinel-2 Validation Team Meeting, November 2016b, ESRIN-Frascati.
- Bresciani, M., I. Cazzaniga, M. Austoni, T. Sforzi, F. Buzzi, G. Morabito, and C. Giardino. 2018. Mapping phytoplankton blooms in deep subalpine lakes from Sentinel-2A and Landsat-8. Hydrobiologia. https://link.springer.com/article/10.1007/s10750-017-3462-2.
- Brockmann, C., R. Doerffer, M. Peters, K. Stelzer, E. Sabine, and A. Ruescas. 2016. Evolution of the C2RCC neural network for Sentinel 2 and 3 for the retrieval of ocean colour products in normal and extreme optically complex waters. Proc. Living Planet Symposium, ESA SP-470.
- Bulgarelli, B., V. Kiselev, and G. Zibordi. 2017. Adjacency effects in satellite radiometric products from coastal waters: a theoretical analysis for the northern Adriatic Sea. Applied Optics 56: 854-869.
- Buraschi, E., F. Buzzi, L. Garibaldi, E. Legnani, G. Morabito, A. Oggioni, et al. 2008. Protocollo di campionamento di macrofite acquatiche in ambiente lacustre. Protocollo per il campionamento di fitoplancton in ambiente lacustre. Metodi biologici per le acqueAPAT (Italian Agency for the Environmental Protection). Parte 1. (In Italian).
- Buzzi, F., G. Gerosa, and G. Salvadè. 1997. Descrizione e analisi di alcuni aspetti limnologici e idrodinamici del Lago di Como. Documenta dell'Istituto italiano di idrobiologia 61: 93-115.
- Buzzi, F. 2002. Phytoplankton assemblages in two sub-basins of Lake Como. Journal of Limnology 61: 117-128.
- Callieri, C., R. Bertoni, M. Contesini, and F. Bertoni. 2014. Lake level fluctuations boost toxic cyanobacterial ‘‘oligotrophic blooms’’. Plos one 9(10): e109526.
- Carder, K.L., F.R. Chen, Z.P. Lee, S.K. Hawes, and D. Kamykowski. 1999. Semianalytic Moderate-Resolution Imaging Spectrometer algorithms for chlorophyll-a and absorption with bio-optical domains based on nitrate-depletion temperatures. Journal of Geophysical Research 104: 5403-5421.

- Carder, K.L., F.R. Chen, J.P. Cannizzaro, J.W. Campbell, and B.G. Mitchell. 2004. Performance of the MODIS semi-analytical ocean color algorithm for chlorophyll-a, Advances in Space Research 33 (7): 1152-1159.
- Carvalho, G.A., P.J. Minnett, L.E. Fleming, V.F. Banzon, and W. Baringer. 2010. Satellite remote sensing of harmful algal blooms: A new multi-algorithm method for detecting the Florida Red Tide (Karenia brevis). Harmful Algae 9:440-448.
- Chavez, P.S. 1996. Image-based atmospheric corrections - revisited and improved. Photogrammetric Engineering & Remote Sensing 62(9): 1025-1036.
- Carollo, A., and V. Libera. 1992. Geographical characteristics of the main Italian lakes. In Memorie Dell'Istituto Italiano Di Idrobiologia Dott. Marco De Marchi, eds. P. Guilizzoni, G. Tartari, G. Giussani.
- Chavula, G., P. Brezonik, P. Thenkabail, T. Johnson, and M. Bauer. 2009. Estimating chlorophyll concentration in Lake Malawi from MODIS satellite imagery. Physics and Chemistry of the Earth 34: 755–760.
- Chen, Q., Y. Zhang, and M. Hallikainen. 2007. Water Quality Monitoring Using Remote Sensing in Support of the EU Water Framework Directive (WFD): A Case Study in the Gulf of Finland. Environmental monitoring and assessment. 124. 157-66. 10.1007/s10661-006-9215-8.
- Cox, C., and W. Munk. 1954. Measurements of the roughness of the sea surface from photographs of the Sun's glitter, J. Opt. Soc. Am. 44: 838, 850.
- de Groot, R., L. Brander, S. van der Ploeg, R. Costanza, F. Bernard, L. Braat, M. Christie, et al. 2012. Global Estimates of the Value of Ecosystems and Their Services in Monetary Units. Ecosystem Services 1(1): 50–61.
- De Keukelaere, L., S. Sterckx, S. Adriaensen, E. Knaeps, I. Reusen, C. Giardino, M. Bresciani, P. Hunter, C. Neil, D. Van der Zande, and D. Vaiciute. 2018. Atmospheric correction of Landsat-8/OLI and Sentinel-2/MSI data using iCOR algorithm: validation for coastal and inland waters. European Journal of Remote Sensing 51(1): 525-542.
- Dekker, A.G., S.R. Phinn, J. Anstee, P. Bissett, V.E. Brando, et al. 2011. Intercomparison of shallow water bathymetry, hydro-optics, and benthos mapping tachinques in Australian and Caribbean costal environments. Limnol. Oceanogr. Meth. 9(9): 396-425.
- Dekker, A. G., and E.L. Hestir. 2012. Evaluating the feasibility of systematic inland water quality monitoring with satellite remote sensing; Water for a Healthy Country WIRADA. Report to the National Programme for Environmental Information 105.
- Depuis, S. 2017. Validation of Landsat-8 and Sentinel-2 algorithms for atmospheric correction on Lake Geneva. https://infoscience.epfl.ch/record/232033 (Last accessed on 25/3/2018).
- Dierssen, H., G.B. McManus, A. Chlus, D. Qiu, B_C. Gao, and S. Lina. 2015. Space station image captures a red tide ciliate bloom; Proc. National Academy of Sciences, 112(48): 14783–14787.
- Doerffer, R., and J. Fischer. 1994. Concentrations of chlorophyll, suspended matter, and gelbstoff in Case II water derived from satellite coastal zone color scanner data with inverse modeling methods. Journal of Geophysical Research 99 (C4), 7457-7466.
- Doerffer, R., and H. Schiller. 2007. The MERIS Case 2 water algorithm. International Journal of Remote Sensing 28(3-4): 517-535.
- Doerffer, R., and H. Schiller. 2008a. MERIS lake water algorithm for BEAM - MERIS algorithm theoretical basis document. Inst. Coastal Res. GKSS Res. Center, Geesthacht, Germany, Rep. GKSS-KOF-MERIS-ATBD01, Vol. 1.
- Doerffer, R., and H. Schiller. 2008b. MERIS Regional Coastal and Lake Case 2 Water Project - Atmospheric Correction ATBD, GKSS Research Center 21502 Geesthacht Version 1.0.

- Dörnhöfer, K., and N. Oppelt. 2016. Remote sensing for lake research and monitoring—recent advances. Ecological Indicators 64: 105–122.
- Dörnhöfer, K., A. Göritz, P. Gege, B. Pflug, and N. Oppelt. 2016. Water Constituents and Water Depth Retrieval from Sentinel-2A—A First Evaluation in an Oligotrophic Lake. Remote Sensing 8 (11): 941.
- Dubovik, O., and M. D. King. 2000. A flexible inversion algorithm for retrieval of aerosol optical properties from Sun and sky radiance measurements. Journal of Geophysical Research 105(D16): 20,673–20,696.
- Dubovik, O., B.N. Holben, T.F. Eck, A. Smirnov, Y.J. Kaufman, M.D. King, D. Tanre, and I. Slutsker. 2002. Variability of absorption and optical properties of key aerosol types observed in worldwide locations. Journal of Atmospheric Science 59: 590–608.
- Dubovik, O., et al. 2006. Application of spheroid models to account for aerosol particle nonsphericity in remote sensing of desert dust. Journal of Geophysical Research 111: D11208.
- Drusch, M., U. Del Bello, S. Carlier, O. Colin, V. Fernandez, F. Gascon, B. Hoersch, C. Isola, P. Laberinti, and P. Martimort. 2012. Sentinel-2: ESA's optical high-resolution mission for GMES operational services. Remote Sensing of Environment 120: 25-36.
- ESA, European Space Agency, Sentinel-3 OLCI-A preflight spectral response, 2016. Available at https://sentinel.esa.int/documents/247904/2700436/Sentinel-3-OLCI-A-spectral-response-functions. Last accessed on 8/5/2018.
- European Environmental Agency, Europe's Environment - The Dobris Assessment, 1995, available at: https://www.eea.europa.eu/publications/92-826-5409-5. Last accessed 8/5/2018.
- Fargion, G. S. and J. L. Mueller, 2000. Ocean optics protocols for satellite ocean color sensor validation. Revision 2. NASA Technical Memo. 2000-209966. NASA Goddard Space Flight Center, Greenbelt.
- Fischer, J., and H. Grassl. 1984. Radiative transfer in an atmosphere-ocean system: an azimuthally dependent matrix-operator approach. Applied Optics 23: 1032-1039.
- Fell, F., and J. Fischer. 2001. Numerical simulation of the light field in the atmosphere-ocean system using the matrix-operator method. Journal of Quantitative Spectroscopy & Radiative Transfer 69: 351-388.
- Fukushima H., A. Higurashi, Y. Mitomi, T. Nakajima, T. Noguchi, T. Tanaka, and M. Toratani. 1998. Correction of atmospheric effects on ADEOS/OCTS ocean color data: Algorithm description and evaluation of its performance. J. Oceanogr. 54: 417-430.
- Fukushima H., M. Toratani, H. Murakami, P.Y. Deschamps, R. Frouin, and A. Tanaka. 2007. Evaluation of ADEOS-II GLI ocean color atmospheric correction using SIMBADA handheld radiometer data. J. Oceanogr. 63: 533-543.
- Gallina, N., O. Anneville, and M. Beniston. 2011. Impacts of extreme air temperatures on cyanobacteria in five deep peri-Alpine lakes. J Limnol 70(2):186–196.
- Gallina, N., N. Salmaso, G. Morabito, and M. Beniston. 2013. Phytoplankton configuration in six deep lakes in the peri-Alpine region: Are the key drivers related to eutrophication and climate?. Aquatic Ecology 47: 177-193.
- Gallinaro, N., S. Tavernini, and F. Cantoni. 2013. Project EULAKES Ref. Nr. 2CE243P3, Final Report.
- Gardner, R.C. et al. 2015. State of the World's Wetlands and Their Services to People: A Compilation of Recent Analyses. Ramsar Briefing Note 7. Ramsar Convention Secretariat, SSRN.
- Gasiūnaitė, Z.R, D. Daunys, S. Olenin and R.-B. Artūras. 2008. The Curonian Lagoon. Ecology of Baltic Coastal Waters 197: 197-215.

- Giardino, C., V.E. Brando, A.G. Dekker, N. Strömbeck, and G. Candiani. 2007. Assessment of water quality in Lake Garda (Italy) using Hyperion, Remote Sensing of Environment, 109(2): 183-195.
- Giardino, C., M. Bresciani, V.E. Brando, and A.G. Dekker. 2008. Observations of the largest Italian lakes from MERIS, Proceedings of the 2nd MERIS / (A)ATSR User Workshop, Frascati, Italy 22–26 September 2008.
- Giardino, C., M. Bresciani, P. Villa, and A. Martinelli. 2010. Application of Remote Sensing in Water Resource Management: The Case Study of Lake Trasimeno, Italy. Water Resources Management 24 (14): 3885–3899.
- Giardino, C., G. Candiani, M. Bresciani, Z. Lee, S. Gagliano, and M. Pepe. 2012. BOMBER: A tool for estimating water quality and bottom properties from remote sensing images. Computers & Geosciences Elsevier 45: 313–318.
- Giardino, C., M. Bresciani, I. Cazzaniga, K. Schenk, P. Rieger, F. Braga, E. Matta, and V.E. Brando. 2014a. Evaluation of Multi-Resolution Satellite Sensors for Assessing Water Quality and Bottom Depth of Lake Garda. Sensors (Switzerland) 14(12): 24116–24131.
- Giardino, C., M. Bresciani, D. Stroppiana, A. Oggioni, and G. Morabito. 2014b. Optical remote sensing of lakes: an overview on Lake Maggiore. Journal of Limnology 73(s1): 201-214.
- Giardino, C., M. Bresciani, E. Matta, and V.E. Brando. 2015a. Imaging Spectrometry of Inland Water Quality in Italy Using MIVIS: An Overview. In: Younos T., Parece T. (eds) Advances in Watershed Science and Assessment. The Handbook of Environmental Chemistry, 33. Springer, Cham.
- Giardino, C., M. Bresciani, E. Valentini, L. Gasperini, R. Bolpagni, and V.E. Brando. 2015b. Airborne hyperspectral data to assess suspended particulate matter and aquatic vegetation in a shallow and turbid lake. Remote Sensing of Environment 157: 48-57.
- Gitelson, A.A., G. Dall'Olmo, W. Moses, D.C. Rundquist, T. Barrow, T.R. Fisher, D. Gurlin, and J. Holz. 2008. A Simple Semi-Analytical Model for Remote Estimation of Chlorophyll-a in Turbid Waters: Validation. Article. Remote Sensing Of Environment 112(9): 3582–3593.
- GLaSS project, Deliverable 5.3. Deep clear lakes with increasing eutrophication, 2015. Available at http://www.glass-project.eu/assets/Deliverables/GLaSS-D5.3.pdf (Last accessed on 1/1/2018).
- GLaSS project, Deliverable 5.2. Shallow lakes with high eutrophication and potentially toxic algae, 2015. Available at http://www.glass-project.eu/assets/Deliverables/GLaSS-D5.2.pdf (Last accessed on 1/1/2018).
- Gohin, F., B. Saulquin, H. Oger-Jeanneret, L. Lozac'h, L. Lampert, A. Lefebvre, P. Riou, and F. Bruchon. 2008. Towards a better assessment of the ecological status of coastal waters using satellite-derived chlorophyll-a concentrations. Remote Sensing Of Environment 112: 3329-3340.
- Gons, H.J, M. Rijkeboer, and K.G. Ruddick. 2002. A Chlorophyll-Retrieval Algorithm for Satellite Imagery (Medium Resolution Imaging Spectrometer) of Inland and Coastal Waters. Journal Of Plankton Research 24(9): 947–951.
- Gons, H.J., M.T. Auer, and S.W. Effler. 2008. MERIS Satellite Chlorophyll Mapping of Oligotrophic and Eutrophic Waters in the Laurentian Great Lakes. Remote Sensing Of Environment 112(11, SI): 4098–4106.
- Goody, R., and Y. Yung. 1996. Atmospheric Radiation: Theoretical Basis. New York: Oxford University Press.

- Gordon, H.R., O.B. Brown, and M.M. Jacobs. 1975. Computed relationships between the inherent and apparent optical properties of a flat homogeneous ocean. Applied Optics 14(2): 417-427.
- Gordon, H.R., O.B. Brown, R.H. Evans, J.W. Brown, R.C. Smith, K.S. Baker, et al. 1988. A semianalytic radiance model of ocean color. Journal Geophysical Research 93(D9): 10909-10924.
- Gordon, H.R., and M. Wang. 1994. Retrieval of water-leaving radiance and aerosol optical thickness over the oceans with SeaWiFS: a preliminary algorithm. Applied Optics 33(3): 443-452.
- Gower, J., S. King, G. Borstad, and L. Brown. 2005. Detection of intense plankton blooms using the 709 nm band of the MERIS imaging spectrometer. International Journal of Remote Sensing 26(9).
- Government of Canada, 1985. Canada Water Act. Government of South Africa, 1998. National Water Act. Gower, J.F.
- Guanter, L., M.C. González-Sampedro, and J. Moreno. 2007. A method for the atmospheric correction of ENVISAT/MERIS data over land targets. International Journal of Remote Sensing 28: 709−728.
- Guanter L., L. Gómez-Chova, and J. Moreno. 2008. Coupled retrieval of aerosol optical thickness, columnar water vapor and surface reflectance maps from ENVISAT/MERIS data over land. Remote Sensing of Environment 112: 2898−2913.
- Guanter, L., A. Ruiz-Verdu, D. Odermatt, C. Giardino, S. Simis, V. Estelles, T. Heege, J.A. Dominguez-Gomez, and J. Moreno. 2010. Atmospheric Correction of ENVISAT/MERIS Data over Inland Waters: Validation for European Lakes. Remote Sensing Of Environment 114(3): 467–480.
- Hastie, T.J., and R.J. Tibshirani. 1990. Generalized Additive Models 43. Chapman and Hall, London..
- Hedley, J., C. Roelfsema, B. Koetz and S. Phinn. 2012. Capability of the Sentinel 2 mission for tropical coral reef mapping and coral bleaching detection. Remote Sensing of Environment 120: 145–155.
- Hintze, J.L., and R.D. Nelson. 1998. Violin Plots: A Box Plot-Density Trace Synergism. The American Statistician 52: 181-184.
- Hirsch, R.M., and J.R. Slack. 1984. A Nonparametric Trend Test for Seasonal Data With Serial Dependence, Water Resources Research 20(6): 727–732.
- Hommersom, A., S. Kratzer, M. Laanen, I. Ansko, M. Ligi, M. Bresciani, C. Giardino, J. M. Beltrán-Abaunza, G. Moore, M. Wernand and S. Peters. 2012. Intercomparison in the field between the new WISP-3 and other radiometers (TriOS Ramses, ASD FieldSpec, and TACCS). Journal of Applied Remote Sensing 6(1): 63615.
- Holben, B.N., T.F. Eck, I. Slutsker, D. Tanré, J.P. Buis, A. Setzer, E. Vermote, J.A. Reagan, Y. Kaufman, T. Nakajima, F. Lavenu, I. Jankowiak, and A. Smirnov. 1998. AERONET - A federated instrument network and data archive for aerosol characterization, Remote Sensing of Environment 66: 1-16.
- Hu, C., K.L. Carder, and F.E. Muller-Karger. 2000. Atmospheric correction of SeaWiFS imagery over turbid coastal waters: a practical method. Remote Sensing of Environment 74: 195-206.
- Hunter, P. et al. 2017. INFORM prototype/algorithms validation report update, D5.15. Available at http://inform.vgt.vito.be/files/documents/INFORM_D5.15_v1.0.pdf. (Last accessed 24/7/2018).

- Irons, J.R., J.L. Dwyer and J.A. Barsi. 2012. The next Landsat satellite: the Landsat Data Continuity Mission. Remote Sensing of Environment 122: 11–21.
- ISPRA. 2017. Gli indicatori del clima in Italia nel 2016.
- Jaelani, L.M., B. Matsushita, W. Yang, and T. Fukushima. 2013. Evaluation of four MERIS atmospheric correction algorithms in Lake Kasumigaura, Japan. International Journal of Remote Sensing 34(24): 8967-8985.
- Jakimavičius, D., J. Kriauciuniene, and D. Sarauskiene. 2018. Impact of climate change on the Curonian Lagoon water balance components, salinity and water temperature in the 21st century. Oceanologia 60(3): 378-389.
- Jöhnk, K.D., J. Huisman, J. Sharples, B. Sommeijer, P.M. Visser, and J.M. Stroom. 2008. Summer heatwaves promote blooms of harmful cyanobacteria. Global Change Biology 14: 495–512.
- Kaufman, Y.J., and C. Sendra. 1988. Algorithm for automatic atmospheric corrections to visible near-IR satellite imagery. International Journal of Remote Sensing 9: 1357-1381.
- Keller, P.A. 2001. Comparison of two inversion techniques of a semi-analytical model for the determination of lake water constituents using imaging spectrometry data. Science of Total Environment 268: 189-196.
- Kiselev, V., B. Bulgarelli, T. Heege. 2015. Sensor independent adjacency correction algorithm for coastal and inland water systems. Remote Sensing of Environment 157: 85–95.
- Kratzer, S., E.T. Harvey, and P. Philipson. 2014. The use of ocean colour remote sensing in integrated coastal zone management: a case study from Himmerfjärden, Sweden. Mar. Policy 43: 29-39
- Kuchinke, C. P., H.R. Gordon, and B.A. Franz. 2009. Spectral optimization for constituent retrieval in case 2 waters I: Implementation and performance. Remote Sensing of Environment 113: 571−587.
- Kudela, R.M., S.L. Palacios, D.C. Austerberry, E.K. Accorsi, L.S. Guild, and J. Torres-Perez. 2015. Application of hyperspectral remote sensing to cyanobacterial blooms in inland waters. Remote Sensing of Environment 167: 196-205.
- Kutser, T., A. Herlevi, K. Kallio, and H. Arst. 2001. A hyperspectral model for interpretation of passive optical remote sensing data from turbid lakes. Sci. Total Environment 268: 1-3.
- Kutser, T. 2004. Quantitative detection of chlorophyll in cyanobacterial blooms by satellite remote sensing. Limnology and Oceanography 49: 2179–2189.
- Kutser, T., L. Metsamaa, N. Strombeck, and E. Vahtmae. 2006. Monitoring Cyanobacterial Blooms by Satellite Remote Sensing. Article. Estuarine Coastal And Shelf Science 67 (1–2): 303–312.
- Kutser, T. 2009. Passive optical remote sensing of cyanobacteria and other intense phytoplankton blooms in coastal and inland waters. International Journal of Remote Sensing 30(17): 4401–4425.
- Kutser, T., E. Vahtmäe, B. Paavel, and T. Kauer. 2013. Removing glint effects from field radiometry data measured in optically complex coastal and inland waters. Remote Sensing of Environment 133: 85–89.
- Lee, Z.P., K.L. Carder, C.D. Mobley, R.G. Steward, and J.S. Patch. 1998. Hypespectral remote sensing for shallow waters: 1. A semianalytical model. Applied Optics 37, 6329–6338.
- Lee, Z.P., K.L. Carder, C.D. Mobley, R.G. Steward, and J.S. Patch. 1999. Hypespectral remote sensing for shallow waters: 2. Deriving bottom depths and water properties by optimization. Applied Optics 38: 3831–3843.

- Lee, Z.P., K.L. Carder, and R.A. Arnone. 2002. Deriving inherent optical properties from water color: a multiband quasi-analytical algorithm for optically deep waters. Applied Optics 41: 5755-5772.
- Lee, Z.P., A. Weidemann, J. Kindle, R. Arnone, K.L. Carder, and C. Davis. 2007. Euphotic zone depth: its derivation and implication to ocean-color remote sensing. Journal of Geophysical Research 112: C03009.
- Lee, Z.P., B. Lubac, J. Werdell, and R. Arnone. 2009. An update of the quasi-analytical algorithm (QAA_v5). Available at http://www.ioccg.org/groups/Software_OCA/QAA_v5.pdf (Last accessed on 10/8/2018).
- Leoni, B., C.L. Marti, J. Imberger, L. Garibaldi. Summer spatial variations in phytoplankton composition and biomass in surface waters of a warm-temperate, deep, oligoholomictic lake: Lake Iseo. 2014. Inland Waters 4: 303-310.
- Li, L., L. Li, K. Song, Y. Li, L.P. Tedesco, K. Shi, and Z. Li. 2013. An inversion model for deriving inherent optical properties of inland waters: Establishment, validation and application. Remote Sensing of Environment 135:150-166.
- Li, L., L. Li, and K. Song. 2015. Remote sensing of freshwater cyanobacteria: An extended IOP Inversion Model of Inland Waters (IIMIW) for partitioning absorption coefficient and estimating phycocyanin. Remote Sensing of Environment 157: 9-23.
- Lim, J., and M. Choi. 2015. Assessment of water quality based on Landsat 8 operational land imager associated with human activities in Korea. Environmental monitoring and assessment 187: 4616.
- Lobo, F.L., M.P.F. Costa, and E.M.L.M. Novo. 2015. Time- series analysis of Landsat-MSS/TM/OLI images over Amazonian waters impacted by gold mining activities. Remote Sensing of Environment 157: 170–184.
- Lorenzen, C. J. 1967. Determination of chlorophyll and pheo-pigments: spectrophotometric equations 1. Limnology and Oceanography 12: 343–346.
- Malkmus, W. 1967. Lorentz band model with exponential-tailed S-1 line-intensity distribution function. Journal of the Optical Society of America 57: 323–329.
- Manzo, C., M. Bresciani, C. Giardino, F. Braga, and C. Bassani. 2015. Sensitivity analysis of a bio-optical model for Italian lakes focused on Landsat-8, Sentinel-2 and Sentinel-3. European Journal of Remote Sensing. 48: 17-32.
- Martins, V.S., C.C. Faria Barbosa, L.A. Sander de Carvalho, D. Schaffer Ferreira Jorge, F. de Lucia Lobo, and E. M. Leão de Moraes Novo. 2017. Assessment of Atmospheric Correction Methods for Sentinel-2 MSI Images Applied to Amazon Floodplain Lakes. Remote Sensing 9(4): 322.
- Matthews, M.W, S. Bernard, and K. Winter. 2010. Remote Sensing of Cyanobacteria-Dominant Algal Blooms and Water Quality Parameters in Zeekoevlei, a Small Hypertrophic Lake, Using MERIS. Remote Sensing Of Environment 114(9): 2070–2087.
- Matthews, M.W., S. Bernard, and L. Robertson. 2012. An Algorithm for Detecting Trophic Status (Chlorophyll-A), Cyanobacterial-Dominance, Surface Scums and Floating Vegetation in Inland and Coastal Waters. Remote Sensing Of Environment 124: 637–652.
- Matsushita, B., W. Yang, G. Yu, Y. Oyama, K. Yoshimura, and T. Fukushima. 2015. A hybrid algorithm for estimating the chlorophyll-a concentration across different trophic states in Asian inland waters. ISPRS Journal of Photogrammetry and Remote Sensing: 102.
- Mayer, J., M. T. Dokulil, M. Salbrechter, M. Berger, T. Posch, G. Pfister, K. T. A. Kirschner, B. Velimirov, A. Steitz and T. Ulbricht. 1997. Seasonal successions and trophic relations between phytoplankton, zooplankton, ciliate and bacteria in a hypertrophic shallow lake in Vienna, Austria. Hydrobiologia 342(0): 165–175.

- Medina-Cobo, M., J.A. Domínguez, A. Quesada, C. de Hoyos. 2014. Estimation of cyanobacteria biovolume in water reservoirs by MERIS sensor. Water Research 63: 10-20.
- Meis, S., S.J. Thackeray, and I.D. Jones. 2009. Effects of recent climate change on phytoplankton phenology in a temperate lake. Freshwater Biology 54: 1888-1898.
- Mishra, S., and D.R. Mishra. 2012. Normalized difference chlorophyll index: a novel model for remote estimation of chlorophyll-a concentration in turbid productive waters. Remote Sensing Environment 117: 394-406.
- Mishra, S., D.R. Mishra, Z.P. Lee, and C.G. Tucker. 2013. Quantifying cyanobacteria phycocyanin concentration in turbid productive waters: a quasi-analytical approach Remote Sensing of Environment 133: 141–51 .
- Mishra, D.R., I. Ogashawara, and A.A. Gitelson. 2017. Bio-Optical Modeling and Remote Sensing of Inland Waters. R.D. Mishra, I. Ogashawar, and A.A. Gitelson (eds.), Elsevier Inc.
- Mittenzwey, K.-H, S. Ullrich, A. Gitelson, and K.Y. Kondratiev. 1992. Determination of chlorophyll a of inland waters on the basis of spectral reflectance. Limnology and Oceanography 37(1): 147-149.
- Mobley C.D. 1999. Estimation of the remote-sensing reflectance from above-surface measurements. Applied Optics 38(36): 7442-55.
- Mobley, C.D., and L.K. Sundman. 2013. HYDROLIGHT 5.2 ECOLIGHT 5.2 Technical documentation. Sequoia Scientific, Redmond (WA), USA. Available at: http://www.sequoiasci.com/wp-content/uploads/2013/07/HE52TechDoc.pdf (Last accessed on 10/6/2018).
- Moore, G., J. Aiken, and S.J. Lavender. 1999. The atmospheric correction of water colour and the quantitative retrieval of suspended particulate matter in Case II waters: Application to MERIS. International Journal of Remote Sensing 20(9): 1713-1733.
- Moore, G., C. Mazeran, and J.-P. Huot. 2017. Case II. S Bright Pixel Atmospheric Correction. MERIS ATBD 2.6, Issue 5.3. (mesotrophic to high turbidity).
- Morabito, G., A. Oggioni, and M. Austoni. 2012. Resource ratio and human impact: how diatom assemblages in Lake Maggiore responded to oligotrophication and climatic variability. Hydrobiologia 698: 47–60.
- Morel, A., and L. Prieur. 1977. Analysis of variations in ocean color. Limnology and Oceanography 22(4): 709-722.
- Morel, A. 1988. Optical modeling of the upper ocean in relation to its biogenous matter content (case I waters). Journal of Geophysics Research 93: 10749-10768.
- Morel, A., and S. Maritorena. 2001. Bio-optical properties of oceanic waters: a reappraisal. Journal of Geophysics Research 106(C4): 7163-7180.
- Morel, A., Y. Huot, G. Bernar, P.J. Werdell, S.B. Hooker, and B.A. Franz. 2007. Examining the consistency of products derived from various ocean color sensors in open ocean (Case 1) waters in the perspective of a multi-sensor approach, Remote Sensing of Environment, 111(1): 69-88.
- Moses, W.J., A.A. Gitelson, S. Berdnikov, and V. Povazhnyy. 2009a. Satellite estimation of chlorophyll-a concentration using the red and NIR bands of MERIS – the Azov Sea case study. IEEE Geoscience and Remote Sensing Letters 6: 845–849.
- Moses, W.J., A.A. Gitelson, S. Berdnikov, and V. Povazhnyy. 2009b. Estimation of chlorophyll-a concentration in case II waters using MODIS and MERIS data – successes and challenges. Environmental Research Letters 4: 045005.
- Moses, W.J., S. Sterckx, M.J. Montes, L. De Keukelaere, and E. Knaeps. 2017. Chapter 3 - Atmospheric Correction for Inland Waters, In Bio-optical Modeling and Remote Sensing of Inland Waters, R.D. Mishra, I. Ogashawar, and A.A. Gitelson (eds.), Elsevier Inc.: 69-100.

- Mouw, C.B., S. Greb, D. Aurin, P.M. DiGiacomo, Z. Lee, M. Twardowski, C. Binding, C. Hu, R. Ma, T. Moore, W. Moses, and S.E. Craig. 2015. Aquatic color radiometry remote sensing of coastal and inland waters: Challenges and recommendations for future satellite missions. Remote Sensing of Environment 160: 15-30.
- Müller-Wilm, U., J. Louis, R. Richter, F. Gascon, and M. Niezette. 2013. Sentinel-2 Level 2a Prototype Processor: Architecture, Algorithms and First Results. In Proceedings of the ESA Living Planet Symposium, Edinburgh, UK, 9–13 September 2013.
- Nelder, J., and R. Mead. 1965. A Simplex Method for Function Minimization. Computer Journal 7: 308-313.
- Odermatt, D., C. Giardino, and T. Heege. 2010. Chlorophyll Retrieval with MERIS Case-2-Regional in Perialpine Lakes. Remote Sensing Of Environment 114(3): 607–617.
- Odermatt, D., et al., 2012. Review of constituent retrieval in optically deep and complex waters from satellite imagery. Remote Sensing of Environment 118: 116-126.
- Olmanson, L. G., M. E. Bauer, and P.L. Brezonik. 2008. A 20-year Landsat water clarity census of Minnesota's 10,000 lakes. Remote Sensing of Environment 112: 4086–4097.
- Olrik, K., G. Oronbergz, and H. Annadotter. 2012. Lake Phytoplankton responses to global climate changes. In Goldman, C. R., M. Kumagai & R. D. Robarts (eds.), Climatic change and global warming of inland waters: impacts and mitigation for ecosystems and societies. Wiley, Chichester: 173–199.
- O'Reilly, J.E., S. Maritorena, B.G. Mitchell, D.A. Siegel, K.L. Carder, S.A. Garver, M. Kahru, and C. McClain. 1998. Ocean Color Chlorophyll Algorithms for SEAWIFS. Journal Of Geophysical Research 103(C11): 24937-24953.
- Paerl, H.W., and V.J. Paul. 2012. Climate change: links to global expansion of harmful cyanobacteria. Water Research 46:1349– 1363.
- Pahlevan, N., Z. Lee, J. Wei, C.B. Schaaf, J. R. Schott, and A. Berk. 2014. On-orbit radiometric characterization of OLI (Landsat-8) for applications in aquatic remote sensing. Remote Sensing of Environment 154: 272–284.
- Pahlevan, N., S. Sarkar, B.A. Franz, S.V. Balasubramanian, and J. He. 2017. Sentinel-2 MultiSpectral Instrument (MSI) data processing for aquatic science applications: Demonstrations and validations. Remote Sensing of Environment 201: 47-56.
- Palmer, S.C.J., T. Kutser, and P.D. Hunter. 2015a. Remote Sensing of Inland Waters: Challenges, Progress and Future Directions. Remote Sensing of Environment 157: 1–8.
- Palmer, S.C.J., P. D Hunter, T. Lankester, S. Hubbard, E. Spyrakos, A.N. Tyler, M. Presing, et al. 2015b. Validation of Envisat MERIS Algorithms for Chlorophyll Retrieval in a Large, Turbid and Optically-Complex Shallow Lake. Remote Sensing Of Environment 157(SI): 158–169.
- Palmer, S.C.J., D. Odermatt, P.D. Hunter, C. Brockmann, M. Présing, H. Balzter, and V.R. Tóth. 2015c. Satellite remote sensing of phytoplankton phenology in Lake Balaton using 10 years of MERIS observations. Remote Sensing of Environment 158: 441-452.
- Phinn, S., C. Roelfsema, A. Dekker, V.E. Brando, and J. Anstee. 2008. Mapping seagrass species, cover and biomass in shallow waters: An assessment of satellite multi-spectral and airborne hyper-spectral imaging systems in Moreton Bay (Australia). emote Sensing Of Environment 112: 3413-3425.
- Pinardi, M. et al. 2011. Net autotrophy in a fluvial lake: the relative role of phytoplankton and floating-leaved macrophytes. Aquatic Science 73: 389-403.
- Pinardi, M., M. Bresciani, P. Villa, I. Cazzaniga, A. Laini, V. Tóth, A. Fadel, M. Austoni, A. Lami, and C. Giardino. 2018. Spatial and temporal dynamics of primary producers in shallow lakes as seen from space: intra-annual observations from Sentinel-2A. Limnologica 72: 32-43.

- Platnick, S., et al., 2015. MODIS Atmosphere L3 Daily Product. NASA MODIS Adaptive Processing System, Goddard Space Flight Center, USA: http://dx.doi.org/10.5067/MODIS/MOD08_D3.006.
- Platt, T., N. Hoepffner, V. Stuart, and C. Brown [editors]. 2008. IOCCG Report Number 7: Why Ocean Colour? The Societal Benefits of Ocean-Colour Technology. Available online at http://www.ioccg.org/reports/report7.pdf (Last accessed on 12/2/2018).
- Proud, S.R., R. Fensholt, M.O. Rasmussen, and I. Sandholt. 2010. A comparison of the effectiveness of 6S and SMAC in correcting for atmospheric interference of Meteosat Second Generation images. Journal Geophysical Research 115: D17209.
- Räike, A., O.P. Pietiläinen, S. Rekolainen, P. Kauppila, H. Pitkänen, J. Niemi, A. Raateland, and J. Vuorenmaa. 2003. Trends of phosphorus, nitrogen and chlorophyll a concentrations in Finnish rivers and lakes in 1975-2000. Science of Total Environment 310(1-3): 47-59.
- Riha, S., and H. Krawczyk. 2011. Development of a remote sensing algorithm for Cyanobacterial Phycocyanin pigment in the Baltic Sea using Neural Network approach. Proceedings of SPIE - The International Society for Optical Engineering 8175
- Richter, R., and D. Schläpfer. 2012. Atmospheric / Topographic Correction for Airborne Imagery (ATCOR-4 User Guide , Version 6 . 2 BETA, February 2012). Remote Sensing of Environment.
- Richter, R., and D. Schläpfer. 2014. Atmospheric/Topographic Correction for Satellite Imagery. DLR Report DLR-IB, 565–02/14: 231.
- Rogora, M., F. Buzzi C. Dresti, B. Leoni, F. Lepori, R. Mosello, M. Patelli, and N. Salmaso. 2018. Climatic effects on vertical mixing and deep-water oxygen content in the subalpine lakes in Italy. Hydrobiologia 824(1): 33-50.
- Roy, D.P. et al. 2014. Landsat-8: science and product vision for terrestrial global change research. Remote Sensing of Environment 145: 154–172.
- Ruddick, K.G., F. Ovidio, and M. Rijkeboer. 2000. Atmospheric correction of SeaWiFS imagery for turbid coastal and inland waters. Applied Optics 39(6): 897-912.
- Ruddick, K.G., V.D. Cauver, and Y.J. Park. 2006. Seaborne measurements of near-infrared water leaving reflectance: the similarity spectrum for turbid waters. Limnology and Oceanography 51(2): 1167-1179.
- Salmaso, N., and J. Padisák. 2007. Morpho-Functional Groups and phytoplankton development in two deep lakes (Lake Garda, Italy and Lake Stechlin, Germany). Hydrobiologia 578: 97-112.
- Salmaso, N. 2010. Long-term phytoplankton community changes in a deep subalpine lake: responses to nutrient availability and climatic fluctuations. Freshwater Biology 55: 825–846.
- Salmaso, N. 2011. Interactions between nutrient availability and climatic fluctuations as determinants of the long-term phytoplankton community changes in Lake Garda, Northern Italy. Hydrobiologia 660(1): 59–68.
- Salmaso, N., C. Capelli, S. Shams, and L. Cerasino. 2015. Expansion of bloom-forming Dolichospermum lemmermannii (Nostocales, Cyanobacteria) to the deep lakes south of the Alps: colonization patterns, driving forces and implications for water use. Harmful Algae 50: 76–87.
- Sellner, K. G., G. J. Doucette and G. J. Kirkpatrick. 2003. Harmful algal blooms: causes, impacts and detection. Journal of Industrial Microbiology and Biotechnology 30: 383–406.
- Schlaepfer, D., K.I. Itten, C.C. Borel, and J. Keller. 1998. Atmospheric Precorrected Differential Absorption technique to retrieve columnar water vapor. Remote Sensing of Environment 65: 353-366.
- Schopf, J.W. 2000. The fossil record: tracing the roots of the cyanobacterial lineage. In: Whitton B.A., Potts M. (eds) The ecology of cyanobacteria. Kluwer Academic Publishers, Dordrecht: 13–15.

- Schroeder, T., I. Behnert, M. Schaale, J. Fischer, and R. Doerffer. 2007. Atmospheric correction algorithm for MERIS above case-2 waters. International Journal of Remote Sensing 28: 1469−1486.
- Siegel, D.A., M. Wang, S. Maritorena, and W. Robinson. 2000. Atmospheric correction of satellite ocean color imagery: the black pixel assumption. Applied Optics 39(21), 3582-3591.
- Skeffington, R.A., S.J. Halliday, A.J. Wade, M.J. Bowes, and M. Loewenthal. 2015. Using high-frequency water quality data to assess sampling strategies for the EU Water Framework Directive. Hydrological and Earth System Sciences 19: 2491–2504.
- Steinmetz, F., P.-Y. Deschamps, and D. Ramon. 2011. Atmospheric correction in presence of sun glint: application to MERIS. Optics Express 19: 9783.
- Sterckx, S., E. Knaeps, S. Adriaensen, I. Reusen, L. De Keukelaere, and P. Hunter. 2015. Opera : An atmospheric correction for land and water. Proceedings of the Sentinel-3 for Science Workshop 1: 3–6.
- Stumpf, R.P., T.T. Wynne, D.B. Baker, and G.L. Fahnenstiel. 2012. Interannual Variability of Cyanobacterial Blooms in Lake Erie. Plos One 7(8).
- Sun, Y., and M.G. Genton. 2011. Functional Boxplots. J Comput Graph Stat 20(2): 316-334.
- Toming, K., T. Kutser, A. Laas, M. Sepp, B. Paavel, and T. Nõges. 2016. First Experiences in Mapping Lakewater Quality Parameters with Sentinel-2 MSI Imagery. Remote Sensing 8(8): 1–14.
- Trüper, H.G., and C.S. Yentsch. 1967. Use of glass-fiber filters for the rapid preparation of in vivo absorption spectra of photosynthetic bacteria. J. Bacteriol. 94: 1255–1256.
- Tyler, A.N., P.D. Hunter, E. Spyrakos, S. Groom, A.M. Constantinescu, and J. Kitchen. 2016. Developments in Earth observation for the assessment and monitoring of inland, transitional, coastal and shelf-sea waters. Science of the Total Environment 572: 1307-1321.
- U.S. Senate, 2002. Federal Water Pollution Control Act, 33 U.S.C. 1251 et seq.
- Utermöhl, H. 1958. Zur Vervollkommung der quantitative Phytoplankton Methodik. Mitteilungen Internationale Vereinigung für Theoretische und Angewandte Limnologie 9: 1–38.
- Valerio, G., M. Pilotti, C.L. Marti, and J. Imberger. 2012. The structure of basin-scale internal waves in a stratified lake in response to lake bathymetry and wind spatial and temporal distribution: Lake Iseo, Italy. Limnology and Oceanography 57: 772–786.
- Valerio, G., M. Pilotti, S. Barontini, and B. Leoni. 2014. Sensitivity of the multiannual thermal dynamics of a deep pre-alpine lake to climatic change. Hydrological Processes 29(5): 767-779.
- Vanhellemont, Q., and K. Ruddick. 2015. Advantages of High Quality SWIR Bands for Ocean Colour Processing: Examples from Landsat-8. Remote Sensing of Environment 161: 89-106.
- Vanhellemont, Q., and K. Ruddick. 2016. ACOLITE For Sentinel-2: Aquatic Applications of MSI Imagery. In Living Planet Symposium 2016 proceedings, edited by L. Ouwehand, 9–13. Prague.
- Vanhellemont, Q., and K. Ruddick. 2018. Atmospheric correction of metre-scale optical satellite data for inland and coastal water applications. Remote Sensing of Environment: 586-597.
- Van Mol, B. and K. Ruddick 2005. Total suspended matter maps from CHRIS imagery of a small inland water body in Oostende (Belgium). In Proceedings of the 3rd ESA CHRIS/Proba Workshop, 21–23 March 2005, ESRIN, Frascati, Italy.
- van Puijenbroek, P., C. Evers, and F.W. van Gaalen. 2015. Evaluation of Water Framework Directive metrics to analyse trends in water quality in the Netherlands. Sustainability of Water Quality and Ecology 6: 40-47.
- Ventura, S. 2003. Il problema ambientale e sanitario delle fioriture di cianobatteri nel lago Trasimeno. CNR - Descrizione e rapporto progetto.

- Vermote, E.F., D. Tanré, J.L. Deuzé, M. Herman, J.J. Morcrette, and S.Y. Kotchenova. 2006. Second Simulation of the Satellite Signal in the Solar Spectrum, 6s: An Overview. 6S User Guide Version 3.
- Verpoorter, C., T. Kutser, D.A. Seekell, and L.J. Tranvik. 2014. A Global Inventory of Lakes Based on High-Resolution Satellite Imagery. Geophysical Research Letters 4(18): 6396–6402.
- Vidot, J., and R. Santer. 2005. Atmospheric correction over inland waters: applications to SeaWiFS. International Journal of Remote Sensing 26(17): 3663-3682.
- Villa, P., M. Pinardi, V. Tóth, P. Hunter, R. Bolpagni, and M. Bresciani. 2017. Remote sensing of macrophyte morphological traits: Implications for the management of shallow lakes. Journal of limnology 76(1).
- Visconti, A., M. Manca, and R. de Bernardi. 2008. Eutrophication-like response to climate warming: an analysis of Lago Maggiore (N. Italy) zooplankton in contrasting years. Journal of Limnology 67(2): 87-92.
- Vörösmarty, C.J. et al. 2000. Global Water Resources: Vulnerability from Climate Change and Population Growth. Science (New York, N.Y.) 289 (JULY): 284–289.
- Wang, M. and W. Shi. 2005.Estimation of ocean contribution at the MODIS near-infrared wavelengths along the east coast of the US: Two case studies. Geophysical Research Letters 32: L13606.
- Winder, M., and U. Sommer. 2012. Phytoplankton response to a changing climate. Hydrobiologia 698: 5-16.
- Wolfram, G., C. Argillier, J. de Bortoli, F. Buzzi, A. Dalmiglio, M.T. Dokulil, E. Hoehn, A. Marchetto, P.J. Martinez, G. Morabito, M. Reichmann, Š. Remec-Rekar, U. Riedmüller, C. Rioury, J. Schaumburg, L. Schulz, and G. Urbanič. 2009. Reference conditions and WFD compliant class boundaries for phytoplankton biomass and chlorophyll-a in Alpine lakes. Hydrobiologia 633: 45–58.
- World Resources Institute. 2005. Ecosystems And Human Well-Being: Wetlands And Water Synthesis. Millennium Ecosystem Assessment. Washington, DC.
- Wynne, T.T., R.P. Stumpf, M.C. Tomlinson, and J. Dyble. 2010. Characterizing a cyanobacterial bloom in Western Lake Erie using satellite imagery and meteorological data. Limnology and Oceanography 55(5): 2025-2036.
- Zhai, L., T. Platt, T. Charles, S. Sathyendranath, and R.H. Walls. 2011. Phytoplankton phenology on the Scotian Shelf. ICES Journal of Marine Science 68(4): 781–791.
- Zilius, M., M. Bartoli, M. Bresciani, M. Katarzyte, T. Ruginis, J. Petkuviene, I. Lubiene, C. Giardino, P.A. Bukaveckas, R. de Wit, and A. Razinkovas-Baziukas. 2014. Feedback mechanisms between cyanobacterial blooms, transient hypoxia, and benthic phosphorus regeneration in shallow coastal environments. Estuaries and Coasts 37(3): 680–694.
- Zwart, G., M. P. Kamst-van Agterveld, I. van der Werff- Staverman, F. Hagen, H. L. Hoogveld, and H. J. Gons. 2005. Molecular characterization of cyanobacterial diversity in a shallow eutrophic lake. Environmental Microbiology 7: 365–377.

Acknowledgments

The activities were part of and co-founded by the following projects: INFORM (grant agreement No. 606865) funded under the European Community's Seventh Framework Programme (FP7/2007–2013), EOMORES (grant agreement No. 730066) funded under the European Union's Horizon 2020 research and innovation programme; BLASCO (CARIPLO Rif. 2014-1249) and ISEO (CARIPLO Rif. 2015-0241); GLaSS (7^{th} Framework Programme, project number 313256). Landsat-8 OLI data were gathered from USGS; Sentinel-2 and Sentinel-3 images were provided by ESA, through Copernicus Open Access Hub and Copernicus Online Data Access.

Thank you to ARPA Umbria for providing *in situ* data in Lake Trasimeno, and ARPA Lombardia, ARPAV Veneto and APPA Trento in Lake Garda. Thanks to Fabio Genoni (ARPA Lombardy) for providing *in situ* data of Lake Idro.

Thank you to the AERONET Principal Investigator Giuseppe Zibordi and his staff for establishing and maintaining Ispra site.

Thank you to the MODIS and OMI mission scientists and associated NASA personnel for the production of the data used in this research effort.

Thank you to Prof. Roberto Colombo who accepted to be my tutor in this PhD thesis work.

Thank you very much to Dr. Claudia Giardino and Dr. Mariano Bresciani (CNR-IREA) for the continuous tireless tutoring activity and for the additional *in situ* data provided throughout all the three years of my PhD.

Thank you to my external referees, Dr. Erin Hestir and Dr. Cristiana Bassani, who supported my work throughout these three years with useful feedback, suggestions, discussions, and long chats.

Thank you to the two external reviewers Dr. Mark Warren and Dr. Tiit Kutser, whose suggestions and comments helped a lot improving this thesis.

Finally thank you to the whole IREA staff, in particular to Erica, Lucia, Martina, Francesca, Paolo, Gabriele, Simone, and Giacomo who shared space and time with me during this 'adventure'.